IMPROVED SOUND SPEED CONTROL THROUGH REMOTELY DETECTING STRONG CHANGES IN THE THERMOCLINE

by

Jose M. Cordero Ros

B.S. and M.S. in Naval Sciences, Spanish Naval College, 2001

Extension Course in Hydrography (IHO Category "A"), Hydrographic Institute of the

Spanish Navy, 2006

THESIS

Submitted to the University of New Hampshire

in partial fulfillment of the requirements for the degree of

Master of Science

in

Ocean Engineering. Ocean Mapping

September 2018

ProQuest Number: 10934448

ProQuest 10934448

This thesis has been examined and approved.

Thesis Director, John. E. Hughes Clarke,
Professor of Ocean Engineering and Earth Science

Andrew Armstrong,
Co-Director, Joint Hydrographic Center
Affiliate Professor of Ocean Engineering
and Marine Sciences and Earth Sciences

Giuseppe Masetti,
Research Assistant Professor of Ocean Engineering

On 20th July, 2018

ACKNOWLEDGEMENTS

TABLE OF CONTENTS

ABSTRACT

IMPROVED SOUND SPEED CONTROL THROUGH REMOTELY DETECTING STRONG CHANGES IN THE THERMOCLINE

By

Jose M. Cordero Ros

University of New Hampshire, September 2018

Internal waves are a common phenomenon associated with stratification developed in shallow tidal seas during summer time. From a hydrographic point of view, they result in very rapid undulations in the main velocline which, if not accounted for, will result in significant refraction errors in multibeam echo sounder data. Mechanical sound speed profiling, both static and mobile, cannot sample this structure adequately (Hughes Clarke, 2017). Thus, an alternate means of detecting and accounting for that variability is needed.

Within the oceanographic community, it has long been recognized that a distinct acoustic volume scattering layer is often associated within or close to major oceanographic boundaries. This has been noted to reflect a combination of temperature/salinity microstructure and zooplankton around the pycnocline depth. Several weeks of multibeam survey on the Irish continental shelf were undertaken during which multispectral acoustic scattering data from a Simrad EK60 scientific echo sounder were acquired together with profiles from a Moving Vessel Profiler.

This thesis proposes and implements a method to determine the evolving sound speed structure by processing the images derived from the EK60 echo sounder. This is done by extracting the

scattering layer depth and finding the correlations with the velocline found in each of the discrete MVP profiles. Thus, a continuously evolving estimate of the local sound speed structure is derived. From this, by calculating the associated depth bias in the seafloor modeling caused by the difference in sound speed structure between the last actual profile and the estimate at each ping, a visual indication of the need for a new in situ measurement is made. In this manner, the sound speed structure may be monitored to adjust the spatial and temporal resolutions of the profile casts more efficiently.

INTRODUCTION

Motivation

Underwater remote sensing is mostly achieved by acoustic methods since electromagnetic waves, like the ones used in space and land remote sensing, do not effectively transmit through the sea water. Although acoustic waves propagate within the ocean, the sound speed and, thus, the ray path depend on local oceanographic variables, mostly temperature and salinity. Temporal and spatial variability in the ocean sound speed structure is a concern for hydrographers since, if not accounted for, will lead to refraction bias and errors in the seafloor modeling. Current in situ sound speed sampling methods often cannot cope with rapid changes in the ocean physical structure occurring in stratified continental shelf seas. As such, tracking changes in features from acoustic images of the water column, correlated with those from in situ measurements, will be studied as a complementary method to infer those alterations.

Research Objectives

a) Develop an image processing algorithm to extract the scattering layer depth from a Simrad EK60 scientific echo sounder echogram and find correlations with the true velocline from the in-situ samples.

b) Determine the temporal and spatial location where the algorithm is more effective.

c) Assess the sound speed structure uncertainty on a ping-by-ping base and show graphically when that uncertainty exceeds the survey standards.

Thesis Outline

This thesis is organized as follows. Chapter 1 describes how the changes in the sound speed control the refraction error and presents the existing phenomena in temperate stratified seas that affects the velocline. Chapter 2 describes the oceanography of the Celtic Sea, the area where the

data were extracted from. Chapter 3 introduces the Copernicus Marine Service and its applications in operational oceanography. Chapter 4 presents the methods, how the data was acquired and processed and the image processing algorithms that were applied to find the correlation between the thermocline depth and the scattering layers from the EK60 echograms. Chapter 5 presents the results and Chapter 6 contains conclusions and recommendations for future work.

CHAPTER 1

SOUND SPEED GRADIENTS AND REFRACTION ERRORS

The ocean structure is a heterogeneous environment (Defant, 1961). Temperature, pressure and salinity, which drive the oceanographic circulation, change continuously in space and time. Controlled by these parameters, the sound speed varies accordingly.

For hydrographic survey purposes, however, the ocean is assumed to be horizontally stratified without lateral variability on a local scale (Lurton, 2002) based on the consideration that the sound speed varies much faster vertically than horizontally (Kammerer, 1996). By considering only vertical changes, a sound speed profile can be modeled as composed by a number of horizontal layers of constant sound speed gradient. The corresponding acoustic ray paths thus do not diverge in azimuth and the normal to the interfaces is assumed to be vertical.

There are several empirical formulae to determine the value of the sound velocity in sea water. As an example, the simple formula of Medwin (1975) is given as:

$$c(T, S, D) = 1449{,}2 + 4.6T - 0.055T^2 + 0.00029T^3 + (1.34 - 0.010T)(S - 35) + 0.016D \quad (1)$$

This algorithm is suitable for rapid computations in oceanic waters to 1000m (Alkan et al, 2006). It shows that sound velocity is approximately 1500 m/s and that it gets higher with increasing temperature (T), salinity (S) and pressure or depth (D). Nevertheless, in the upper ocean and away from riverine influence, it is temperature that mostly affects the speed of sound rather than salinity or hydrostatic pressure. Thus, temperature gradient (most notably in the vertical) have the most profound impact on hydrographic survey

1.1 Vertical structure of the ocean

The vertical structure of the open ocean can be most commonly described as consisting of three different parts (Davis et al., 2001).

The mixed layer is at the top of the water column. The sea surface is heated by both short-wave (SW) and long-wave (LW) solar radiation and air heat exchange that are transmitted in the water column. This heat does not penetrate deeper during much of the year because it is quickly dissipated by wind stress, tidal currents and buoyancy fluxes mixing (Simpson et al., 2012). This turbulence creates a nearly isothermal and isopycnal mixed layer where sound speed is mostly driven by pressure. It is depicted in figure 1.1.
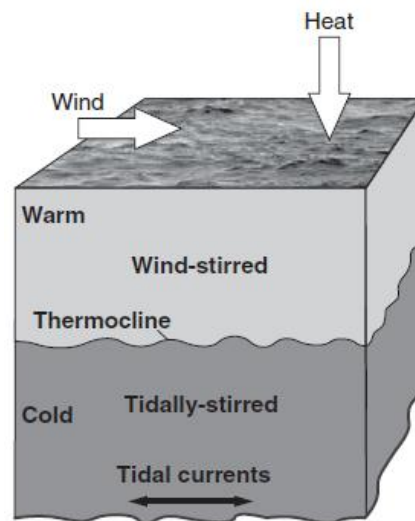
Figure 1.1. The shelf seawater column is stirred by winds and tides (Simpson and Sharples, 2012)

The thickness of the mixed layer varies with time and location as it depends on multiple factors that control the depth of the surface heat exchange and the turbulence. Frequent cool gales during winter time will deepen the mixed layer while an increase of heating and reduced storms during summer results in a shallower thermocline (Kantha et al, 1994). This homogenous layer lies above the thermocline on top of the contrasting deeper and colder waters. On the continental shelves,

as the seabed lies <100 m below this thermocline, any tidal current activity causes shear at the lower boundary resulting in homogenization of the lower layer (Simpson and Sharples, 2012). This is a common seasonal phenomenon in temperate continental shelfs, such as the Canadian, the Patagonian or the Northwest European Shelf and it is referred to as stratification (Simpson and Sharples, 2012).

The mixed layer is of great interest to the oceanographic community as it acts as a barrier and bridge between the atmosphere and the ocean bellow (Holte and Talley, 2009), and it controls the exchanges between air and sea.

The bottom of this layer is referred to as the Mixed Layer Depth and in this vertical level there is a relatively abrupt negative gradient in temperature commonly referred to as the thermocline, generally associated with a high density gradient or pycnocline. Since temperature controls sound speed in this layer, the thermocline is also a strong velocline. As these temperate shelves receive significant fresh water from land run-off, this tends to be reflected in a lower salinity in the surface mixed layer (Simpson and Sharples, 2012). As a result, there is also a weak, but not insignificant halocline, a distinct change of salinity with depth, that is also associated with this boundary. Thermocline, velocline, halocline, and pycnocline are generally at the same depth in the open ocean at mid latitudes. The thickness of this layer of strong gradients depends on the contrast between surface to deep water mass and the local current shear and it varies with latitude and season. After the spring bloom, the top of the thermocline is also usually correlated with the depth of maximum chlorophyll concentration (Sharples et al, 2001). At this depth, phytoplankton growth is possible due to the balance between the vertically decreasing solar radiation and the increase of nutrient abundance that is being mixed up from the lower nutrient rich layer. Figures 1.2a and 1.2b illustrate this process while figure 1.3 shows an example of the seasonal evolution of the thermocline depth.
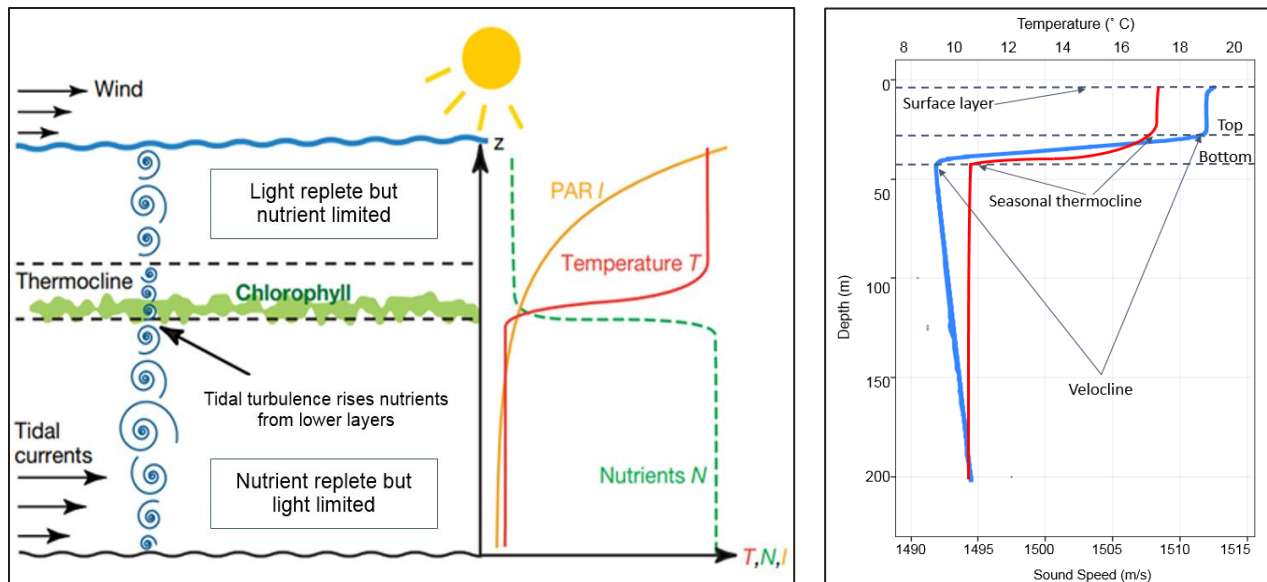
Figure 1.21a (left) Schematic of a stratified shelf sea. PAR stands for photosynthetically active radiation. (Modification of original drawing by Sharples et al, 2001). Figure. 1.2 b (right) Example of sound speed and temperature profiles as a function of depth in the summer-time stratified Celtic Sea
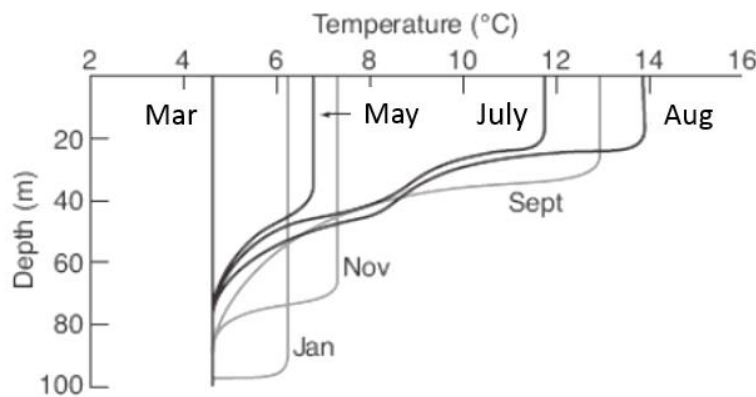
Fig. 1.3 Example of seasonal variation of the thermocline in temperate shelf seas (Sharples, 2001)

1.2 The acoustic ray refraction through the water column.

For ocean mapping purposes, the water column is commonly considered to be horizontally stratified, meaning that the oceanographic conditions are assumed to vary only with depth in a local scale (Lurton, 2002). This assumption is necessary because changes in the horizontal stratification are very difficult to measure and, at the same time, it simplifies the ray tracing

4

calculations. As it is explained further below, such an assumption is not always true (Hamilton and Beaudoin, 2010). Some phenomena cause rapid and strong oscillations in the velocline, and thus tilting the assumed horizontally stratified layers.

When the general assumption is verified, the acoustic wave propagates along layers of continuously changing sound speed where the angle of incidence between the ray and the interface between two layers of sound speed will always be relative to the vertical. This allows a straightforward application of Snell's law (Lurton, 2002). It is shown in figure 1.4.

$$\frac{cos(\theta_1)}{c_1} = \frac{cos(\theta_2)}{c_2} = \frac{cos(\theta_3)}{c_3} = ... = \frac{cos(\theta_n)}{c_n} = \text{constant}$$
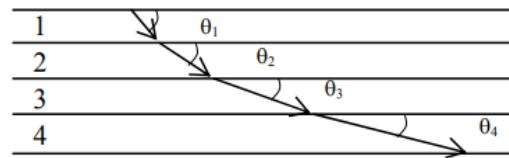
$$\text{where } c_1 < c_2 < c_3 < c_4 \quad \text{and } \theta_1 > \theta_2 > \theta_3 > \theta_4$$

Figure 1.4. Snell's law explains how the incident angle changes with layers of different sound speed.

As the sound wave propagates downwards through horizontal layers of different sound speed, the acoustic path is bent by refraction. When sound speed increases the grazing angle diminishes, and it refracts the acoustic wave toward the horizontal. Likewise, the ray will be bent to the vertical when sound speed decreases. For either case, as the interface normal is vertical, the ray azimuth does not change.

The magnitude of this refraction effect is proportional to the sound speed gradient. As the velocline is the region of maximum speed gradient, it behaves as a particularly strong refracting layer (Hamilton and Beaudoin, 2010). The thermocline location and intensity are thus of the highest

interest for the hydrographer since refraction is one of the main causes of uncertainty and bias

for Multi Beam Echo Sounder (MBES) soundings, particularly for the outer beams of the swath.

Even with the horizontal layer assumption, any change in depth or sound speed contrast over the

thermocline will be the major factor influencing refraction related errors in hydrographic survey

(Hughes Clarke, 2017).

1.3 Sound speed sampling in the water column.

The ray path is defined as the geometrical path of the acoustic wave within the water column

(Lurton, 2002) and it is modeled by tracing algorithms that require the knowledge of the sound

speed profile along the water column to account for the refraction. The variability of sound speed

is assumed to take place only along the vertical direction over short time and spatial scales. Since

it depends on the local oceanographic dynamics, an accurate and updated knowledge of the

sound speed structure is needed to avoid horizontal and vertical biases in the seafloor modeling.

Figure 1.5 provides an example that emphasizes the biases induced by an outdated sound speed
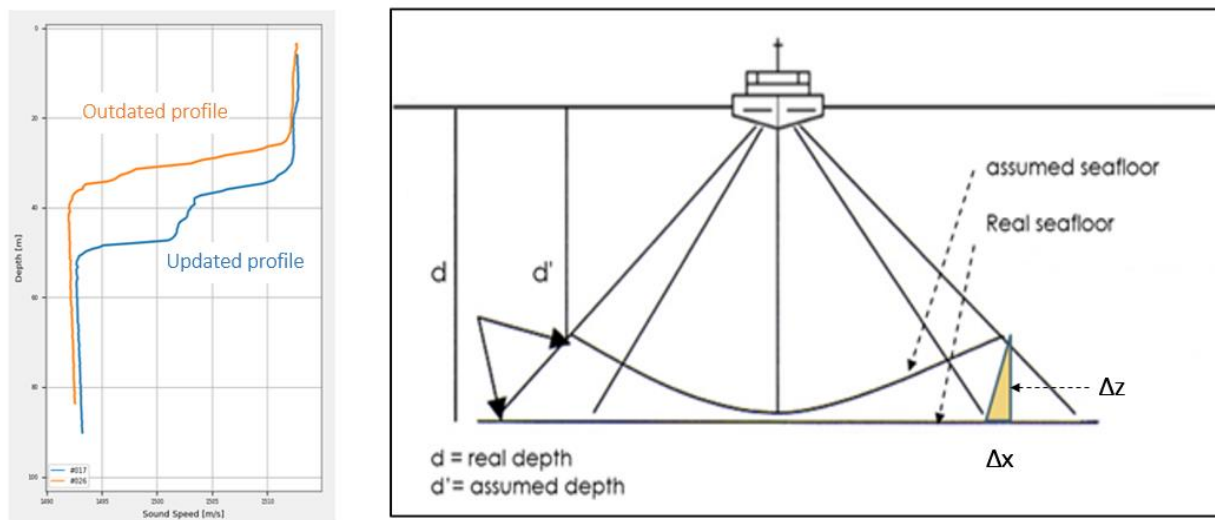
profile.

Figure 1.5. When an outdated sound speed profile (orange curve in left plot) is used for ray tracing instead of an updated one (blue curve), the resulted seafloor relief is biased in depth (Δz) and across track distance (Δx) (right plot, extracted from IHO "Manual of Hydrography",2005)

Sound speed values through the water column are obtained by readings from sensors. These measurements are done discretely at different time and space intervals throughout the survey. According to how the measurements are carried out, two main techniques can be differentiated.

1.3.1 Static profiling.

CTD (Conductivity, Temperature and Depth sensors) rosettes or sound speed probes are lowered as close as possible to the seafloor using onboard cranes and winches, while acquiring data along the water column. Although this method allows the use of accurate sensors at the same time without size restrictions, it is time and labor intensive, and it requires the vessel to remain stationary during the slow dipping and recovering process. This traditional sampling method usually is effective in ocean waters with a relatively low variability of oceanographic conditions, and the casts are normally conducted at the hours of maximum temperature gradient (dusk, dawn, noon and midnight). These sampling intervals are adequate to track the depth variations of the oceanic thermocline. Eventually, survey managers must balance the loss of survey time taken to collect a profile versus cast against an improvement in sounding accuracy. Figure 1.6 depicts an example of a CTD cast from a vessel.

Figure 1.6. CTD rosette fitted with sampling bottles and sound speed profiler. Recovery after deep ocean dip. R/V Hesperides. (photo by the author)

1.3.2 Underway profiling.

Water column cannot be adequately sampled by static profiles in highly variable oceanographic environments such as estuaries or tidal fronts (Hamilton and Beaudoin, 2010) where salinity can be highly variable due to freshwater runoff or tidal mixing. When surveying under these conditions, less time-consuming methods along with higher spatial sampling rates are needed.

- XBT (eXpendable Bathy-Thermographs).

Expendable bathythermographs measure sea water temperature while the device sinks at a pre-calculated fall rate. The signal is transmitted through a thin copper wire connected to an onboard logging computer until the sensor hits the seafloor or the wire is consumed. Then the temperature-depth trace along with historical salinity gradients can be used for the sound speed profile calculation (de Jong et al., 2002). Besides hydrographic surveying, this method is widely used in

Anti-Submarine Warfare (ASW) since XBTs can be launched underway from surface vessels, submarines and rotary wing aircrafts without the need of any other specific hardware. The main limitation of using XBTs is the reduced accuracy achieved in the computed sound profile since salinity is assumed and depth values are inferred from time assuming a precalculated fall rate. An XBT cast is show in figure 1.7.

Figure 1.7. XBT cast onboard R/V Hesperides. (Spanish Navy open archives)

By being collected underway, there can be is a limited loss of survey time if a reduced ship´s speed is required. The frequency of XBT profiling is limited only by the budget of the operator. Practically, however, dips more frequent than hourly are hard to justify. A more rapid method, without compromising accuracy would thus be favored.

- Moving Vessel Profilers (MVP).

In response to the demand for more rapid profiling without compromising accuracy, the Moving Vessel Profiler (MVP) concept (Dinn et al.,1995) was developed in Canada in the 1990s. With the MVP, underway profiling is carried out by deploying a wire connected probe astern of the vessel using an automatized winch that releases the sensor, controls the depth limit and quickly recovers the free fall instrument to near the surface, where the probe is towed until the next cast. CTD, conductivity and sound speed sensors are normally fitted within the fish probe. The data are received by an onboard computer and, after being parsed and processed, are sent to the MBES acquisition software. MVPs provide frequent sound speed profile updates without halting the survey and stopping the vessel (Rudnick and Klinke, 2007). For instance, the temporal and spatial resolutions achieved in 100 m depths while steaming at 8 knots can be as little as 3 minutes and ~1 km. Cable and hardware wear and tear are one of the limiting factors of using MVP and sampling frequency is usually lowered in long surveys to extend the maintenance periods. Such a device obviously provides the best sampling density achievable mechanically. As it is discussed further below in this thesis, however, there are still some oceanographic phenomena which cause alterations shorter in wavelength than the spatial resolution feasible using MVPs. Figure 1.8 shows an example of an MVP cast.
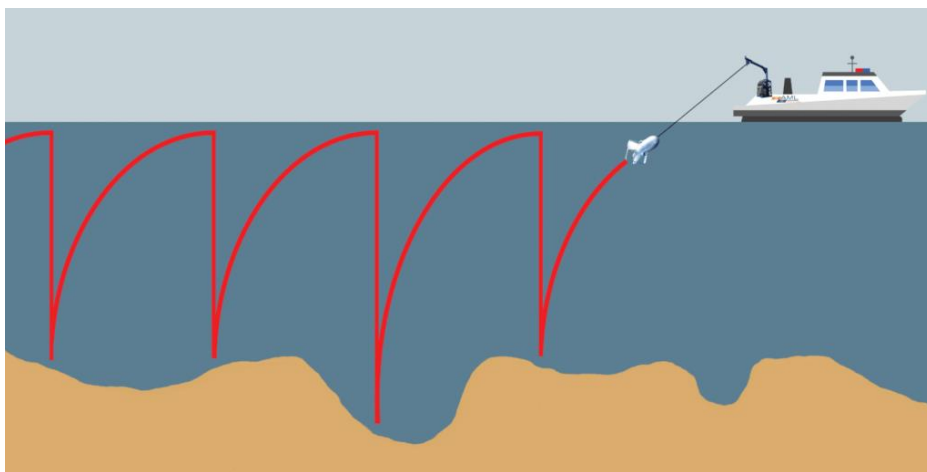
Figure 1.8. MVP cast depicted. (courtesy of AML oceanographic inc.)

1.4 Oceanographic phenomena affecting the velocline.

Temporal and spatial variations of temperature and salinity within the vertical structure of the water column will determine the intensity and the location of the velocline, and therefore, will define the refraction affecting the ray path.

Processes such as surface wind stress (from above) and bottom tidal friction (from below) both can create shear at the thermocline due to the flow differences in depth. Eventually this can induce short wavelength baroclinic perturbations in the form of either billows or internal waves that impact the sound speed structure (Hughes Clarke, 2017).

1.4.1 Billows

The shear at the thermocline in stratified waters can lead to Kelvin Helmholtz (KH) instabilities, commonly known as billows (Thorpe, 1971), with magnitudes depending on the ratio between buoyancy and shear. The Richardson number (Ri, formula 2) is the dimensionless parameter that expresses this balance between turbulence and laminarization.

$$Ri = -\frac{g}{\rho} * \frac{\frac{\delta \rho}{\delta z}}{\left(\frac{\delta u}{\delta z}\right)^2} \qquad (2)$$

Ri > 0.25 Stable
Ri < 0.25 Velocity Shear Enhances Turbulence
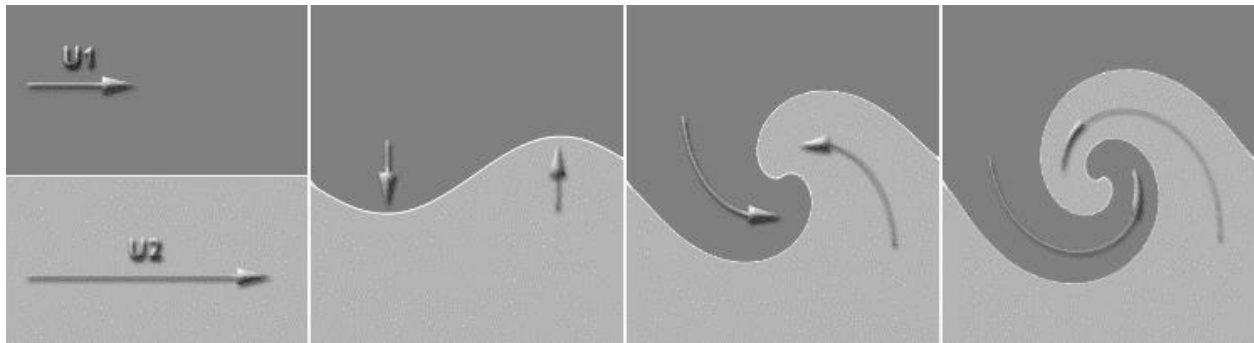
Figure 1.9. Kelvin-Helmholtz Instability Structure (obtained from www.brockmann-consult.de)

Instability will be prone to happen when shear is high, or the stratification is weak enough so that Ri falls below a critical standardized value of 1/4. The resulting KH wave often has high aspect ratios, with wavelengths over one order of magnitude greater than the thickness of the sheared layer (Smyth et al, 2012), normally shorter than 300 m and amplitudes smaller than 10 m. KH waves have short life spans and once they cease and the mixing effects are extinct, a smoothed now slightly thicker, thermocline remains.

Current mechanical sound speed sampling methods cannot cope with such short spatial resolutions, thus, the induced refraction caused by KH waves cannot be avoided. Nevertheless, their effect is expected to be short in time, mostly only while they are being formed. (Hughes Clarke, 2017).

1.4.2 Internal waves.

Another kind of perturbation affecting the sound speed structure are internal waves, defined as gravity waves propagating within a fluid instead of its surface (Sutherland et al, 2010). As with KH waves, they are characteristic of stratified masses of water, where a strong layer density contrast in present due to abrupt changes in salinity or temperature. This is a common phenomenon in temperate continental shelves during summer stratification due to enhanced solar radiation heating on the upper layers over colder water below. Freshwater riverine runoff can also generate sharp haloclines in coastal areas (Uncles, 1996).

The pycnocline originated by this density change can be perturbed by tidal flow over steep underwater topography, such as the shelf break, ridges or sills, resulting in the pycnocline deepening downstream of the topographic feature. Once the tidal flow is halted or reversed, the magnitude of the density difference controls the restoring force that causes the depression to travel as a nonlinear internal wave in an oscillating pycnocline. Since the density difference is

much weaker than at the air-sea interface, internal waves have much lower frequencies than surface waves of similar wavelengths (Massel, 2016). Internal waves are depicted in figure 1.10. Similarly, as the density contrast is so weak, they commonly have amplitudes that are much larger than surface waves. Thus, the velocline may be perturbed by dozens of meters during the passage of an internal wave, resulting in a significant refraction anomaly in the multibeam seafloor modeling due to both vertical shifting and tilting of the local velocline.
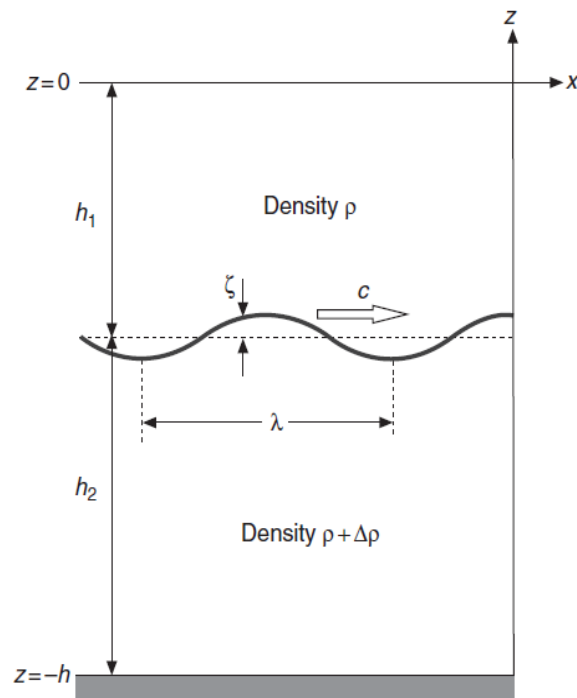
Figure 1.10. Two layer ocean model (extracted from "Internal Gravity Waves in the Shallow Seas" by Massel, 2016)

While the vertical depression may propagate as a solitary wave or "soliton" , it has been observed that in most cases internal waves propagate in groups of tens of solitons packets, with increasing amplitudes and wavelengths at the leading wave while decreasing with each undulation. They can travel long distances retaining their shape transporting momentum and mass. They can break when passing over shallow banks or the edge break, mixing the denser, colder and nutrient rich below. This phenomenon is believed to be of major importance in reintroducing nutrients in the

surface mixed layer (Sharples, 2010). As they are typically longer wavelength than the local layer depth ($\lambda \gg h1$) they are non-dispersive (long waves).

Internal waves can be considered mostly sinusoidal shaped but, more in detail, since the propagation speed is directly proportional to the isopycnal depth for a 2-layers system in which $h_1 \ll h_2$, wave troughs propagate faster that the peaks and it leads to a more triangular-like form of the wave (Hughes Clarke, 2017).

Solitons are generated at the same timescales as the tides in spring tide periods whereas they are not often observed at the neap tide phase. If there is a diurnal inequality the large of the two tides will generate the most noticeable packet. Seasonal density variability and meso-scale currents influence the generation and development of internal waves (Apel, 2002).

Typical values of the main characteristics of internal waves in temperate continental shelves are shown in table 1.1.

Characteristic	Symbol	Scale
Packet Length	L (km)	1 – 10
Amplitude Factor	$2\eta_0$(m)	-15
Upper Layer Depth	h_1(m)	20 – 35
Lower Layer Depth	h_2(m)	30 - 200
Long Wave Speed	c_0 (m s^{-1})	0.5 - 1.0
Maximum Wavelength	λ_{MAX} (m)	100 – 1000
Crest Length	C_r(km)	0 - 30
Internal Tidal Wavelength	$D = VT$ (km)	15 – 40
Characteristic Soliton Width	l_1(m)	100

Table 1.1. Typical magnitudes of the Internal waves characteristic in continental shelves (Apel, 2002)

1.5. Internal wave observation.

This phenomenon is of great interest in physical oceanography, since it helps to explain the dynamics of the continental shelf. It is as well relevant in fields such as oil extraction and antisubmarine warfare because energic internal wave packet entails unexpected stresses to offshore structure and complicate submarine detection.

Under favorable conditions, internal wave effects can be observed using remote sensing through satellite-borne synthetic aperture radars (SAR). (Fig. 1.11) This technique is widely employed to detect internal wave packets on the sea surface (Zheng et al., 2004) along with multispectral radiometer imaging and aerial photography. Such visibility is only possible under certain surface wave and wind speeds, however, and is thus not a reliable way of detecting their presence. Acoustic imagery of the water column is another effective remote sensing method for smaller scales. This method is detailed further below and depicted in figure 1.12.

In the absence of remote sensing methods, it is hard to detect the presence of these phenomena. In-situ measurements are normally made using shipborne underwater sensors logging temperature, density or plankton concentration. In as the case of sound velocity profiling, as discussed previously the wavelength of internal waves is shorter than the spatial resolution currently achievable with mechanical sampling methods.
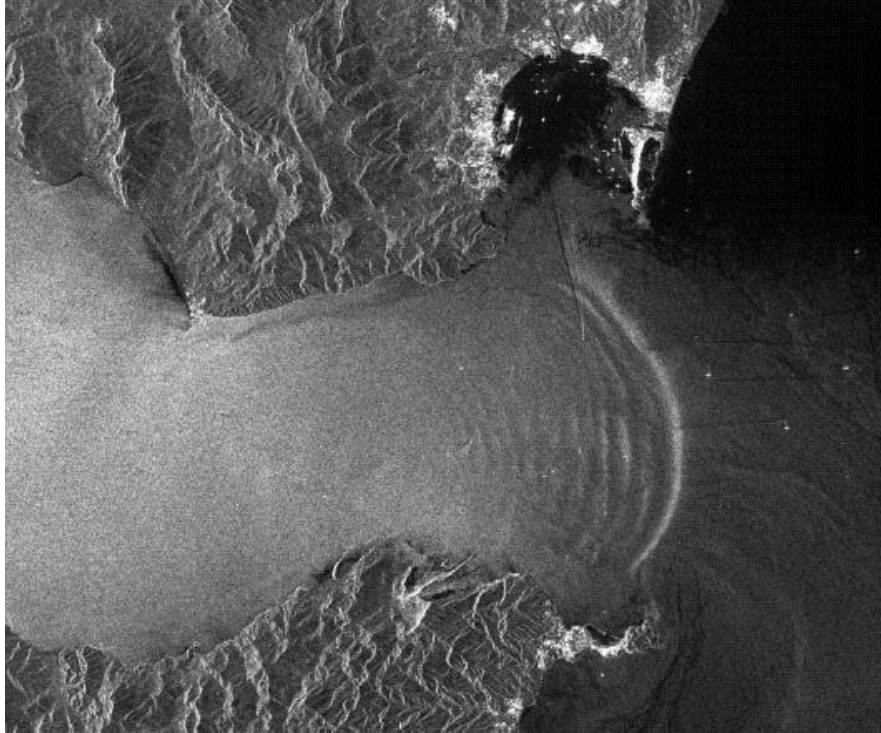
Figure 1.11. SAR image of internal wave packet in the Strait of Gibraltar. (Space Dept., DERA, UK)
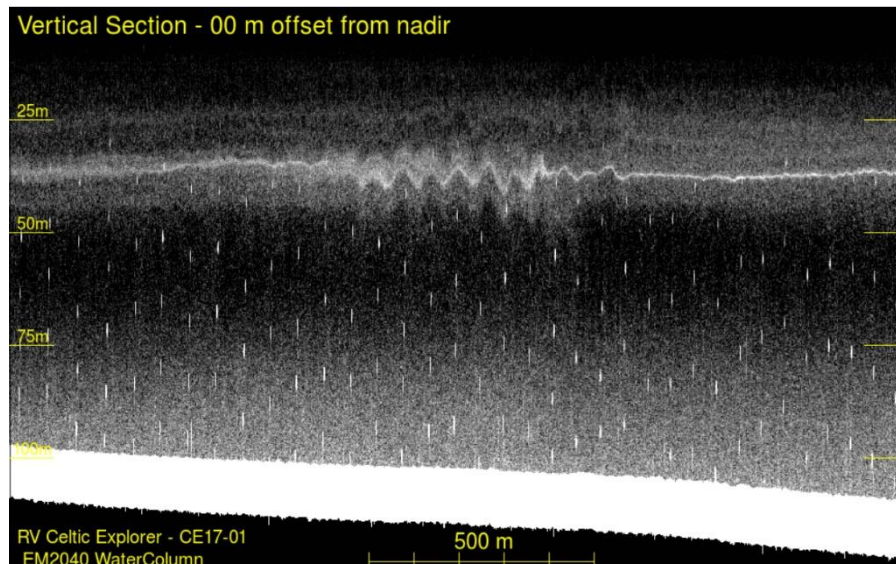
Figure 1.12. Acoustic image from an internal wave packet in the Celtic Sea (Hughes Clarke, 2016).

1.6. Impact of internal waves in multibeam surveying.

Internal waves perturb the initially horizontal pycnocline producing vertically oscillation and tilt. Both effects bias the MBES ray tracing by inducing errors in the seafloor modeling that frequently exceed the International Hydrographic Organization (IHO) specifications.

The vertical shifting of the velocline, as the internal wave passes, results in the ray path being refracted at a different depth than the one calculated from the sound speed profile. Therefore, the true refracted ray will travel a different path through the successive layers and will eventually hit the seafloor at a different time and place than the calculated ray path. This is translated into an erroneous harmonic mean error at nadir and an increasing horizontal offset as the depression angle diminishes. Figure 1.13 illustrates it. The overall effect of the vertical oscillation without tilting of the velocline is a smile-frown geometry in the seafloor modeling, symmetrical at each side of the nadir and cancelling out at about 45 degrees (Beaudoin et al, 2010)
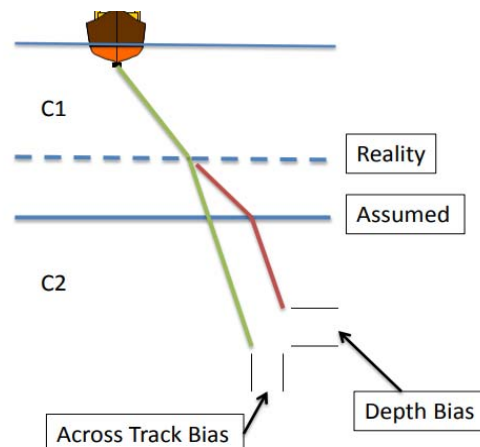
Figure 1.13. Vertical shifting of the velocline (Beaudoin, 2011)

In addition, the effect of tilting the velocline breaks the assumption that the water column is divided in horizontal layers of same density in a local scale. According to Snell's law, the incident ray will be refracted in an angle with respect to the normal to the inclined velocline,

which is no longer the vertical. It will induce a bias in the refracted ray of the same magnitude of the velocline tilt angle at the point. This affects not only the MBES oblique beams but also those aimed at nadir. This angular error creates depth and across track bias in the seafloor modeling.
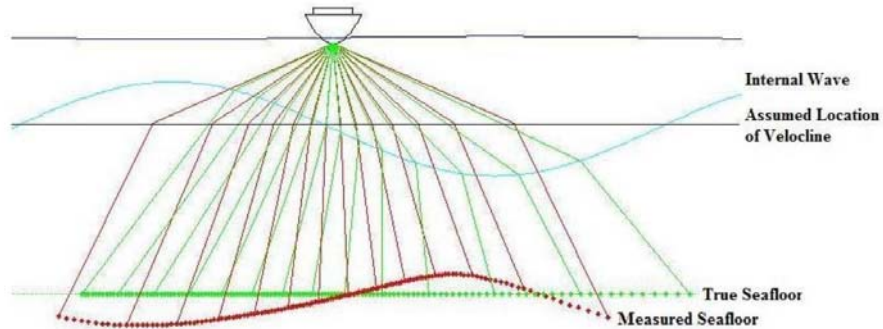
Figure 1.14. Tilted velocline effect on the seafloor modeling (Hamilton and Beaudoin, 2010).

Another consideration to take in to account is the azimuth of the perturbation with respect to the ship's track. The effect of a titled velocline will be greater when an internal wave propagates orthogonal to the ship's track since the induced refraction will dramatically accentuate the across track error in the seafloor modeling. Conversely, this effect if minimized when an internal wave propagates in the same directions as the survey line (Hamilton and Beaudoin, 2010). Nevertheless, the tilting effect cannot be determined by using a single beam echo sounder (SBES) since the two-dimensional cross section that these systems provides only shows a projection of the wave. An example of this is depicted in figure 1.15.
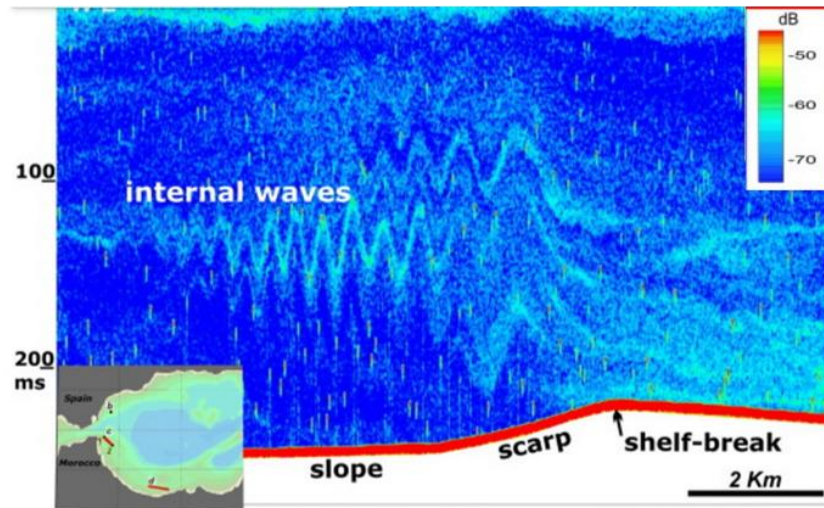
Fig 1.15. Soliton packets eastward of Gibraltar are acoustically imaged and projected into a 2D plane by using a SBES (CESIC, 2009)

1.7 Acoustic Imaging of perturbations in the thermocline

Acoustic remote sensing is a fast, qualitative and compendious alternative to in situ water column sampling techniques (Lavery, 2014). Echosounders have been used to detect scatterers in the water column since WWII. Fish school detection was firstly attempted by Cushing (1952). Investigations of acoustic scattering from suspended sediment layers and internal waves were conducted by Proni et al. (1975). Layers of different density and sound speed (Thorpe and Brubaker ,1983) as well as zones of turbulence (Oakey and Cochrane, 1998) and zooplankton (Stanton et al., 1994) can be observed in an echogram. More recently, Ross and Lueck, (2005) estimated turbulent intensities using a SBES echosounder along with CTD profiles.

The example below (fig. 1.16) illustrates a multispectral acoustic image of a strong thermocline in the Celtic sea during the summer stratification using a Simrad EK60 single beam echosounder operating simultaneously at 3 frequencies along with an overlay of two MVP sound profiles. The distinctive strong scattering horizon clearly correlates with the depth of bottom of the thermocline in the along track direction.

19
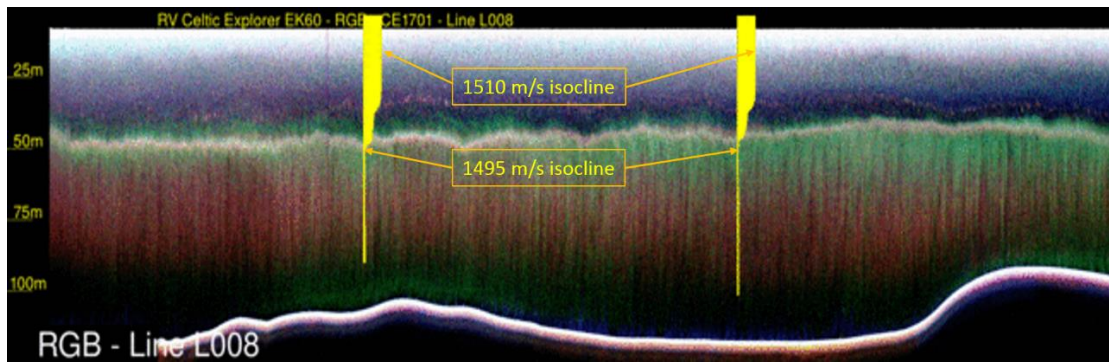
Figure 1.16 Example of a water column scattering layer mimicking the bottom of the thermocline

It can be considered that the ocean is usually stratified by layers of fine scale acoustic scatterers (Hughes Clarke, 2017) from biological (zooplankton, fishes) and physical (microstructure, turbulence, and suspended sediments) origin (Lavery et al.,2009). However, these scattering sources can be present simultaneously or intermittently (Rothschild and Osborn, 1988), which makes difficult to determine what is primarily controlling the scattering strength.

The use of different frequencies, beam widths and bandwidths may help discriminate the source of the scattering (Stanton et al, 1998). Some studies (Lavery et al, 2007) suggest that backscatter from microstructure turbulence is enhanced at frequencies lower than 100 kHz, whereas that for zooplankton occurs when using higher frequencies (figure 1.17). Ross et al. (2007) indicate that turbulence can be distinguished from biomass by sampling at different ranges. The apparent volume scattering strength from a discrete biological individual intensifies as it is closer to the echosounder, "*and so at some range, will become greater than, and the zooplankter will become visible over the turbulent background', (*Ross, 2003). Conversely, response from turbulence is controlled by the number of scatterers per unit volume and it is preserved on average, therefore varying the transducer range doesn´t not change the resulting volume scattering strength.

Also, another factor to consider for the acoustic imaging of the thermocline is the diurnal vertical migration. This is the zooplankton ascension pattern at dusk to the euphotic zone in order to feed

on phytoplankton and avoid predators during the night (Kimmerer et al, 2002). Conversely, this vertical displacement occurs downwards at dawn. The diurnal vertical migration will cause the appearance of several oblique scattering layers, corresponding to the migrating zooplankton and to passive tracers. If acoustic layers are to be used as an indicator of sound speed structure, clearly the method has to cope this non-sound speed related structure variation.
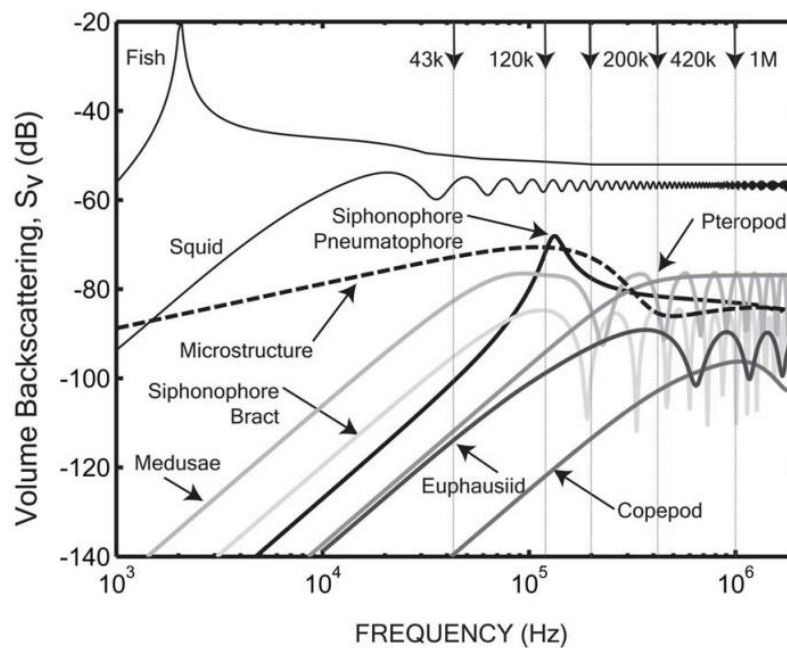
Figure 1.17. Scattering model comparing microstructure and biological frequency responses using a BIOMAPER-II system (Lavery et al, 2008).

Regarding internal waves, as a major contributor to perturbations in the thermocline, they have long been observed using echosounders (Munk and Garrett, 1973; Proni and Apel, 1975; Haury et al., 1983; Wiebe et al., 1997). Their amplitude and wavelength could be resolved since SBES achieve range resolutions and beam widths smaller that these features in the internal waves. However, the origin of the associated backscatter is still a matter of research (Stanton et al, 1998). If an algorithm can be developed to track layers as they are perturbed, a mean of rapidly tracking velocline changes is possible. This is the main aim of this thesis.

CHAPTER 2

OCEANOGRAPHY OF THE CELTIC SEA

2.1 General overview.

The Celtic Sea is a shallow embayment of the eastern North Atlantic bounded by Southern Ireland, South West of Wales, Cornwall, and Brittany. It limits to the North with the Irish Sea at Saint George's Channel, it meets the English Channel to the East and extends 400 km to the SW until the break of the slope at the 200 m contour of water depth (Pingree,1980). The Celtic Sea covers an area roughly 150 km by 500 km. The seabed under the Celtic Sea is called the Celtic Shelf and it is a part of the European continental shelf.

The physical oceanography of the Celtic Sea in characterized by an intense tidal mixing, advections fluxes, and by a seasonal summer time stratification of the shelf waters that is routinely perturbed by the intense internal wave activity originated at the shelf break (Pingree, 1975).

Figure 2.1. Celtic sea location. (IHO Special Publication num. 23)

2.2 Bathymetry.

The Celtic sea is characterized by shallow depths, between 80 m and 160 m, with a sea floor of relatively low relief topography, but with a number of prominent SW-NE oriented ridges. The central area hosts the Celtic Deep of 130 m depth, and several shallower banks, such as Labadie Bank, Jones Bank and the Great Sole Bank. Steep rugged flanks of submerged glacial troughs are found in the SW limits of the shelf edge (Walmsley et al., 2016). In the north, in St George's Channel, the water depths are around 160 m. The 100 m contour is on average located approximately 70 km from the coast. At the shelf break, 400 km to the west of Ireland, depths suddenly increase from less than 200 m to more than 1,500 m at the foot of the continental shelf. Sediments of sand and gravel characterize the seafloor over much of the Celtic Sea (Uncles and Stephens, 2007). At the present time, the systematic mapping of the Irish sector of this area is being carried out by the Irish Marine Institute. This thesis uses part of these data.
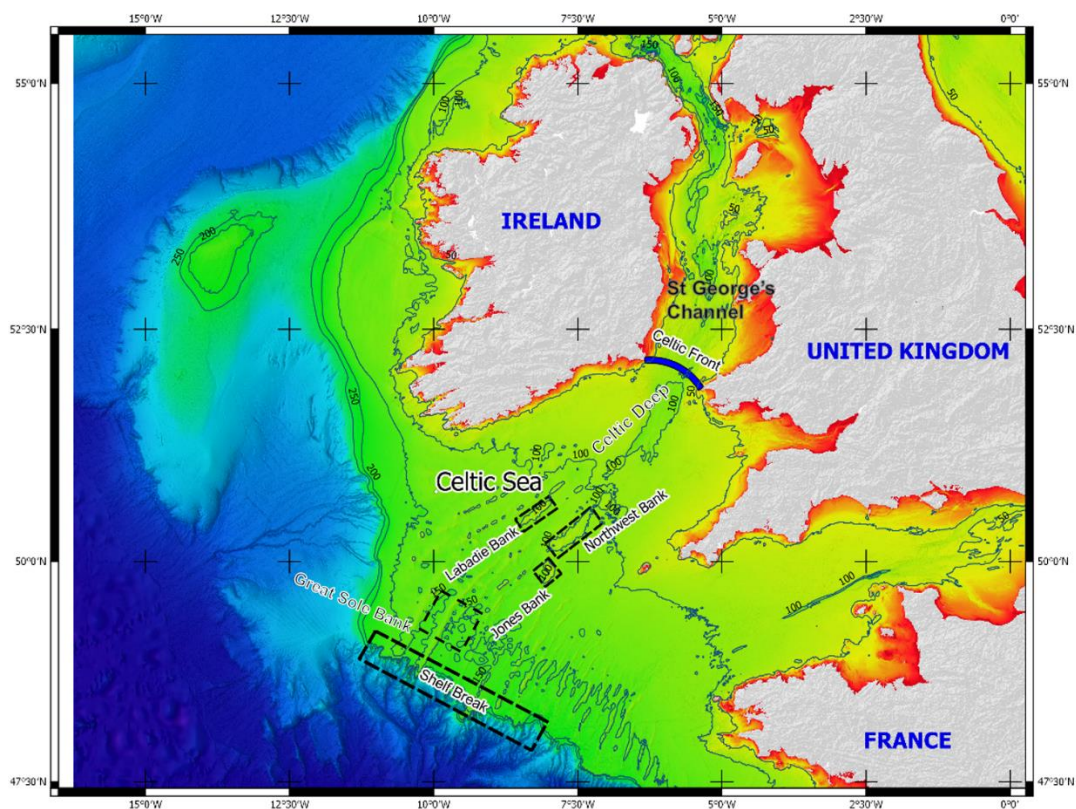
Figure 2.2. Bathymetry of the Celtic sea (GEBCO, 2014)

23

2.3. Dynamics

The Celtic Sea can be broadly described as a seasonally stratified, down welling shelf system (Holt et al., 2009) with important atmospheric fluxes, tides dynamics and riverine inputs. Ocean water exchanges takes place throughout the shelf edge with a net inflow of surface waters and a net outflow from the sea bottom thorough the shelf edge (Wakelin et al., 2009). As such it may be considered to have a negative estuarine circulation superimposed.

2.3.1. Temperatures

The Celtic sea is located in a temperate region where the coldest average sea surface temperatures occur in February, ranging from 11°C in the central area to less than 8.5 C at St. George's Channel. During this period surface temperatures are very close to those in the bottom (Pingree, 1980), leading to a minimal stratification. The warmest temperatures are on average observed in August, varying from approximately 17°C in the central area of the Celtic Sea to 15°C in the St. George's Channel. Conversely to what occurs in winter time, mean bottom temperature is on average 6°C colder than the mean surface temperature over the shelf. This difference is not observed in St. George's Channel, where surface and bottom temperatures are very close in average. This indicates a strong stratification over the Celtic Sea which switches quite abruptly past a tidal front to a well-mixed environment in the St. George's Channel and shows the water column mixing at the tidal fronts (Uncles, 2007). The same transition is observed in to the English Channel, past the Ushant front. Figure 2.2 illustrates this process.
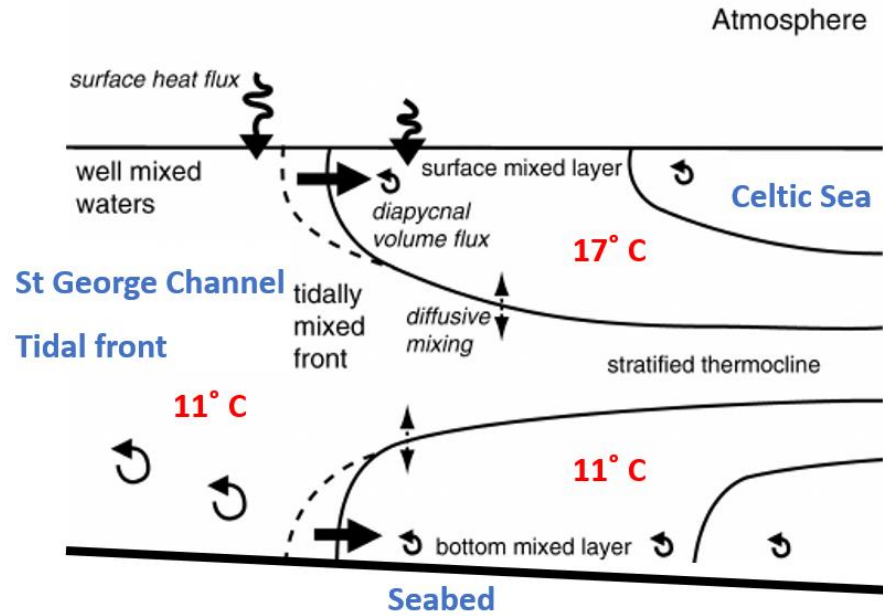
Figure 2.2. Summer stratification over the Celtic sea and mixing at St George Channel. (Modified from the original figure by Sharples et al, 2010)

2.3.2 Winds

The Celtic Sea is mostly influenced by the climatologic conditions in the North Atlantic Ocean. Variable, mostly westerly winds with frequent storms are predominant for much of the year. During winter, gales create large swell waves with a significant height between 8m and 12m (Carter and Challenor, 1989). Springs and summers are characterized by frequent and gentle winds from the North and the East. This drop in wind mixing is complementary to the increase in solar radiation, causing and intensifying the summer stratification.

2.3.3 Water circulation and fresh water contribution

The North Atlantic Drift (NAD) mostly controls the water circulation in the Celtic Sea, bringing warm water northwards and moving it around Ireland and Britain. The NAD is driven by westerly winds and by density differences between the northern waters and the warmer water in the South. This warm ocean current has a great influence in the Northwest European continental shelf. The

most notable effect being that winter temperatures on the UK and Ireland are warmer than those located in lower latitudes of the northeast coast of the United States and Canada (AECOM and METOC report, 2010).

Along the western shelf break, the Irish shelf edge current flows northwards and west of Ireland throughout the year but it is stronger during the summer (fig. 2.3). On the shelf, the weaker Irish coast current drifts northwards from Brittany up to the mouth of St. George channel and along the south coast of Ireland (OSPAR, 2000; Young et al., 2004). North of the Celtic sea, the Western Irish Sea gyre ((fig. 2.3) transport nutrients and retain industrial contaminants throughout is a matter of particularly relevance for environmental implications (Hill and Brown, 1997). The local currents of course are strongly modified by the tidal forcing. Those regional currents thus reflect the residual subtidal drift in the area.
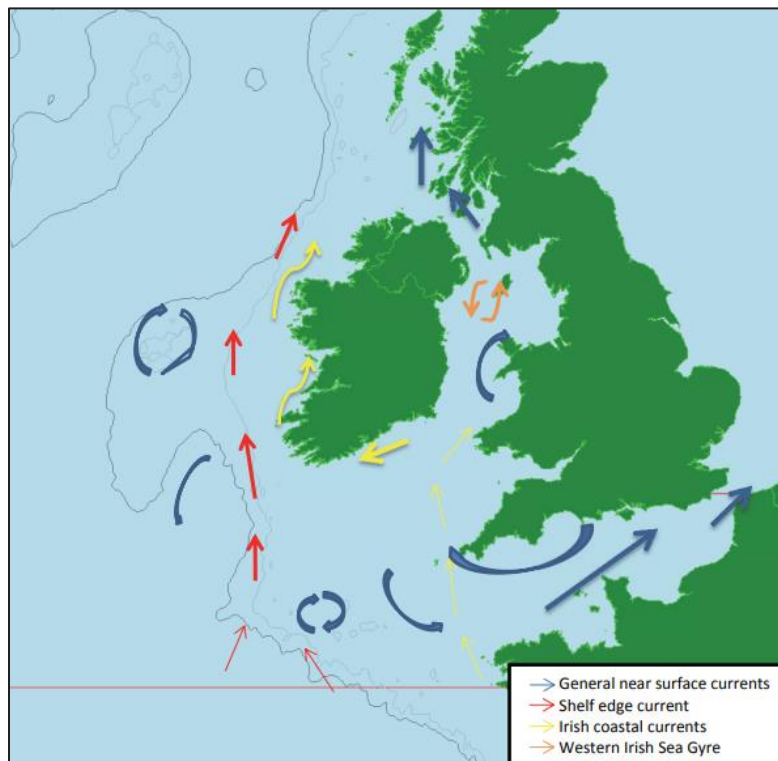
Figure 2.3. General surface currents in the Celtic sea area (atlas.marine.ie, 2014)

2.3.4 Rain

The rainfall regime over the Celtic sea and the surrounding areas is oceanic (Kendrew, 1961) with more rain in the winter than in the summer. The wettest months are October, November and December while the driest months are April, May and June. The rain during the three driest months is around half of the rain during the three wettest (Pingree, 1980).

Several significant rivers discharge fresh water into the Celtic Sea and influence the environment. The most important are the rivers Loire in Brittany and Severn in Wales, and the rivers Lee and Blackwater discharging in the east coast of Ireland.

2.3.5 Salinity

The Celtic Sea salinity is influenced by fresh water input from river run off, rain, sea surface evaporation and the contribution of the denser and saltier Atlantic waters (Uncles and Stephens, 2007). The salinity distribution is controlled by tidal mixing.

The surface salinity decreases from the shelf edge to Saint George's Channel. The maximum salinity is observed at the end of the winter while late summer and early fall are the periods of the freshest water (Cooper, 1961), as depicted in figure 2.4. This difference is explained by a reduction in the mean wind speed that leads to a decline in the surface advection and evaporation and therefore, reducing salinity. Fresh water contribution has a relevant effect on salinity near shore. Substantial variations in annual salinity are indicative of possible changes in the Atlantic Ocean inflow strength (Pingree, 1982).
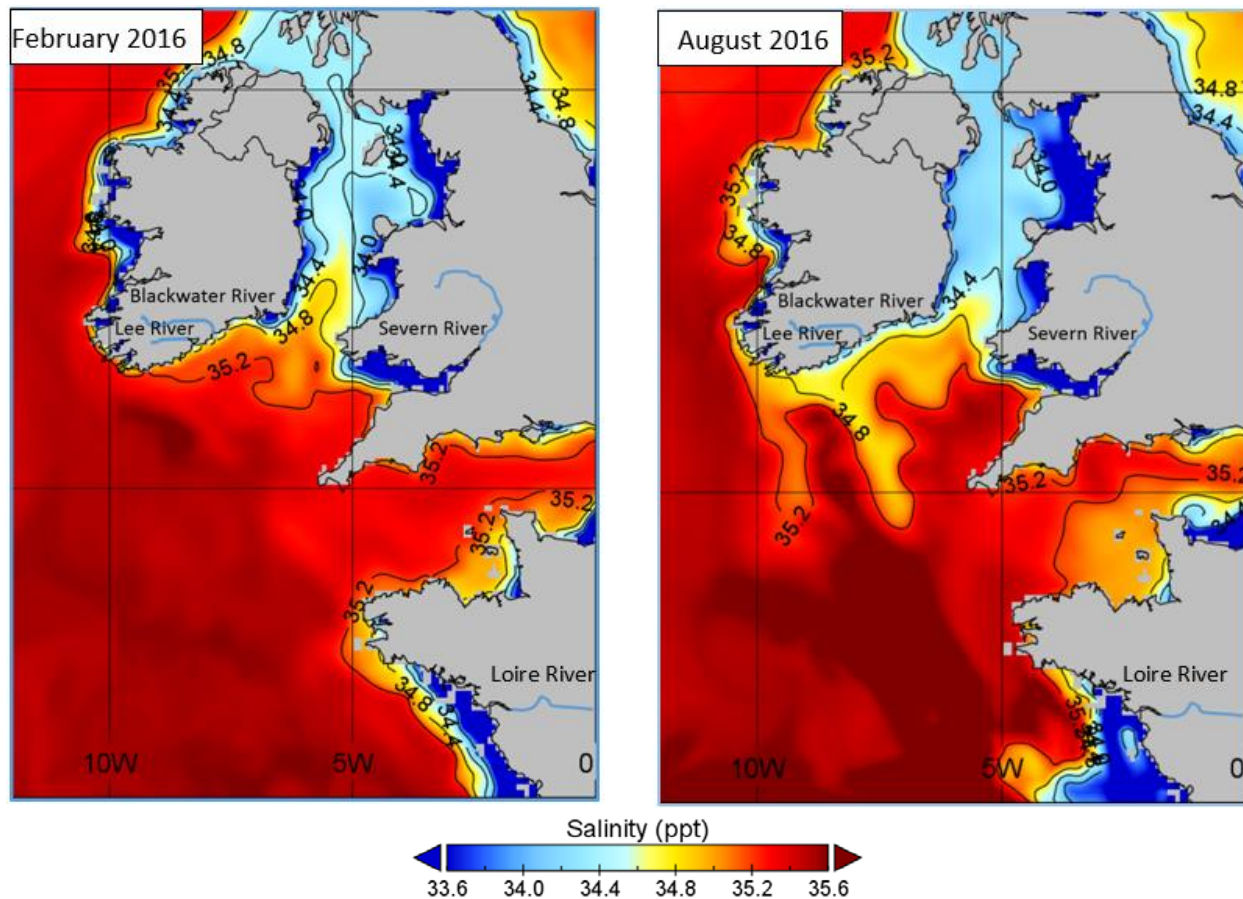
Fig 2.4 Monthly salinity averages depicting the February as the saltiest month (left) and August as the less salty. (copernicus.eu, accessed July 2018)

2.3.5. Tides

The Celtic sea is a tidally driven basin region, where tidal mixing, both horizontally and vertically, substantially influences the water column physical properties (O'dea, E. et al., 2012). The anticlockwise amphidrome in the North Atlantic results in the tidal energy being transmitted from the Atlantic Ocean progressively to the north and to the east in the form of a semidiurnal Kelvin wave. This tidal energy comes from the Atlantic Ocean and progresses across the shelf break into the Celtic Sea, reaching the English Channel and the Irish Sea though Saint George channel with a typical phase lag of 2 hours between the shelf break to the Irish sea.

The tides in the Celtic sea are semidiurnal. The M2 constituent is three times the principal solar semidiurnal S2 constituent. At spring tides S2 and M2 are in phase and the tide range is magnified by a factor of 1.33 while at neap tides they are out of phase and the amplitudes are reduced by a factor of 0.66. The result is that the tide is controlled by the M2 constituent, the average range is 4 m for spring tides and about 2 m for neap tides (fig 2.4), with a small diurnal inequality for the whole lunar period (Uncles, 2007). Average tide ranges grow eastward across the Celtic Sea (Robinson, 1979) (fig 2.4). Superimposed over the regional tidal constituents, bathymetry and bottom friction controls the tide regime around the individual banks. This was particularly noticed as part of the surveys done for this thesis.

Extreme tidal ranges of up to 12 m occur in the Gulf of St. Malo (NW of France) as well as in the reaches of the Bristol Channel, where ranges up to 15 m are observed. These local anomalies are caused by the funneling effect of the wedge-shaped geometry of the coastline, a shallow bathymetry and by a tidal resonance.
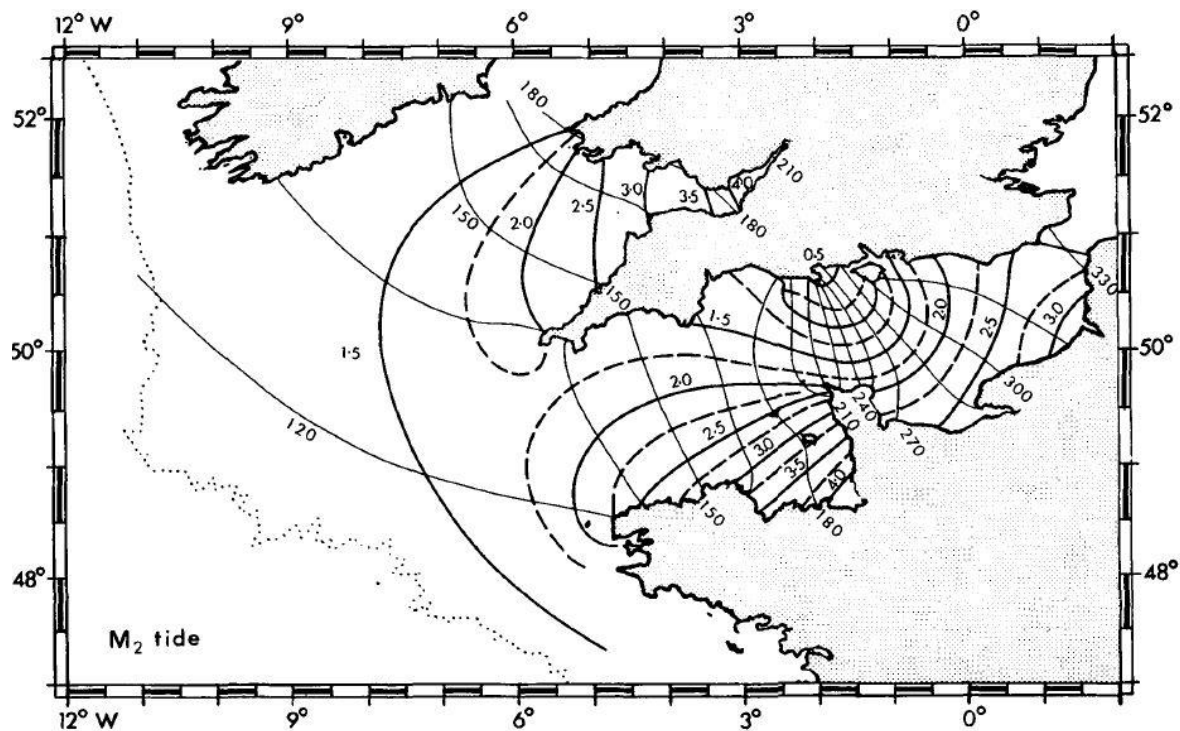
Figure 2.4. Amplitude (in meters) and phase (in degrees) of the semi-diurnal lunar tide (M₂) in the Celtic Sea and English Channel (Pingree,1980)

The tide current intensities are proportional to the tide range, varying from 0.4 m/s near the shelf break to 1 m/s within St. Georges Channel and around NW of France (Huntley, 1980). The tidal streams are elliptical, rotating clockwise offshore and becoming more rectilinear and decreasing in amplitude when they approach the seafloor (Robinson, 1979). Figure 2.5 depicts this phenomenon.

Fig 2.5. Elliptical clockwise tidal flows are observed in the SW Celtic Sea, becoming rectilinear as they approach the bottom as an effect of the increasing seabed friction. (Plot by the author). Note the likelihood of enhanced internal wave generation at the shelf break and over mid-shelf banks.

Regarding the vertical distribution of tidal currents, for most of the Celtic sea shelf, the tide flow over the seafloor produces friction stress that decreases the stream speed near the seafloor, producing a bottom boundary layer. In about 100 m deep mixed water column, the strength of the tidal stream at 1 m above the bottom is about half the surface stream (Uncles and Stephens, 2007). This enhances shear of the seasonal thermocline inducing baroclinic tides. Where the topography varies, there is the potential to trigger internal waves (fig 2.6).

Fig 2.6. Schematic of the thermocline extension and perturbations over a temperate continental shelf

2.4 Seasonal stratification in the Celtic Sea

In the Celtic Sea, mixing by wind at the surface and by tide from the bottom results in a highly mixed homogeneous water column from late Fall until the beginning of spring. On average, from May to September, the mean wind intensity is half that of winter (Pingree and Le Cann, 1989) and it diminishes surface mixing significantly. The balance between increased solar heating, reduced surface turbulence and tidal mixing produces a sharp thermocline that stratifies the water column into two distinct mixed layers, warmer above and cooler below it (Pingree, 1982). The horizontal extension of the stratification depends on the local ratio between depth and tidal mixing (Simpson & Hunter, 1974). This stratification, and therefore the thermocline, firstly appears in the outer shelf and progresses eastwards as it develops, reaching the coastal areas after one month (Sharples et al, 2013). Figure 2.7 illustrates this process. Only occasional summer storms disrupt the thermocline in this period. In September, as the average wind intensity is higher the surface mixing is increased but the remaining surface heats still keeps the stratification. In October, the thermocline is already retreating and by early December it is completely eroded by surface mixing and cooling and tidal mixing from below (Pingree, 1982).
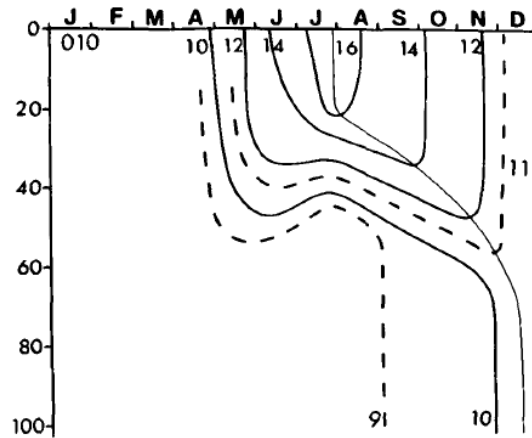
Fig 2.7. Changes in vertical temperature structure in central Celtic Sea during 1975. Dashed line indicates the time of maximum temperature at any depth (Pingree et al., 1976)

The transition zones that separate thermally stratified waters from well-mixed waters are called tidal mixing fronts and they are major structural features of the boundaries of the Celtic Sea that controls the biological environment by supporting primary production and biomass. (Sharples, 2010). The tidal fronts appear at the same time as the thermocline, firstly moving into the western English Channel and northern Celtic Sea. The most important ones are the Celtic Sea front in St George channel and the Ushant front situated in Northwest Britany. Figure 2.8 displays their geographical locations. The tidal fronts migrate back and forth over ~10km during the tidal period. The surveys considered in this thesis were well SW of the Celtic Sea front and thus in strongly stratified waters. Figure 2.9 highlights the stratification layout.
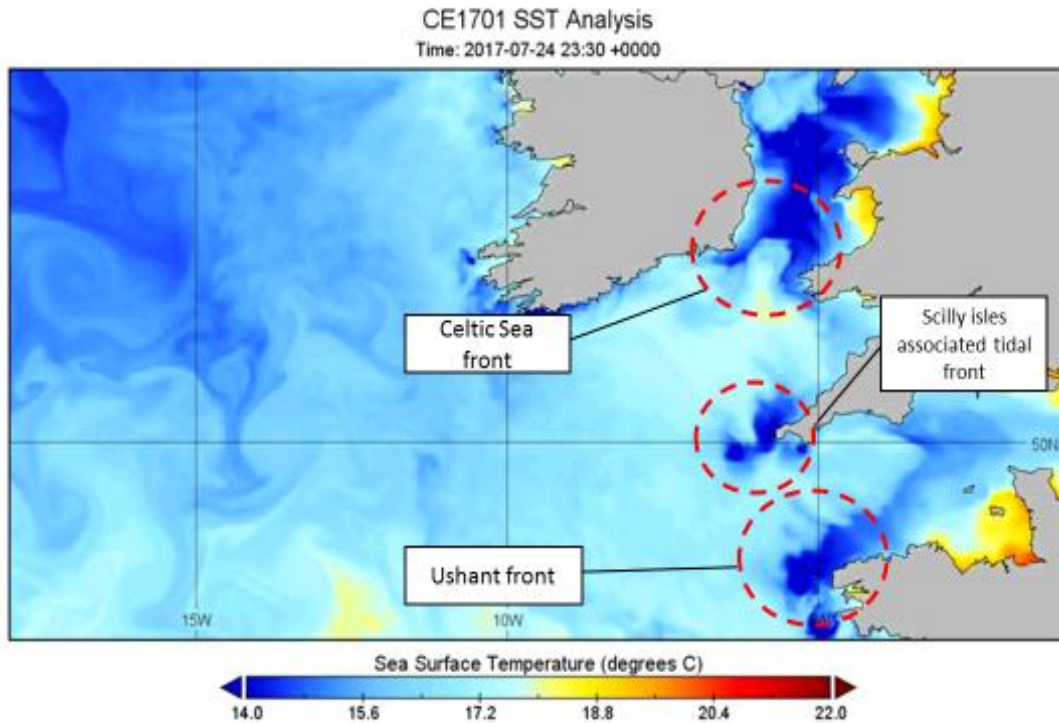
Figure 2.8 Copernicus model SST during CE1701 survey. Summer sea surface temperature help discriminate the tidal fronts in the Celtic Sea since at those locations the colder water from the bottom is mixed with the warmer water above.
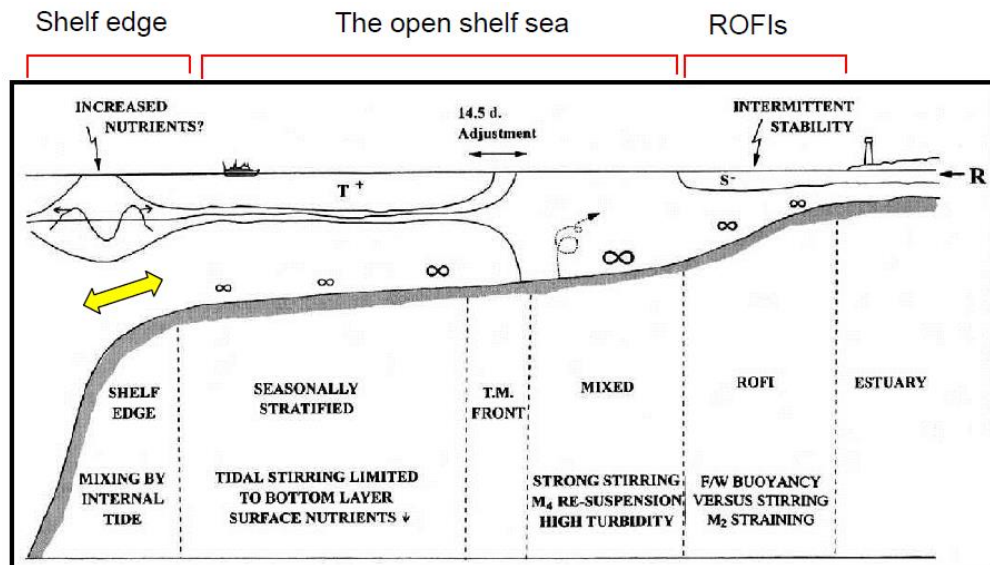
Figure 2.9. Typical stratification scheme in the continental shelf (Simpson, J. H., & Sharples, J. (2012). Introduction to the physical and biological oceanography of shelf seas, 2012)

33

2.5. Internal Waves in the Celtic Sea.

The Celtic Sea is a region of strong and complex internal wave activity (Holt and Thorpe, 1997). The shelf break hosts a rough topography with a series of ridged canyons that connect with Northern Atlantic Ocean and over which intense tidal currents flow both along and across the slope. During the seasonal stratification, the interaction of strong barotropic tides, wind and rough topography generates internal waves that propagates long distances over the shelf (Baines, 1982) as packets of solitons (Sandstorm and Elliott, 1984). This energy dissipates as it progresses shoreward. Enhanced turbulence mixing (Inall et al. 2011) as well as an increased shear in the pycnocline and wave breaking have been observed as the solitons pass along the shelf but the partial contributions of each of these processes to the baroclinic energy decay is still an active area of research (Nash et al., 2012). Recent studies in Jones Bank discovered that internal waves are also generated on the shelf by stratified flow over shallow banks (Palmer et al., 2013). Internal waves of up to 40 m high and about half of the local depth were observed during spring periods and in situations of tidal stream off-bank. This thesis specifically intends to address the associated vertical migration of the velocline due to those internal waves. The data analyzed as part of this study was focused around Labadie Bank, with a similar underwater topography to that in Jones Bank, thus internal waves are expected to be generated locally.

Overall, the Celtic Sea shelf break is considered "*the most relevant tidal conversion hot spot of the ocean in terms of global internal tidal energy flux*" (Baines, 1982) and modifies the local oceanographic conditions. The internal waves produce an intense vertical mixing that brings up to the surface nutrient rich cool water from bellow. (Pingree et al.,1981), leading to an increase of phytoplankton growth. The productivity of the international fishery in the region is believed to be a direct result of this active oceanography (Sharples et al.,2013)

Over much of the Celtic Seas the physical environment is dominated by a simple competition between tidal mixing and surface heating, which in turn controls the seasonality of biochemical

cycling (Pingree et al.,1981). The surveys examined in this thesis were carried out in July/August

2017 at the peak of the summer stratification.

CHAPTER 3

THE COPERNICUS MARINE SERVICE

As part of this thesis, available sources of synoptic oceanographic observations were investigated to aid in comprehending the likely spatial and temporal variability of the mixed layer depth in the Celtic Sea. By far the most relevant available information source is the Copernicus Marine Service, a free and comprehensive EU service that provides models and observations of interest for the hydrographer. This chapter summarizes the organization, functionability and products available within this programme and it goes on to describe the observed Mixed Layer Depth (MLD) variability predicted by the model in the Celtic Sea.

3.1 Copernicus programme overview.

Copernicus is the observation and monitoring programme of the European Commission to provide autonomous operational Earth observation capacity to the European Union. It is based on data acquired from dedicated EU owned satellites (Sentinel missions), satellites operated by other European organizations (EUMETSAT and ESA) as well as satellites belonging to non-EU countries. It is also based on in-situ observations put at the disposal of the programme by the EU members and international research organizations. Copernicus is coordinated by the European Environmental Agency.

The Copernicus programme renders services in six areas (atmosphere monitoring, marine environment monitoring, land monitoring, climate change, emergency management and security) to EU, national and regional institutions and to the private sector and individual users. For the purpose of this thesis, the Copernicus Marine Environment Monitoring Service is described in more detail.
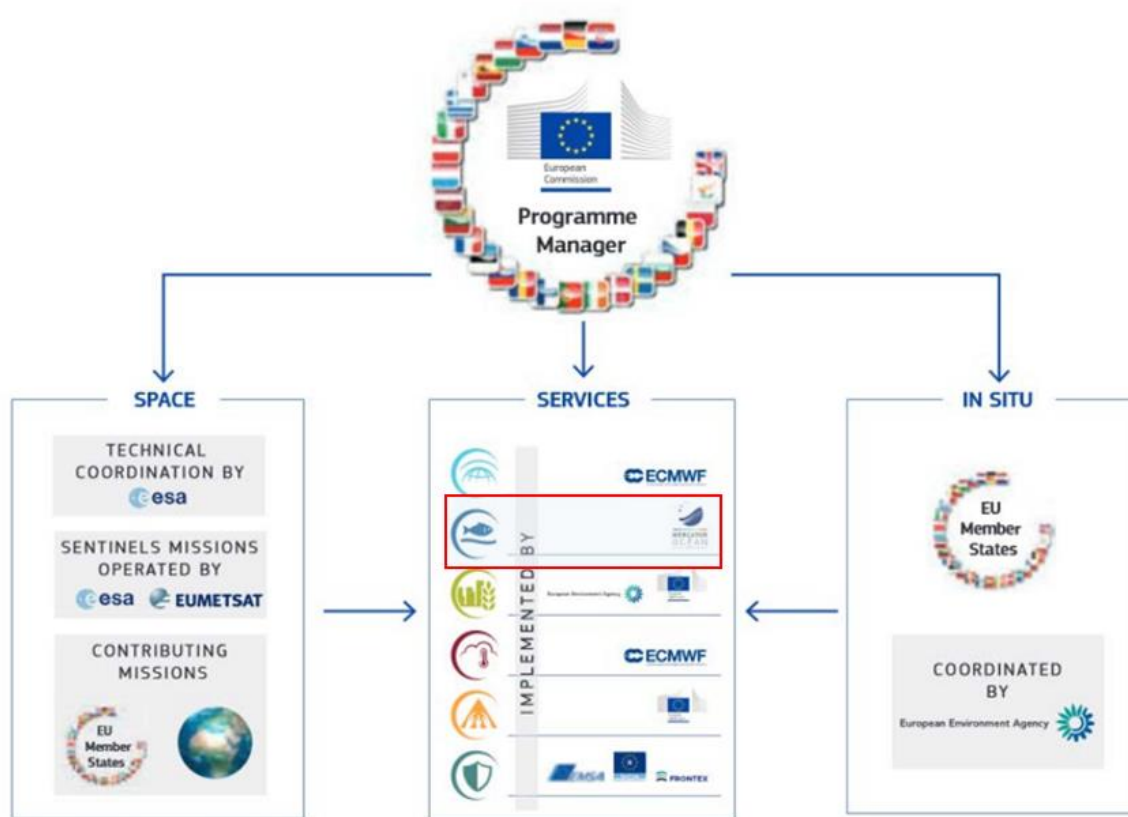
Figure 3.1. Copernicus programme scheme. The Copernicus Marine Environment Monitoring Service is highlighted in red.

3.2. The Copernicus Marine Environment Monitoring Service (CMEMS).

In order to implement the EU Marine Strategy Framework Directive to effectively protect the marine environment across Europe, the Copernicus Marine Environment Monitoring Service became operational in May 2015 as part of the Copernicus programme. Mercator Océan, a private non-profit research center manages CMEMS. It is funded by French institutions involved in operational oceanography such us the CNRS (National Center of Scientific Research), IFREMER (French Research Institute for Exploitation of the Sea), IRD (Institute of Research for

Development), Météo-France, SHOM (Hydrographic and Oceanographic Service of the French Navy) and the CNES (the French Spatial Agency).

4.2.1. Products provided by CMEMS

The main goal of CMEMS is to provide free open access to information on the physical state and marine ecosystems from the global ocean and the European regional seas. CEMS supports the following areas of applications:

- Marine safety

- Marine and coastal environment.

- Marine resources.

- Weather, seasonal forecasting and climate.

This support is achieved by providing a full open and free access to regular and systematic information on currents, temperature, wind, salinity, sea level, sea ice and biogeochemistry in the form of Near-Real Time (NRT) analysis, forecast and the reanalysis of the collected data. This information is obtained by integrating observations from satellites, in-situ and 3d numerical models (K. Von Schuckmann et al. 2016).

Clearly, for operational use in hydrographic survey, the provision of temperature and salinity or sea level could be of great service in refraction and vertical referencing.

3.2.2. CMEMS structure

The Copernicus Marine Service works over a distributed model of service production along the participating European organizations involved in operational oceanography. Firstly, a series of Thematic Assembly Centers (TACs) collect the satellite and the in-situ ocean observations and secondly the regional Monitoring and Forecasting Centers (MFCs) uses this data to generate numerical models for the global ocean and for six pre-established regional areas. The MFCs cover the areas defined as Regional Ocean Observing Systems (ROOS) (figure 3.2), namely:

- Arctic Ocean.

- Baltic Sea.

- European North-West Shelf Seas.

- Iberia-Biscay-Ireland Regional Seas.

- Mediterranean Sea.

- Black Sea

- Global ocean.

Both TACs and MFCs production centers are coordinated by a Central Information System (CIS).

For this thesis, the IBI model is directly relevant and was thus investigated.
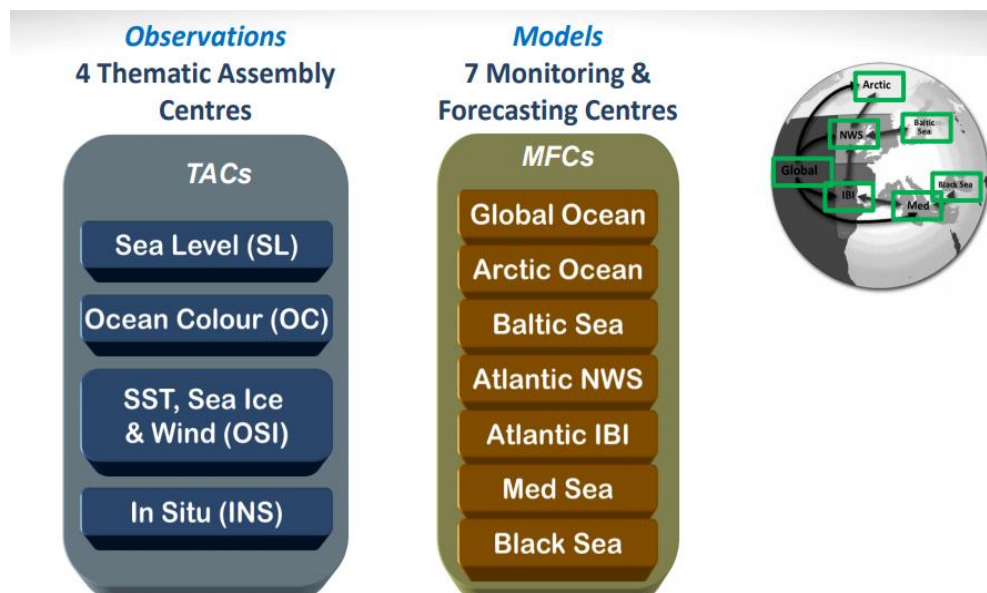
Figure 3.2 System overview of the Copernicus Marine Environment Monitoring Service chain.

Thematic Assembly Centers (TACs)

CMEMS Thematic Assembly Centers collect, process and perform the quality control of the satellite and in-situ data in order to validate models and to serve applications and services (Petit de la Villéon, 2017). There are four TACs, each one specialized in a determined working area but all of them provide products for the global ocean and the regional seas

TAC SEA LEVEL

The Sea Level (SL) TAC provides sea level products from different satellite altimetry missions (SENTINEL 3 , JASON and SARAL) for the MFCs and external users in the form of along-track data and gridded datasets , generated both in real time (3h) and reprocessed offline (6 months). Collected Localization Satellites (CLS), a research French company, is in charge of the altimetry data processing and qualification and renders the following products:

- Sea surface heights with respect to the mean sea level and to the geoid.
- Significant wave height in near-real time over the global ocean area.

The sea surface heights are of high value in hydrography for validating open ocean tidal regimes.

TAC Ocean Colour

The Ocean Colour (OC) TAC, led by The Institute of Atmospheric Sciences and Climate (CNR-ISAC), delivers high-quality core ocean colour products based on sensors onboard satellites such as MERIS (ESA), SeaWiFS and MODIS (NASA), VIIRS (NOAA) and Sentinel 3 (ESA).

For each ocean region, OC TAC delivers two sets of products:

- Phytoplankton chlorophyll concentration, for the global ocean and and the six regional seas.

- Inherent Optical Properties (IOPs), such as absorption and scattering, the diffuse attenuation coefficient of light at 490 nm , Secchi depth (transparency of water), spectral Remote Sensing Reflectance , photosynthetically available radiation, Colored Dissolved Organic Matter , and the Suspended Particulate Matter.

While of undoubted interest, this is only of secondary interest to hydrographic surveys. For example phytoplankton blooms might indicate local upwelling.

TAC OSI (SST, Sea Ice and Ocean Wind Satellite Data)

The OSI TAC is coordinated by the Norwegian Meteorological Institute which leads and collects, processes, and distributes sea surface temperature (SST), surface winds and sea ice (SI) data products derived from radiometers (infra-red and microwave), scatterometers and Synthetic Aperture Radar (SAR) satellite missions.

In the region of interest, the temperature and the winds are the major forcing factors for the hydrodynamic model NEMO (Clementi, 2017) which is used to predict the sound speed structure. Also, as with any marine operations, forecasts of sea state are paramount in survey planning.

TAC In-situ data (INSTAC)

In addition to the remotely sensed data, in-situ (ship, buoys, etc) and measurements of oceanographic parameters are a major additional source of information.

The In-situ TAC is a distributed system based on already existing EU oceanographic projects and services and organized around the global ocean and the 6 ROOS. It provides a research and operational framework to develop and deliver In Situ observations and derived products based on such observations. INSTACs do not deploy any sensor since it is provided from different EU and

international observing systems not funded by CMEMS. These observing system comprehends a wide range of sensors, such as:

- Bathythermographs.

- Bottle data.

- Oceanographic CTD profiles.

- Scanfish profiles.

- Drifting buoys.

- Devices for automatic collection of scientific data on commercial ships (Ferrybox).

-Gliders.

-Fixed buoys or mooring time series.

-ARGO profilers.

-RF river flows.

INSTAC deals with this multisource collection of heterogeneous data to perform a homogenized quality control and data validation. The following Near Real Time (NRT) and reprocessed (delayed mode, DM) products are distributed to the Marine Forecasting Centers (MFC) for assimilation or validation into their numerical ocean models and to the CMEMS users as well:

-Temperature and salinity: global and regional, produced in Real T (all) and DM (all).

-Currents: global and regional, produced in NRT (global, NWS, MedSea, Baltic).

-Sea level: regional, produced in NRT (IBI, NWS, Baltic).

-Biogeochemical: global and regional, produced in RT (all) Wave data (NRT and later REP).

The integration of situ measurements provides the ground truth of the vertical distribution of the information in the water column that is necessary to elaborate the models along with the sea surface only remote sensing observations. Even when only low spatial density observation are

available, the 3D models can be updated with these true in-situ observations to make the output closer to the truth, and thus of more value to the operational hydrographer.

The INSTACs are coordinated by IFREMER (France). There are six regional in-situ data production center for each area of responsibility and each center has its own coordinator as it can be seen in figure 3.3.
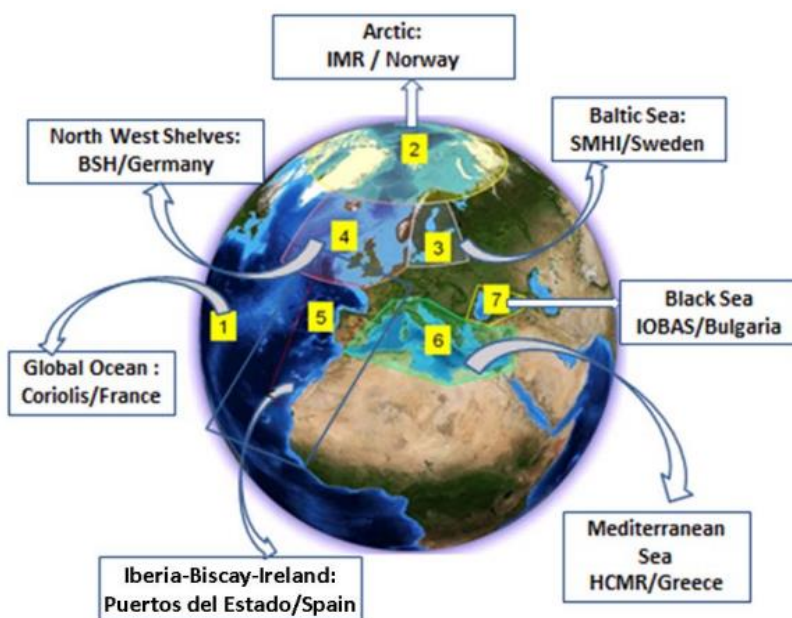
Figure 3.3. In Situ TAC components. Puertos del Estado (Spain) coordinates the IBI area.

Monitor Forecasting Centers (MFC)

Monitoring and Forecasting Centers (MFC) compute numerical models from the datasets provided by the TACs. In this manner, the MFC generate reanalysis (last 20 years), analysis (present time) and 7-day forecast of different ocean parameters regarding ocean circulation, biochemistry and waves. There are seven MFCs: six for the regional seas (ROOS) and one for the global ocean. Each MFC (regional and global) corresponds to one INSTAC center. For a real-

time value to users, all of these observational data needs to be combined with physical models to predict the current or future state of the ocean.

For the purpose of this thesis, the MFC of interest is the "Puertos del Estado" center that manages the Iberia Biscay Irish (IBI) model.

3.3 Products and reports

The following figure show a resume of the products delivered by the CMEMS producers (TACs and MFCs). A complete description can be found in the CEMS online portal.

PARAMETER	MODEL			SATELLITE (surface ocean)		INSITU	
	25years in the past	Today	10-day forecast	25years in the past	Today	25years in the past	Today
Sea Surface Height	x	x	x	x	x	x	x
Temperature	x	x	x	x	x	x	x
Salinity	x	x	x			x	x
Waves	x	x	x				
Currents/velocity	x	x	x			x	x
Mixed Layer Depth	x	x	x			x	x
Sea ice	x	x	x	x	x		
Turbidity/Transparency				x	x		
Reflectance				x	x		
Nutrients	x	x	x			x	
Primary Production	x	x	x			x	
Oxygen	x	x	x			x	
Plankton	x	x	x			x	
Wind				x	x		

Figure 3.4. Products delivered by CMEMS. Those used in this thesis are highlighted in red.

In this thesis, the hindcast mixed layer depth are compared with our observations (chapter 4) and the sound speed derived from the hindcast temperature and salinity is again compared with our

MVP dips. In the discussion, the feasibility of this forecast of sound speed environment is presented.

3.4. User accessibility

CMEMS products can be freely accessed by any particular user after online registration at the CMEMS web site. (http://marine.copernicus.eu/). A user interface shows the product catalog and the desired product can be found by selecting the corresponding area of interest, the oceanographic parameter and the time coverage. Products can the displayed online and downloaded in NetCDF format either directly or by using python scripts. In this thesis, data were acquired from the IBI area, visualized by using the NASA multiplatform application "Panoply" and eventually merged and processed using custom scripts in Matlab 2016a. Figure 3.5 shows an example of the CMEMS user's online menu.

3.5 The MFC IBI (Iberia-Biscay-Ireland)

For the interest of this thesis, it is relevant to highlight the products rendered by the IBI MFC.

This IBI area covers the North Atlantic waters from 60N (Scotland) to 20 N (Senegal), and from

30 W (Azores Islands) to the Greenwich meridian (English Channel).
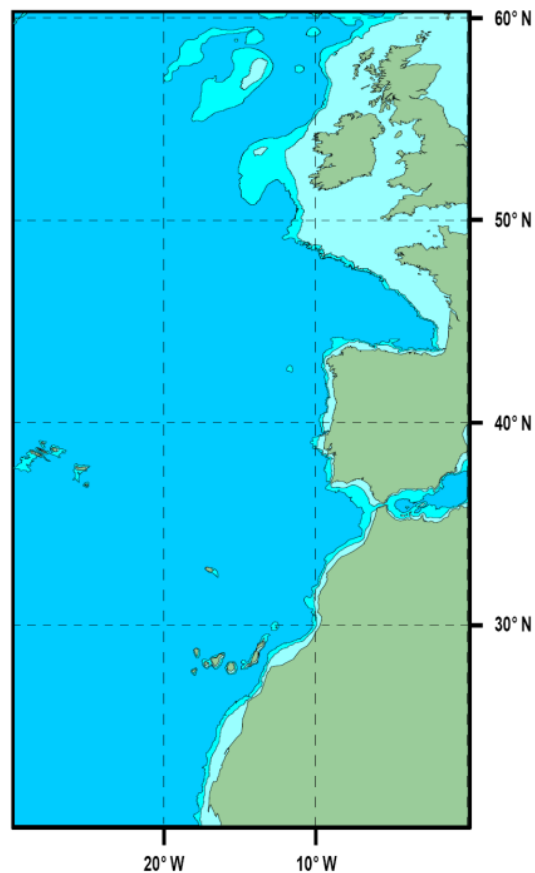
Fig 3.4. CMEMS IBI area includes the Celtic Sea.

The IBI MFC provides daily ocean model estimates and forecasts of diverse physical parameters

for the IBI regional seas (Sotillo et al., 2015). It is coordinated by Puertos del Estado (Spain) and

participated by MeteoFrance, the Spanish Met office AEMET, the Irish Marine Institute and the CESGA Supercomputing Centre.

The IBI physical forecast system is based on a 1/36º NEMO model application (Nucleus for European Modelling of the Ocean) which is equivalent to an average 2 km horizontal resolution grid of temperature and salinity at hourly intervals.

The bathymetry used in the system is a combination of interpolated ETOPO1 (Amante and Eakins, 2009) and GEBCO-8 (Becker et al., 2009) databases. ETOPO1 datasets are used in regions deeper than 300 m and GEBCO8 is used in regions shallower than 200 m with a linear interpolation in the 200 - 300 m layer.

In the absence of up to date information, or to provide near-future predictions, this data can be interrogated to provide height and sound speed structure in specific hydrographic areas.

3.5.1. The IBI Mixed-Layer Depth.

While the full temperature-salinity structure is available for up to 30 days (on-line), the main interest for this thesis is the depth of the thermocline. For that, CMEMS provide a convenient product, the Mixed Layer Depth (MLD) . It is referred to as the part of the water columns where the properties have been homogenized due to winds, surface heat fluxes, or other processes taking place at the air-sea interface. At the bottom of the MLD, a relatively strong gradient is observed: if there is an abrupt change in temperature, then the layer corresponding to that change is called thermocline; if there is an abrupt change in salinity, one refers to it as a halocline. The MLD is where many processes related to physics (wind forcing and heat exchanges), chemistry (dissolution of CO_2) and biology (phytoplankton production) take place. Therefore it is essential to properly measure and understand its variations. For this thesis, this is important

because the MLD is directly related to the depth of the thermocline, as previously explained in chapter 2.

There are two main methods to evaluate the MLD knowing the vertical profiles of temperature and salinity. The first one is setting fixed thresholds for either of these parameters so that the MLD value is determined as the depth where that threshold is exceeded, since T and S are approximately homogeneous within the mixed layer region and there is a pronounced gradient beneath this layer. The second method consist of setting a variable threshold for the same variables so that the depth of the gradient of those parameters are obtained. For both methods, a minimum depth of, normally, 10 m is considered so that the strong diurnal temperature cycle in the top few meters of the water column are no taken into the calculations and thus, do not influence the model (Boyer Montégut et al.,2004)

CMEMS defines MLD as the last vertical level at which the density is greater or equal to the density at the surface + 0.01 kg/m3, starting from 10 m depth (Lellouche, 2016). On an hourly basis, the MLD is derived from the operational model and thus can be directly compared to the location of the thermocline, as defined by the collection of the MVP samples. The real advantage of the MLD predictions is that they are spatially complete at 2 km horizontal and with ~3 m vertical layer increment for the continental shelf in the Iberian-Biscay-Ireland area. By making a spatial map at hourly interval, the evolution of this MLD surface may be assessed over tidal and circadian time periods. From that one can start to investigate how the thermocline is responding to the tidal and wind forcing throughout the survey. A snapshot of the MLD model for the CE1701 survey area is display in figure 3.5 further below.

The MVP dips, in contrast, are only collected at one point at a time (at ~1/2 hourly interval). For example, by the time the vessel steams from one side of Labadie Bank to the other (~ 3 h), the tidal phase has significantly changed. Thus, by combining the in-situ truth of MVP and the spatially extensive predictions of the MLD, one can start to assess the actual pattern of the forcing that is going on.

Finally, the 3D hydrodynamic models provided by CMEMS have a hydrostatic foundation and thus cannot reproduce KH waves and short wavelength internal waves that are seen when using multibeam system (length scales lesser than 1 km). The model node spacing is 2 km and thus only represents the regional (4 km+ length scale) variations in the thermocline. Nevertheless, from the data examined in this thesis, there is a considerable variability of those length scales, which would be of importance for ray trace calculations.
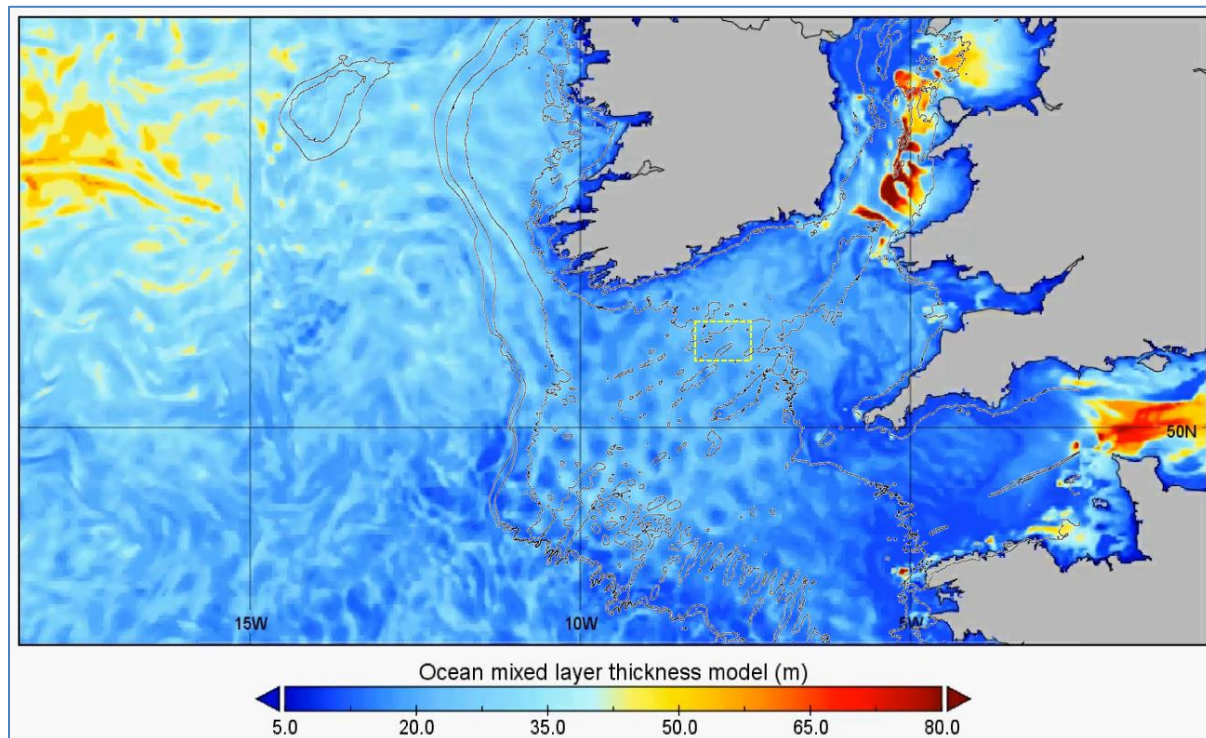
Figure 3.5. MLD model of the Celtic Sea (IBI area), including CE1701 survey area (yellow dashed rectangle). Vertical oscillations of the thermocline can be inferred at the shelf break as well as standing waves over the banks on the shelf.

3.5.2. Physical insights provided by the MLD map.

Now that we can view the predicted MLD across the Celtic Sea and watch it evolve over hourly (i.e. tidal) time scales, there are several important features that are notable and can be clearly observed such as the well-defined tidal fronts, moving back and forth with the semidiurnal tidal pumping, the generation of internal waves at the shelf break and even standing internal waves

at the shallow banks in the central area. Particularly an oscillating depression is observed around the survey area in Labadie Bank (figure 3.6).
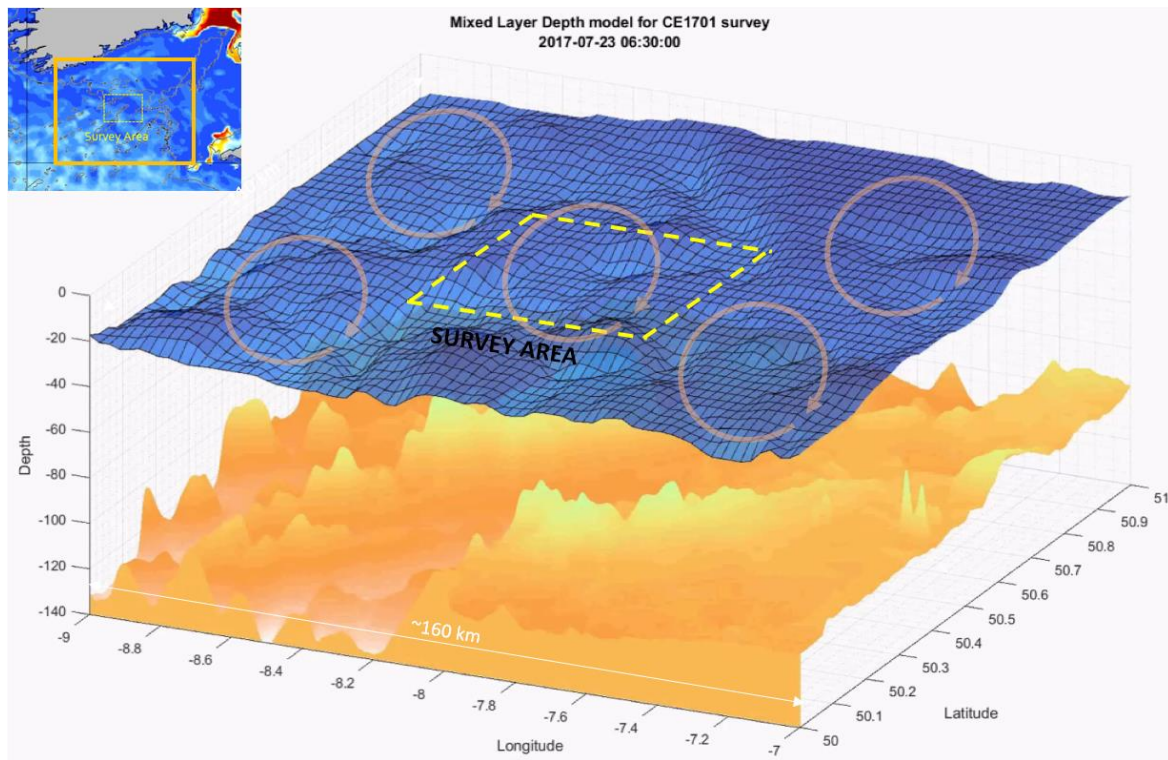
Figure 3.5. Snapshot of the hourly MLD model in the survey area, highlighting standing waves oscillating clockwise

CHAPTER 4

METHODS

4.1 Data collection

The R/V Celtic Explorer (figure 4.1) is the largest research vessel of the Irish state and is run by the Marine Institute, the national sea mapping agency. This multipurpose ship conducts oceanographic, hydrographic, geological and fishery investigations in Irish and other European shallow and deep waters. The vessel specifications are listed in table 4.1.

Figure 4.1. R/V Celtic Explorer (www.marine.ie)

From July 23 to August 6 of 2017, Celtic Explorer carried out the CE1701 survey within the INFOMAR programme, the Irish national seabed mapping project between the Geological Survey and the Marine Institute. This survey was conducted in the vicinity of Labadie Bank, in the central area of the Celtic sea. The weather conditions were favorable most of the time with light breeze winds and slight seas except for two 48h gale events which occurred on the 26-27 of July and on the 1-2 of August. Spring and neap tides were observed during the first and second week of the survey, respectively. A tidal model for the central area was obtained from the Web Tide HR Global model (figure 4.3). An intense internal wave activity was expected according to the season of the year, the tidal flow and the existing underwater topography.

General specifications	
Dimensions	65.5 m (length) x 15 m (beam) x 5.8 m (draft) decreasing to 8.5 m with drop-keel
Tonnage	2425T (GRT) , 725T (DWT)
Speed	Maximum speed 16 knots, service speed <10 knots
Scientific equipment	
Acoustic sensors	MBES Kongsberg EM302, EM2040, EM1002
	SBES Kongsberg EA600, EK60 (18-38-120-200 kHz), SP-70
	iXBLUE ECHOES 3500 T7 Chirp Sub-bottom profiler RDI Sea Surveyor 75 kHz ADCP
Positioning	Primary: C-Nav 3050 (Z corrections). Secondary: Seapath 330+
Other equipment	MVP 200 fitted with one AML Smart SVP. CTD Seabird SBE 911

Table 4.1. R/V Celtic Explorer specifications (www.marine.ie)

The survey plan comprised lines 50 km long east to west that were oriented over a relatively flat 100 m deep seafloor surrounding the 60 m shallow Labadie bank. The first lines started north of the bank, moving subsequently southwards over it. The vessel steamed at 8 knots while sampling the sound speed every ~40 min with an AML-200 Mobile Velocity Profiler fitted with an AML Micro Smart probe. It resulted in an average along track sampling resolution of 8 km. Figure 4.2 shows the survey area and displays the hourly distribution of the sound speed measurements. Each line took approximately 3 hours to be surveyed, thus comprising one quarter of the tidal cycle.
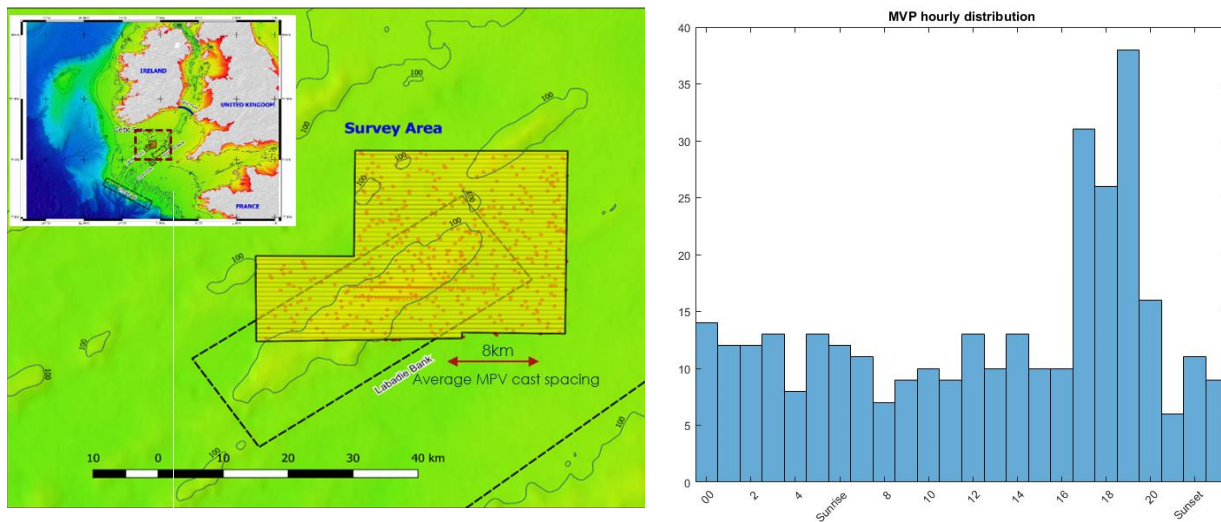
Figure 4.2a (left). CE 17-01 Survey area in the Celtic Sea. (MVP casts shown as red dots). Figure 4.2b (right). MVP casts hourly distribution. The denser period between 1700 and 1900 UTC is explained due to an experiment to achieve the highest sampling resolution on Labadie Bank.

The acoustic imaging from the water column was obtained by using multi frequency channels of a narrow band split beam echosounder SIMRAD EK60. It was operated at 18, 38, 120 kHz along 97 survey lines. The working parameters are detailed in table 4.2.

Sensor	Specifications
SIMRAD EK60	Frequencies: 18 kHz, 38 kHz, 120 kHz (wavelengths: 8.3 cm, 4.0 cm, 1.3 cm)
	Beam width: 11˚ (18 kHz), 7˚ (38 kHz), 7˚ (120 kHz)
	Power : 2000 w (18 kHz), 2000 w (38 kHz), 500 w (120 kHz)
	Pulse length: 1ms , PRF: 1 pps
AML Micro Smart Sound Velocity	S.V. accuracy (+/-): 0.025 m/s. Precision: (+/-) 0.006 m/s Pressure accuracy (+/-) 0.05%. Precision: (+/-) 0.01 m

Table 4.2. Sensors specifications
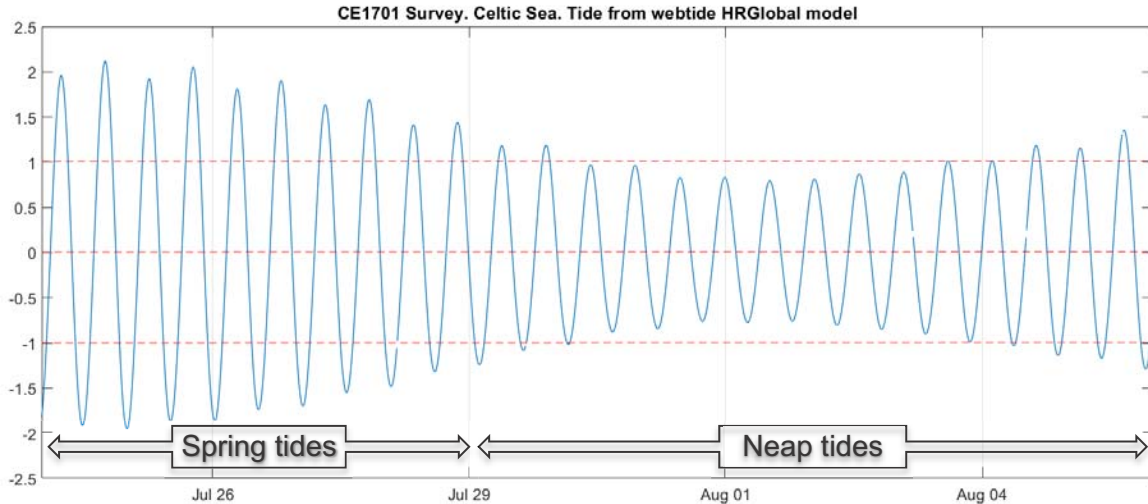
Figure 4.3. Tides for the two-week mapping survey from WebTide HR Global in center of survey area, showing an initial period of spring tides followed by neap tides

4.2 Data processing

The EK60 multispectral raw echograms were firstly converted to the OMG (Ocean Mapping Group) custom format. The original 16-bit data from the EK60 telegram containing power levels adjusted by Time Varying Gain and pulse length corrections were normalized to the mean echo strength. As a result, reprojected 8-bit images were created. One image per channel and per line, where each ping was georeferenced, generating pixels of 0.2 m (height) by 10 m (width) each. Then, for each one of the three frequency channels, an arbitrary dynamic range within red (18 kHz), green, (38 kHz), and blue (120 kHz) spectrum was set to produce an RGB overlay so that the prevailing color at each region of the image highlighted the frequency of higher response. The sound speed profiles were depicted on the top at their specific locations and a combined RGB plot was created for each line by merging the individual channel echograms (figure 4.4).
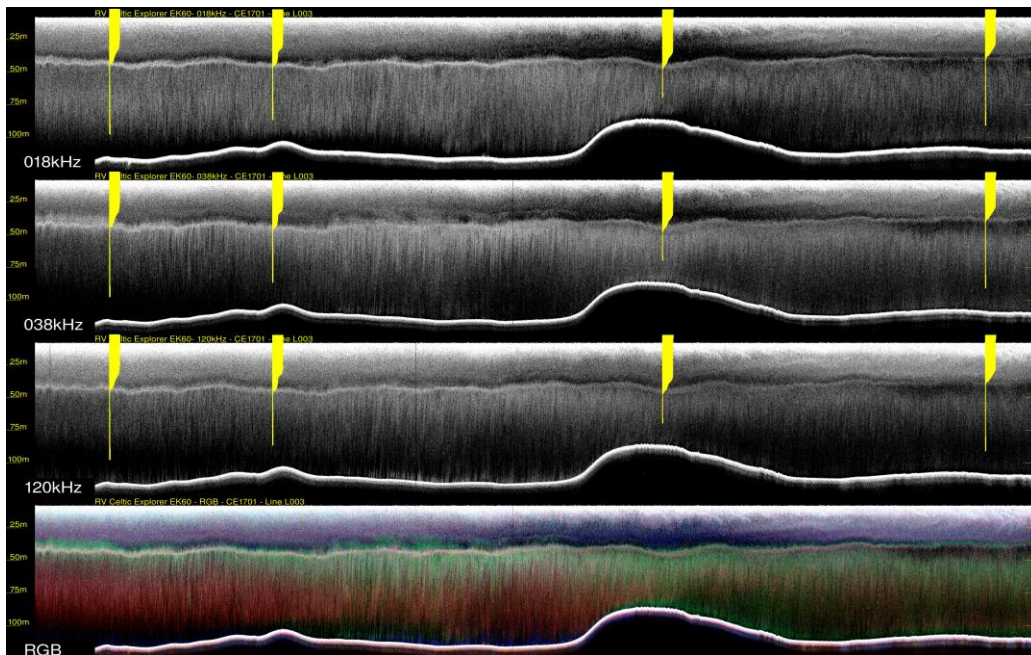
Figure 4.4. EK-60 reprojected echograms for 18,38 and 120 kHz where the sound speed profiles are on top. A fourth RGB multispectral combination (red for 18 kHz, blue for 38 kHz and green for 120 kHz) is shown at the bottom. Strong perturbations in the scattering can be seen over the shallow Labadie Bank.

A first visual inspection indicated that the bottom of the velocline had a strong correlation with the bottom of a fluctuating scattering layer, as expected, and that there were some differences in each channel since the volume backscatter is frequency dependent. Also, it could be noticed the presence of two horizons in some areas (figure 4.5). Regarding the vertical oscillations, the diurnal migration could be clearly discerned as well as notable perturbation over Labadie bank.
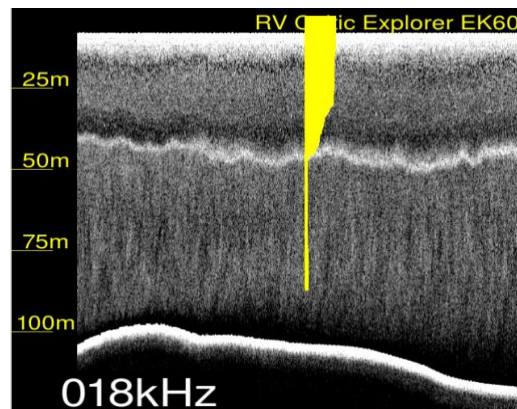
Figure 4.5. Two horizons are present at different depths. In this case, the deeper scatter correlates with the base of the thermocline.

A total of 503 valid MVP sound speed profiles were parsed to extract the velocline. Firstly, a composite overlay was plot, revealing a clear and repetitive pattern. The profiles seemingly shared a very similar double vertical iso-velocity structure separated in average 20 m/s and a velocline depth variability of approximately 20 m (figure 4.6).
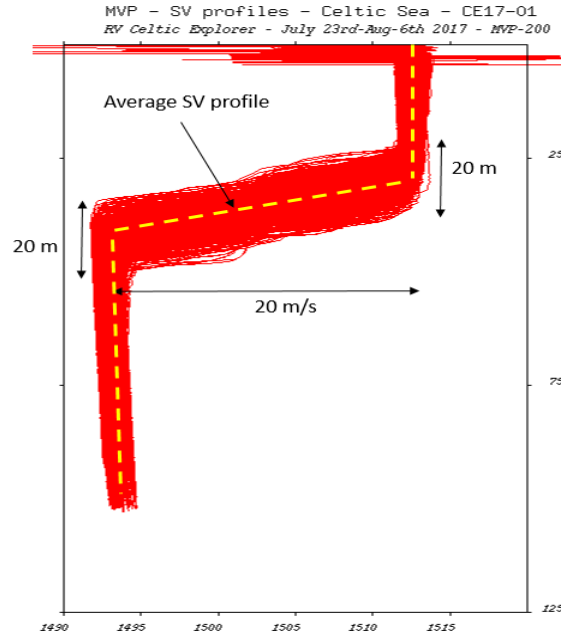
Figure 4.6. CE1701 Sound Speed Profiles composite plot. It shows the common iso-velocity structures and the vertical variability of the velocline.

The numerical values of the top and bottom of the velocline were determined using a custom Matlab script by finding the deeper and shallower gradient existing between 10 and 60 m that were falling above half of the gradient maxima for each profile. Figure 4.7 illustrates an example plot from the script.
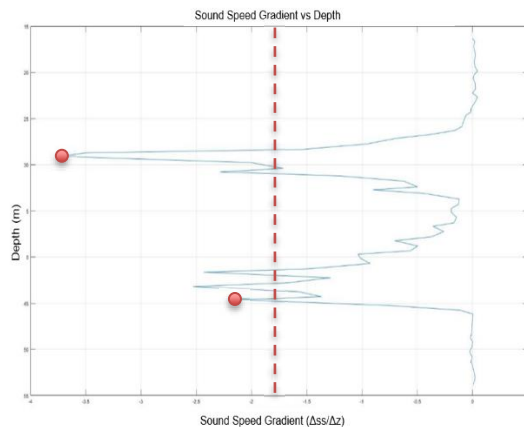
Variable	Mean	Standard Deviation
Velocline top	$1511.44\ ms^{-1}$	+/- $0.66\ ms^{-1}$
Velocline bottom	$1493.50\ m$	+/- $0.84\ ms^{-1}$
Velocline top depth	$30.30\ m$	+/- $3.74\ m$
Velocline bottom depth	$42.02\ m$	+/- $3.32\ m$
Gradient ($\Delta ss/\Delta z$)	$-1.51\ s^{-1}$	+/- $0.40\ s^{-1}$

Figure 4.7 (left) Sound Speed (SS) Gradient vs depth plot for MVP cast #23. The red dots show the picks for the top and the bottom of the thermocline, corresponding to the shallowest and deepest gradient

Complementing the acquired data, a high resolution 4D model of the Ocean Mixed Layer of the survey area was downloaded from the IBI (Iberia Biscay Ireland) service of CMEMS and compared to the MVP inferred thermocline depths. Average vertical offsets of 10 m and 25 m with respect to the top and the bottom of thermocline were observed. This is explained by the fact that the Mixed Layer Depth is defined in the CMEMS model as the last vertical level at which the density is greater or equal to the density at the surface + 0.01 kg/m3, starting from bottom level (Lellouche, 2016). The outcome of these calculations presents depths consistently shallower than those from the measured thermoclines.

Also, the results showed an inconclusive correlation of 0.5 for either comparisons of the MLD with the top and the bottom of the thermocline but, on the other hand, similar standard deviation values were obtained. Figures 4.8 and 4.9 display a visual graph comparison and table 4.4 resumes the corresponding statistics.

Thus, the MLD pick is a conservative estimate of the true start of the thermocline that is likely to be deeper. Also, it was observed that the IBI model usually generalizes and therefore artificially thickens the thermocline region (figure 4.8).
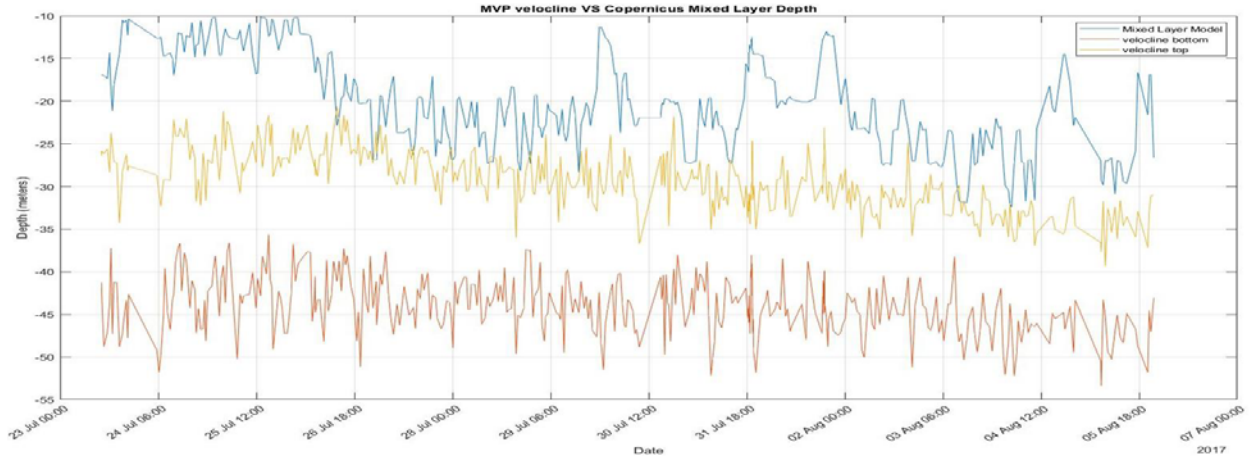
Figure 4.8. Copernicus Mixed Layer Depth vs MVP top and bottom of the thermocline. The Copernicus model for the Mixed Layer is calculated as the depth where density is one per cent higher than on the surface. MVP inferred thermocline depths are calculated as vertical levels of maximum sound speed gradient.
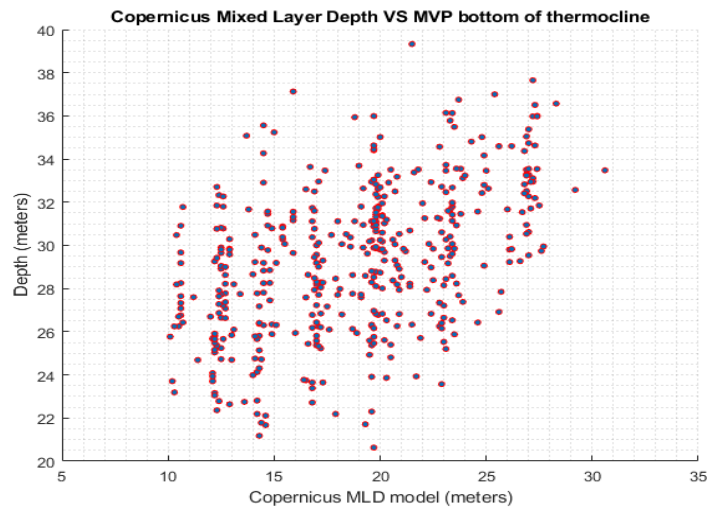
Figure 4.9. Copernicus Mixed Layer Depth vs MVP bottom of the thermocline. Steps in MLD can be seen as the Copernicus model discretizes the solution into 40-z levels

In summary, while the variability is comparable, clearly the CMEMS IBI MLD would not be a good operational model to use directly instead of observations.

	Copernicus MLD	MVP thermocline Top	MVP thermocline Bottom
Maximum value	10.5 m	39.33 m	53.38 m
Minimum value	32 m	20.63 m	35.67 m
Mean depth	19.40 m	29.3 m	44.05 m
Standard dev.	4.77 m	3.41 m	3.25 m

Table 4.4. Copernicus Mixed Layer Depth and MVP thermocline depths statistics. Despite the fact that the MLD is derived from a model and it is calculated with different parameters, the three vertical level have similar variabilities.

4.3 Image Processing of the echograms.

Tracking changes in features from acoustic images of the water column, correlated with those from in situ measurements, is the main goal of this thesis as a method to infer those alterations when direct measurements are not available.

The task to extract the thermocline from the echograms consists of finding a laterally continuous scattering feature that might plausibly be related to the thermocline, determining the corresponding depth and comparing it to the truth, namely the thermocline depth extracted from the MVP samples. These anomalies, corresponding to the biological and microstructure originated backscatter are modulated by the tide, internal waves, K.H. waves and diurnal migration. Since the scattering layer was expected to be mostly influenced by internal waves, depth variabilities of ~20 m over scales of hundreds of meters (Apel, 2004) were expected in the echograms.

The first step to extract the depth of the scattering layer from the EK60 echograms was to select vertical subsets of the images for each frequency at each sound speed profile location. The 8-bit pixel intensity values from each subset were then compared to the vertical structure of the veloclne for each individual MVP profiles (figure 4.9).
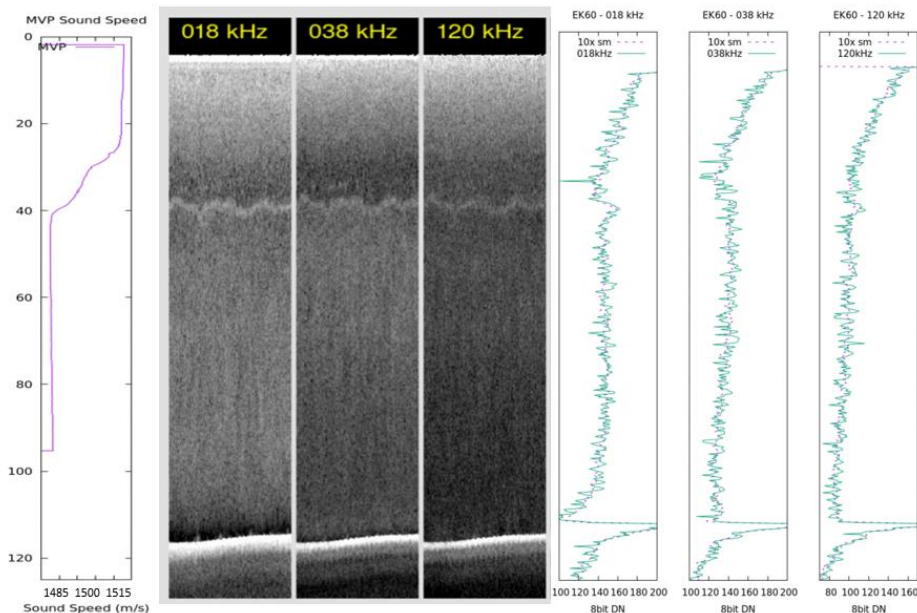
Figure 4.9. Line 01- MVP 02. Velocline structure vs echograms section vs pixel 8 bit intensity profile

Although a layer that appeared to correspond to the thermocline was usually distinguishable in the echograms as a bright and noisy undulation that showed up slightly different for each channel, that anomaly was not immediately and unambiguously discernible in the instantaneous numeric profile corresponding to the pixel intensities.

In order to find and extract this horizontally extensive backscatter layer, several image processing filters were consecutively applied. At this point, it was necessary to define the dimensions of the target features in terms of size in pixels and vertical and horizontal variability. For that, the scattering layer was considered to be at least 1.4 m thick (7 pixels) and vertically varying only over scales of at least 100 m (10 pixels).

4.3.1. Low Pass Filter.

The speckle in the image is generated from different sources. Onboard noise from either the ship's propulsion plant or the electric generators, interferences with other acoustic systems, bubbles in the water, and patchiness of the zooplankton backscattering are some of the most common

61

causes of noise. Superimposed on all this, it is found the stochastic nature of the acoustic backscatter and thus, the inherent presence of the speckle phenomena.

The low pass filter is a basic linear spatial filter that removes high frequency noise by averaging nearby pixels. It is achieved by convolving the image with a spatial mask (box) that has all positive coefficients. They result in smoothed images where the larger the mask, the more averaging, and thus the more noise reduction is obtained. Conversely, enlarging the box increases blurring and diminishes the resolution of the filtered image. Eventually, the size box is determined as a tradeoff between smoothing out the noise and preserving the features of interest.

1/15	1/15	1/15	1/15	1/15
1/15	1/15	1/15	1/15	1/15
1/15	1/15	1/15	1/15	1/15

Figure 4.10. Low pass filter running on a box of size 5x3 pixels. The central value (greyed) is replaced by the average of all intensity values in the box.

Low pass filters of different box dimensions for the filter box were run, ranging from 7 to 41 pixels (70 m to 410 m) horizontally and a fixed 5-pixel (1 m) range vertically. Figure 4.10 illustrates this process.
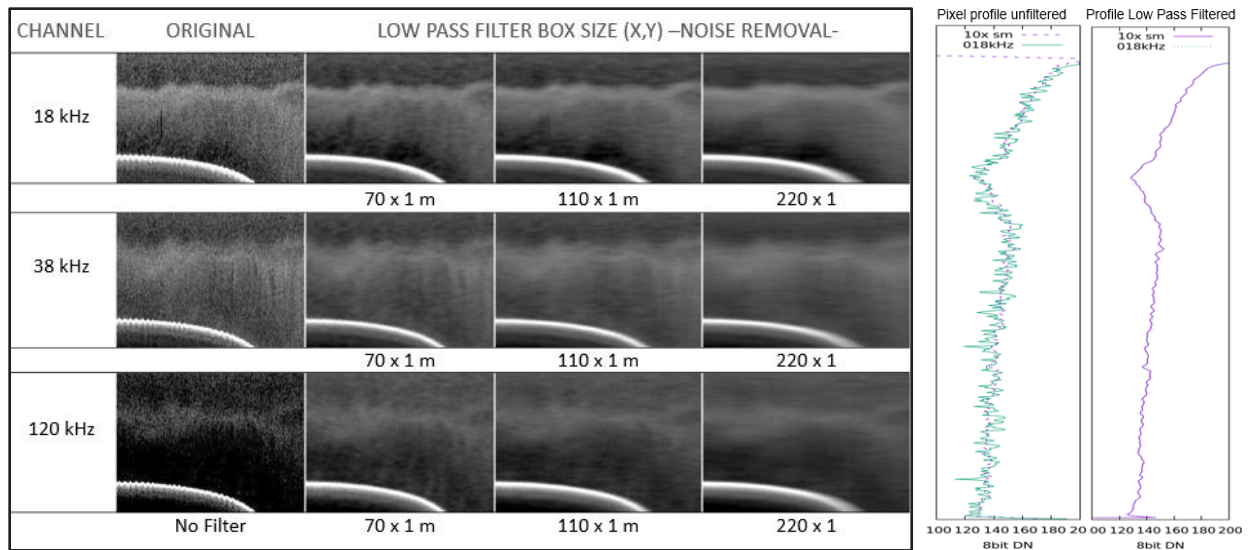
Figure 4.10 (left) Line 01 MVP 02. Smoothing filters results for 7x5,11x5 and 22x5 pixels (horizontal x vertical dimensions). Pixel intensity profile denoising (right).

It can be observed that the noise removal effect is intensified in the image as the dimensions of the kernel increases, but this pixel intensity averaging also dilutes fine details.

4.3.2 Vertical Gradient Filter.

The next step was to detect the edges within the smoothed image. The edges correspond to points in the image where the intensity of the pixel changes suddenly, by running gradient filters. This kind of linear filter returns the first derivative of the image along some preferred direction and have to be run after some smoothing since they are sensitive to noise. Figure 4.11 shows and example of a vertical gradient mask of size 3x3 pixels.

-1	*-1*	*-1*
0	*0*	*0*
1	*1*	*1*

Figure 4.11. Vertical gradient mask of size 3x3. It detects horizontal edges in an image

63

This mask substitutes each pixel value of an image with the difference of the above and below pixel intensities, therefore abrupt changes or edges are made more visible. Vertical gradient filters are adequate to detect features that change most rapidly in the vertical direction. Box sizes from 11 to 61 pixels in height (~2 m to 12 m) and 1-pixel (10 m) width were run along the echogram subsets at the MVP locations. These settings considered the fact that the edges are proportional to the underlying intensity transition and to the variability of the thickness of the features observed in the echograms. These dimensions represent the minimum scale over which a pixel intensity drop will be considered significant. Figure 4.12 displays examples of the vertical gradient filter run over the echogram subset and the resulting numerical profile.
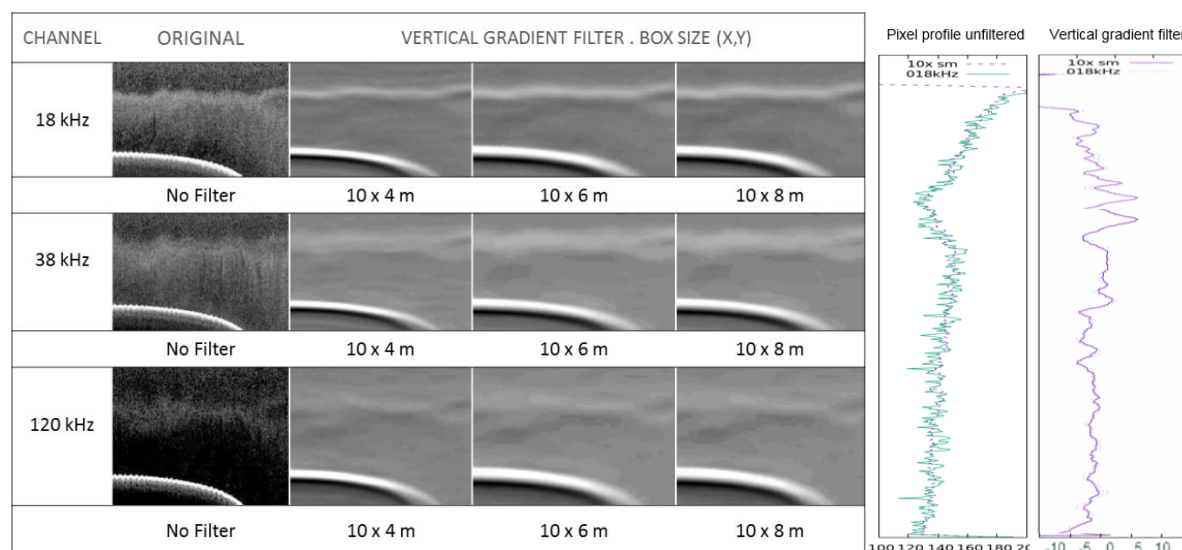
Figure 4.12 (left). Line 01 MVP 02. Edge detection filter results for 1x11, 1x21 and 1x31 pixels (horizontal x vertical dimensions) and pixel intensity profiles before and after the three filtering steps (right).

4.3.3. High Pass Filter.

The end result of the gradient filter was a map of the vertical derivative, understood as how the backscattering changes with depth. For many of the regions above or below the thermocline,

there was a weak but non-zero gradient that could not be considered a boundary. An additional step is therefore needed to highlight the regions where the gradient is changing rapidly over a minimum vertical dimension where a scattering layer is expected to be present. A high pass filter was selected as the final step to remove those gradient changes that are longer than that minimum expected vertical dimension.

The high pass filter has the effect of enhancing pixel contrast over a user-defined dimension. Those regions in which the gradient is only changing gradually will end up being set to zero. Strong gradients will be represented by residual high and low gradient values. The kernel of a high pass filter is designed so that **the brightness of the central pixel is increased and then subtracted from the mean value of the surrounding pixels**. Figure 4.13 shows an example of a 3 by 3-pixel kernel for a high pass filter.

-1/9	-1/9	-1/9
-1/9	1	-1/9
-1/9	-1/9	-1/9

-1/15	-1/15	-1/15	-1/15	-1/15
-1/15	-1/15	1	-1/15	-1/15
-1/15	-1/15	-1/15	-1/15	-1/15

-1/15	-1/15	-1/15
-1/15	-1/15	-1/15
-1/15	1	-1/15
-1/15	-1/15	-1/15
-1/15	-1/15	-1/15

Figure 4.13. High Pass Filter mask of sizes 3x3, 5x3 and 3 x5 (horizontal x vertical dimensions). It enhances edges in an image and it can emphasize a certain direction.

Not only that, high pass filters were run with a box of the same dimensions as those for the vertical gradient filter in the previous step. These dimensions represent the maximum length scale over which a pixel intensity drop will be examined. Figure 4.14 shows examples of the results of various high pass filters.
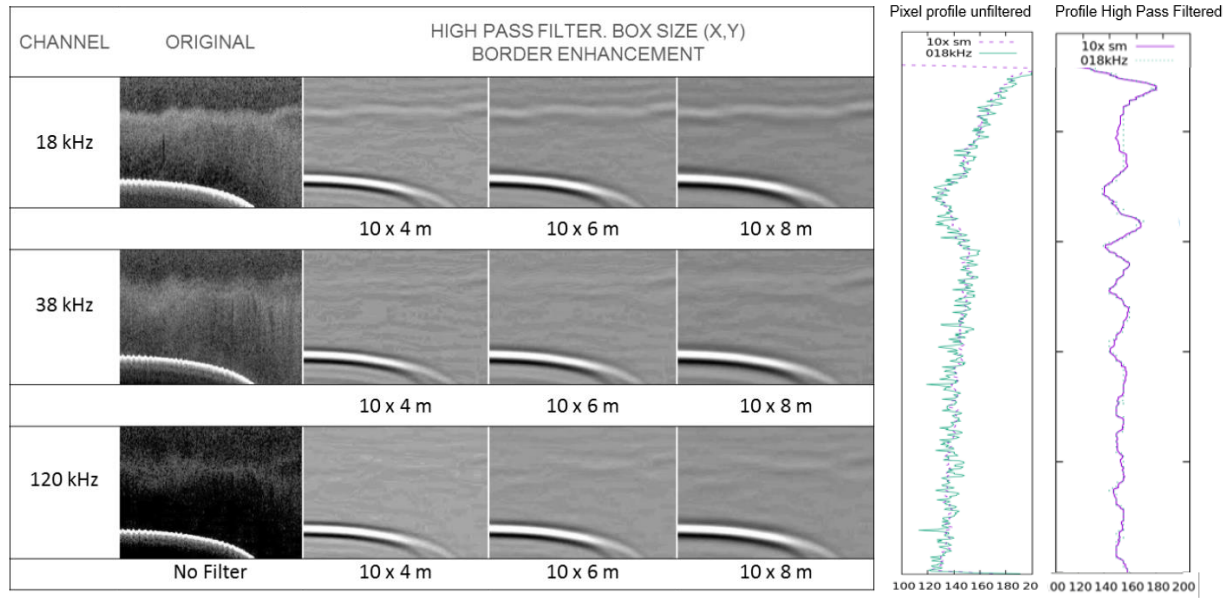
Figure 4.14. Line 01 MVP 02. Edge detection filter results for 7x5,11x5 and 22x5 pixels (left) and pixel intensity profiles prior and after filtering

4.4 Determining the most successful filter combination.

Multiple filter size combinations were investigated on the images, resulting in processed vertical subsets of the echograms centered at the MVP locations and their corresponding 8-bit numerical profiles, fluctuating about zero (represented as 128 in an 8-bit image). This is now amenable for detection of a maximum (or minimum) by defining a user-determined threshold for both pixel intensity changes within a predetermined region of the water column (15 to 60 m depth). Eventually, determining the negative gradient peak will provide the location at which the intensities are dropping most quickly with depth, i.e., the bottom of a high scattering layer.

A certain filter combination was considered unambiguous whenever the anomalies detected in the three frequencies fell above the intensity threshold equal to 2 and these depths were within a confidence interval of +-1 m relative to the MVP depth for the bottom of the thermocline. A solution was considered ambiguous or inconclusive whenever there were 3 extracted depths from the

different channels but they didn't match among each other, thus falling beyond the confidence

interval. Whenever less than 3 depths could be extracted, it was also considered as ambiguous

or inconclusive. Figure 4.15 displays an example of an unambiguous solution where 3 out 3

extracted depths from the numerical profiles resulting after running the image processing filters

are matching the MVP depth for the bottom of the thermocline.
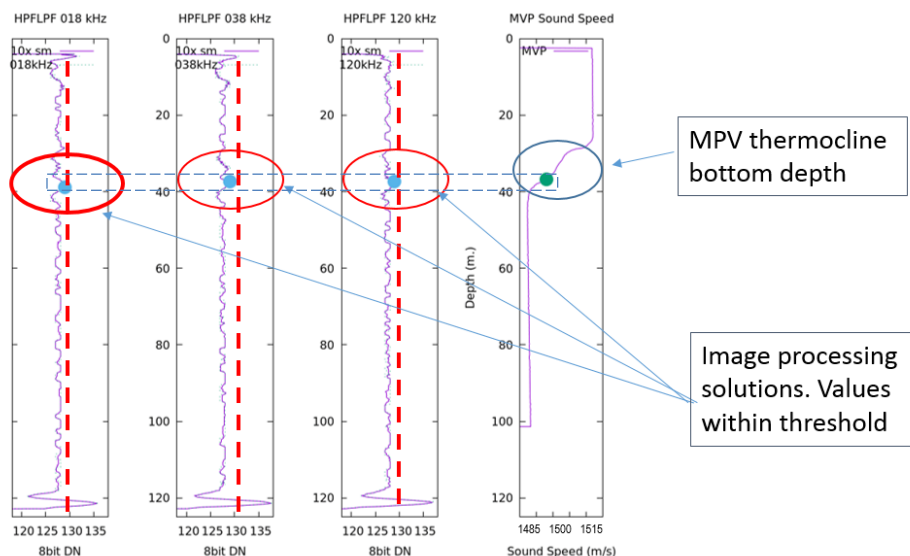
Figure 4.15. Example of unambiguous solution. The numerical profiles for each channel resulting after running the image processing filters are compared to the sound speed structure from MVP #21. Anomalies (blue dots) above an intensity threshold (red dash line) are compared to the bottom of the thermocline depth from the MVP profile. As the anomalies fall within the estimated MVP depth ±2 m, this filter combination is considered successful at this specific MVP location within the echogram.

The most successful size settings were determined by the number of matches between the

image processed thermocline depths and the MVP depths when the same settings were applied

to all the MVP locations. Figure 4.16 shows an example of an unambiguous solution compared

to the other solutions for the same filter settings.
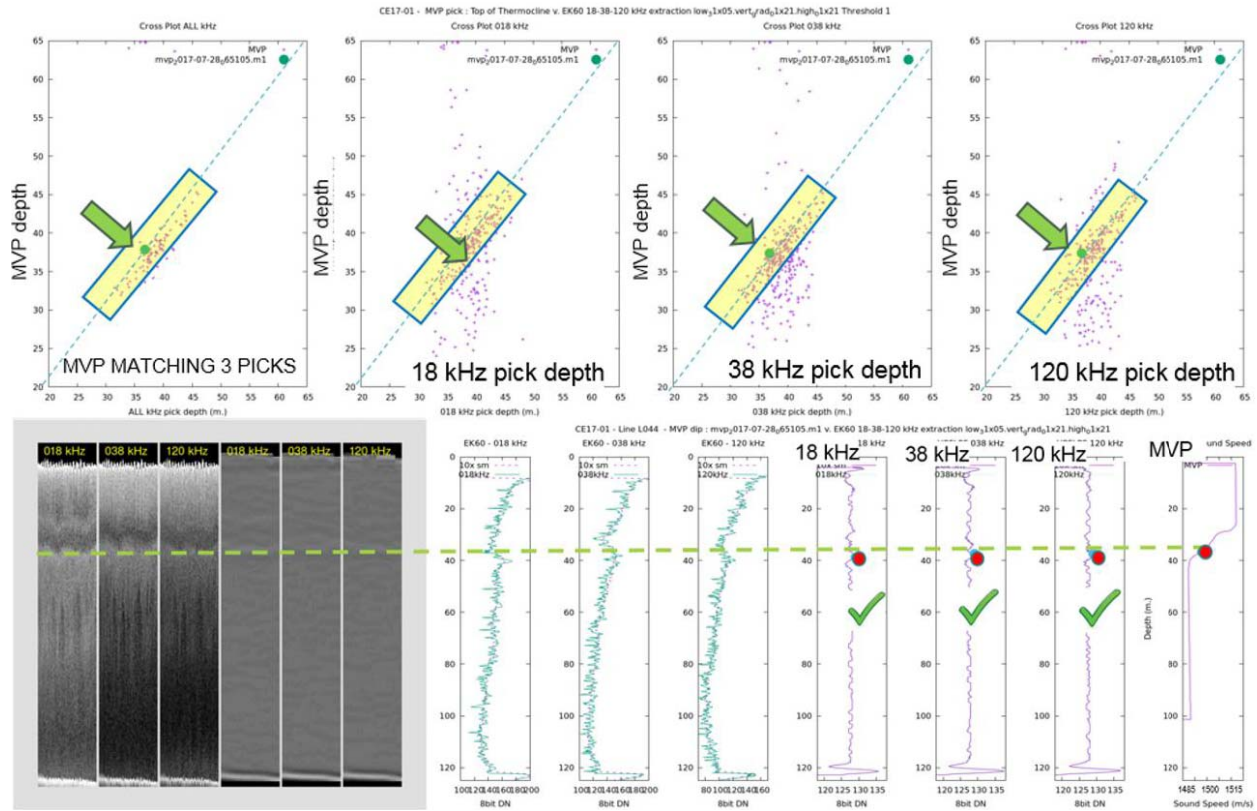
Figure 4.16. Example of an unambiguous solution compared to the results for the same filter settings applied in all MVP locations. Bottom images shows the echogram subsets before and after filtering (left), the numerical profiles before filtering(center) and filtered profiles and MVP sound speed structure (right) where the bottom of the thermocline is highlighted with a red dot. The horizontal dashed green line symbolizes the depth of bottom of the thermocline. Plots at the top display the different depth picks (blue dots) for each frequency compared to the MVP depth. The rectangular boxes represent the thermocline depth acceptance region. Top left plot shows a consolidated layout of the picks all over the MVP locations matching among each other and then compared to the MVP depth. Red dots represent the actual MVP location displayed at the bottom and tick marks emphasizes that the picks are matching the MVP depth.

The results were classified according to the percentage of existing picks within the acceptance region, the width of that acceptance region, the number of channels where the picks where extracted from, as well as the period of the day, namely circadian cycle (24h), daytime (from one hour after sunrise to one hour before sunset), nighttime (from one hour after sunset to one hour before sunrise and twilight (one hour before and after sunrise and sunset).

Eventually, the overall most successful filter combination for all day periods was achieved with the following settings:

- Low Pass Filter: 31 x 5 pixels (310 m width x 1 m height).

- Vertical Gradient Filter: 1 x 11 pixels 9 (10 m width x 2 m height).

- High Pass Filter: 1 x 31 pixels (10 m width x 6 m height).

The physical meanings of the kernels are detailed further below.

Figure 4.17 displays the results where it can be noticed that the thermocline is better resolved during the day rather than the night or the twilight.
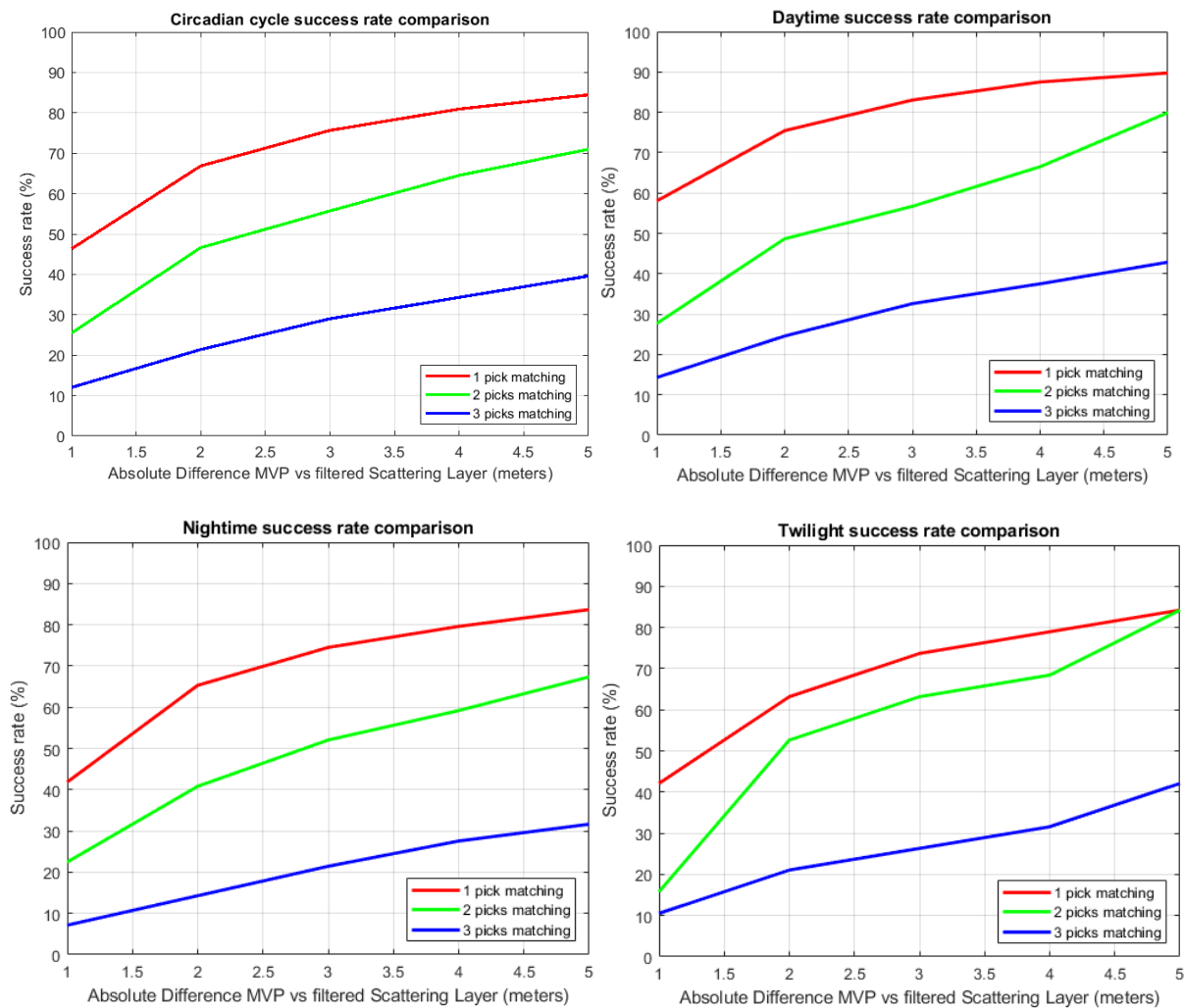
Figure 4.17. Results for the best filter settings (LP 31x01+VF 01x11+HP 01x31) classified according to the period of the day (24h cycle, daytime, nighttime and twilight) and the number of frequencies (picks) matching the MVP solution for the bottom of the thermocline for a confidence interval ranging from 1 to 5 meters.

In a last step, the adequacy of each channel was classified according to the success rate on average (It is depicted in figure 4.18). The 18 kHz frequency was found to be providing a slightly more accurate peak than the others (30% within +-1 m from MVP ground truth, compared to < 25% for the MF and HF channels)
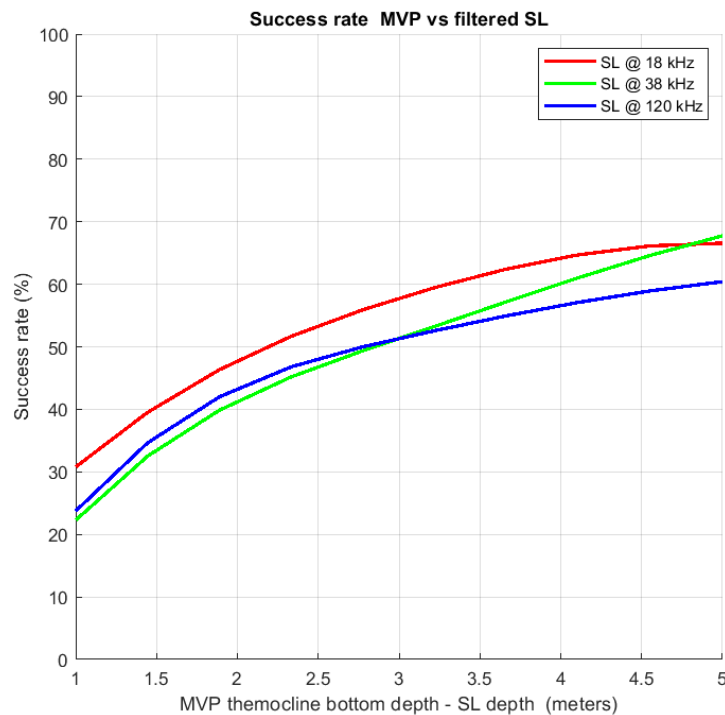
Figure 4.18. Results of the best filter setting for each frequency. The low frequency channel proved to detect the bottom of the thermocline more accurately.

It can be clearly deducted that validating solutions from only one channel is unreliable. Solutions from 3 channels corroborate to a markedly better reliability.

4.5 Physical meaning of the box sizes.

According to the Nyquist sampling theorem, to capture slowly varying thermoclines whose wavelengths are hundreds of meters long, sampling resolutions of at least half of those lengths are required. By selecting a low pass filter, mostly applied in the along-track direction , with a horizontal dimension of 31 pixels or 310 m, wavelengths shorter than twice that length, i.e., 620 m, will not be adequately captured.

Regarding the gradient filter run over the vertical direction with a box size of 1x11 pixels, it detects edges greater than ~2 m and then they are highlighted with the high pass filter over dimensions shorter than 31 pixels or ~6 m in the water column.

4.6 Thermocline detection algorithm.

The whole echogram sequence was processed using the best filter settings previous described. Visual results for line 01 are presented in figure 4.19.
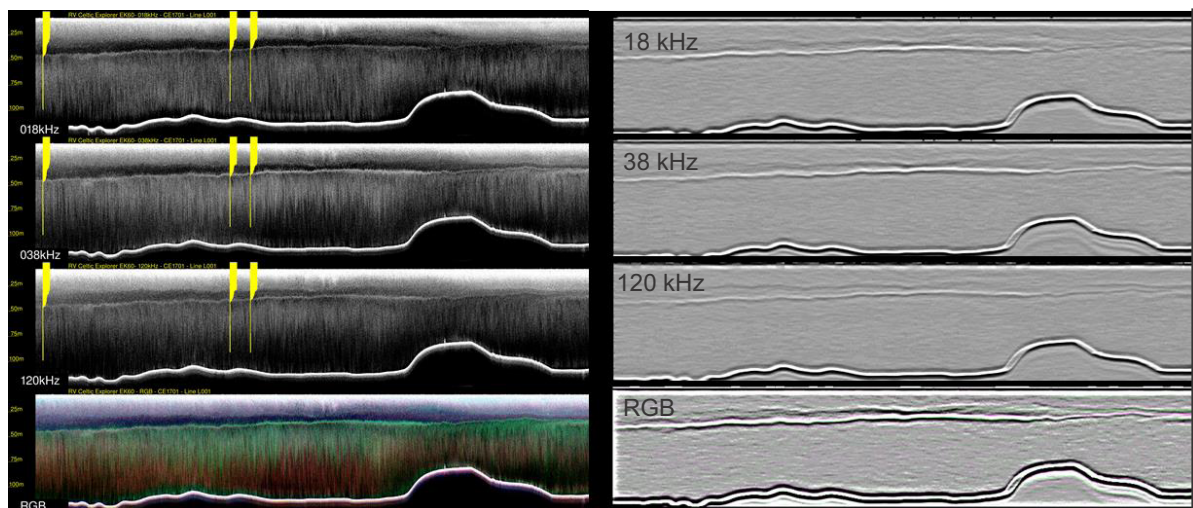
Figure 4.19. Line 01 unfiltered echograms with MVP overlays (left) and filtered echograms after running the best size settings (right). The greyscale RGB plot (bottom right) shows a composite image from the 3 filtered echograms.

The next step was discretizing the thermocline depth all over the echograms. For that, a Matlab custom script was used to process the images and detect the shallowest and the deepest intensity contrasts in each single vertical profile (ping) along the filtered echograms and above a threshold. The output of this process consisted of a time series of markers located at depths corresponding to the top and the bottom of the thermocline. These results, presented in figure 4.20, show consistency for the detection of the bottom of the thermocline but erratic results when tracking the top instead. This occurred when a clear top wasn't present and then the bottom was tracked in its place.
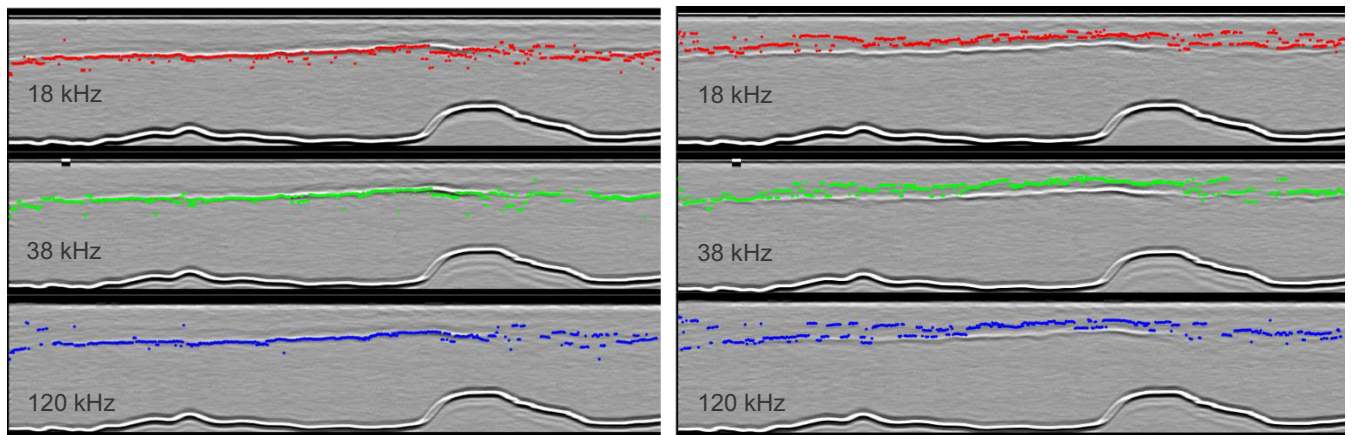
Figure 4.20. Bottom (right) and top (left) of the thermocline detection by selecting the shallowest and the deepest highest intensity contrast for each one pixel wide vertical section.

In order to extract a series of single values for the bottom of the thermocline out of the different multichannel solutions, the deepest value within each individual vertical profile was selected after the assumption that the bottom of thermocline falls on the deepest vertical level of highest contrast in the water column. These resulting series were filtered by running a Hampel filter. Hampel filters are advanced median filters that remove outliers within a moving data window by replacing the central value with the median value when it differs from the median by more than a certain number of standard deviations (Hampel,1974).

It can be expressed as follows, where W_k^K is the moving data window and tS_k stands for the number of standard deviations:

$$W_k^K = \{x_{k-K}, \dots, x_k, \dots, x_{k+K}\}$$
$$m_k = median\{x_{k-K}, \dots, x_k, \dots, x_{k+K}\}$$
$$y_k = \begin{cases} x_k, & |x_k - m_k| \leq tS_k \\ m_k, & |x_k - m_k| > tS_k \end{cases} \qquad (2)$$

The Hempel filter was run over all the echograms using a moving window width of 25 pixels (250 m) and a threshold of two standard deviations.

Figures 4.21 and 4.22 summarize the thermocline detection algorithm walkthrough for line 02 and presents an overlay of the filtered thermocline on the original RGB composite.
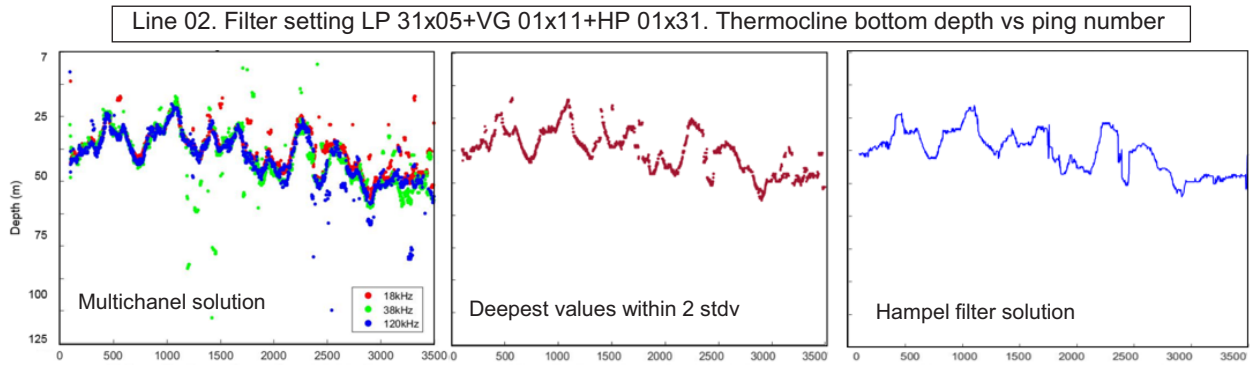
Figure 4.21. Line 03. Thermocline bottom multispectral depths after image processing the ecograms (left). Selection of deepest solutions within 2 std from mean (center). Hampel filter run over deepest values (right)
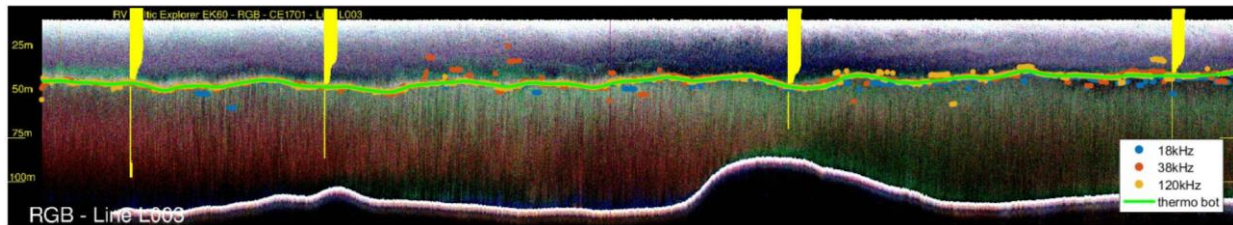
Figure 4.22. The final solution for the bottom of thermocline (green line) as compared with the multichannel discrete solutions (blue, red and orange dots) are presented over the unfiltered RGB overlay. MVP structures are presented in yellow.

73

4.7. Modeling the effect of the vertical oscillation of the thermocline in the ray tracing.

Assessing the contribution of the vertical oscillation of the thermocline in the MBES raytracing had to be attained without the knowledge of the oscillation of the top of the thermocline since it could not be effectively tracked through the filtering of the echograms. To overcome this difficulty, the variability of the thickness of the thermocline extracted from the MVPs along the day was parsed, resulting in hourly delta thicknesses of less than 5%. Subsequently, it was assumed the main sound speed structure was preserved over short time scales and that the veloclines were only displaced in the vertical direction (without modifying the distance between the top and the bottom gradients). Figure 4.23 displays the thermocline thickness evolution along the day on average during the survey.

Figure 4.23. The thermocline thickness evolution along the day as extracted from the MVP samples. Vertical dashed red lines highlight the twilight period while the yellow line represents noon time.

Under the mentioned assumption, the impact in the MBES raytracing was modeled. A canonical sound speed profile was created using the average MVP values for the velocline depth, thickness

and slope. Thereafter, a series of synthetic profiles sharing the same structure as the canonical one but shifted up to 10 m up and down from the mean depth were compared to the unshifted profile using the open source application "Sound Speed Manager" from the package Hydroffice developed at CCOM (Masetti et al., 2018) (fig 4.23). Subsequently, the across track vertical errors for a launch angle of 65 degrees for each compared synthetic profile were calculated. A threshold of 0.5 m was set as the maximum TVU allowance for depth uncertainty when detecting short wave length features on the seafloor. This threshold corresponds to about 50% of the total TPU allowed for IHO order 1 survey (+/- 0.5 z relief) and, recognizing that there are many other error contributions, accounts for the subtle seabed geomorphological variations on the Celtic Shelf that corresponds to similar scale undulations over length scales of a few 100 m. Thus, a slowly undulating thermocline could create false misleading geomorphology. As a result, an on-phase curve showed that this limit was exceeded for vertical thermocline displacements greater than 6 m. Figure 4.24 reveals the synthetic profile overlay and the plot showing the effects of the vertical displacements of the thermocline.
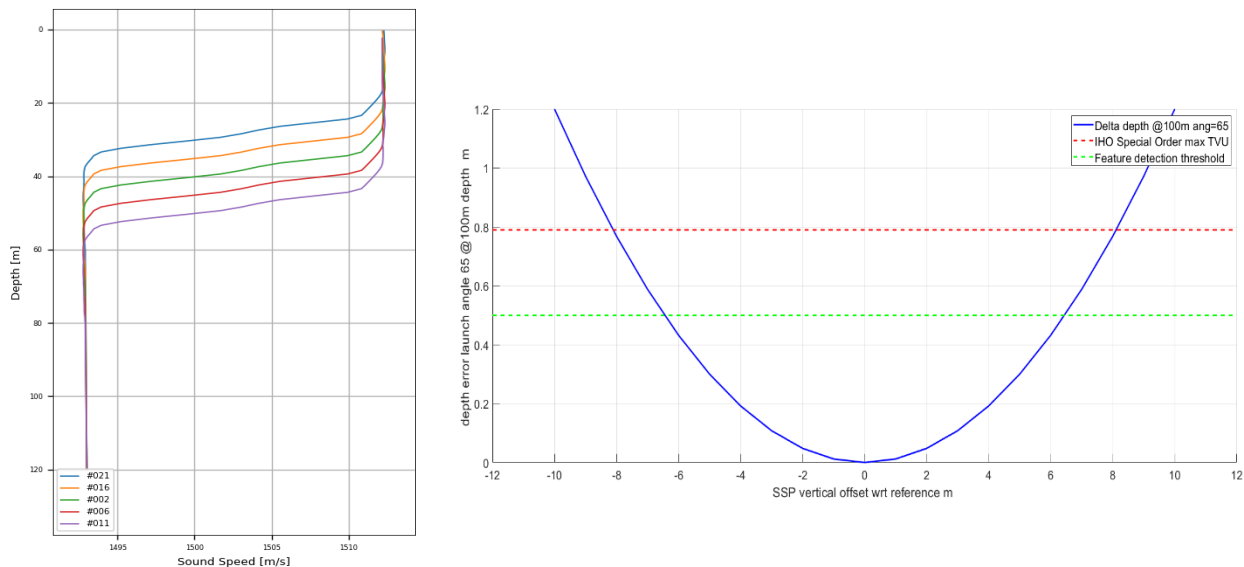
Figure 4.24 (left). An average SSP from the MVP series in presented (green) and synthetic SSPs with the same structure are overlaid 5 and 10 m either above and below. Figure 4.24 (right) The thermocline thickness evolution along 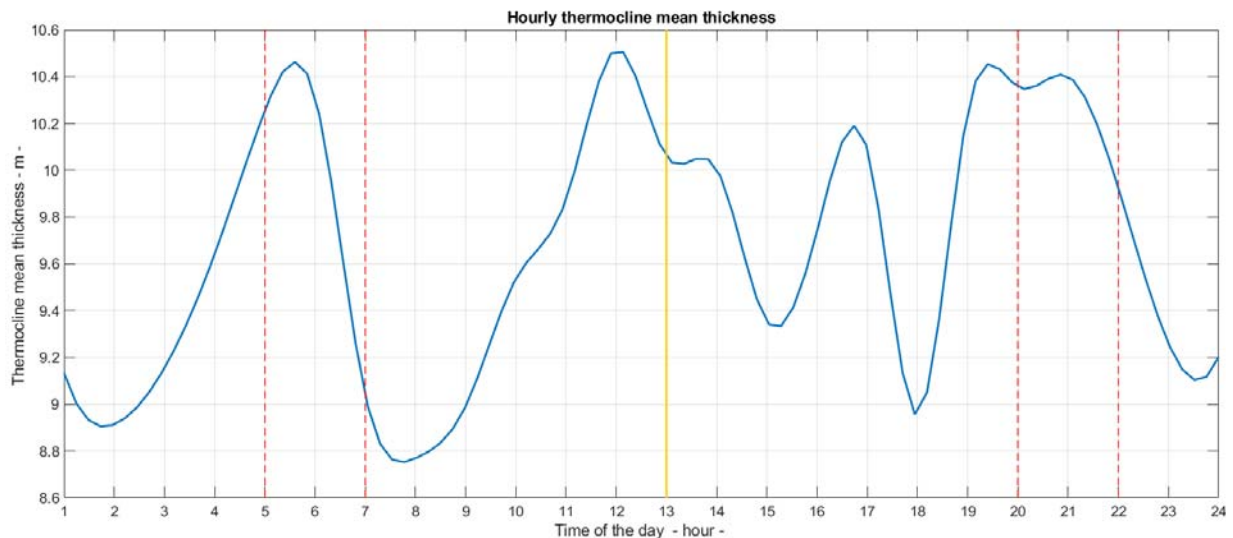the day as extracted from the MVP samples. Vertical dashed red lines highlight the twilight period while the yellow line represents noon time.

4.8. Practical visualization of the TVU limit error excess.

Ultimately, the hydrographic surveyor would greatly benefit from a real-time indicator that the sound speed structure had evolved significantly enough to warrant a new profile.

In a final step, each discrete depth solution for the bottom of the thermocline was compared to that from the previous MVP sample. The representation of these depths on the filtered echogram were colored in green whenever the difference was smaller than the vertical displacement required to exceed the TVU allowance so that it indicated that the existing thermocline oscillation at that time was not drastically degrading the MBES modeling of the seafloor. On the other hand, red color was selected to show vertical oscillation surpassing the threshold. Figure 4.25 displays and example of this process.
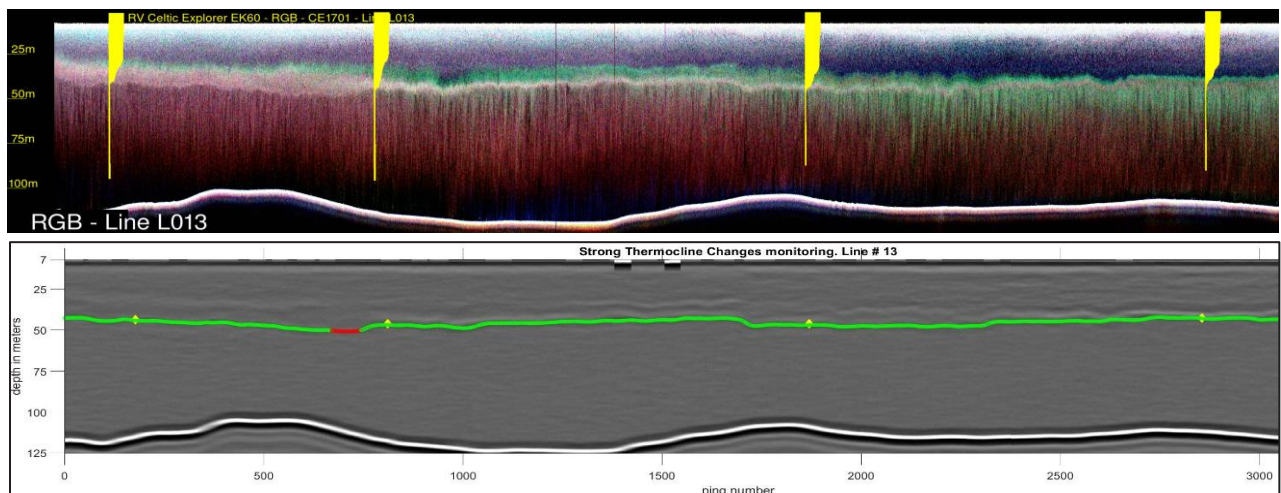
Figure 4.25. Unfiltered RGB overlay for line 13 (up) compared to the depth solution for the bottom of the thermocline colored in red when TPU is exceeded and in green when it is within the limits (down). It is overlaid on the filtered RGB echogram.

The combination of a continuously running thermocline base estimator and a sensitivity analysis of shifts results in a practically usable real time tool to aid the hydrographer about the need to obtain a new profile. An extension of this could be to actually create and use a synthetically shifted profile.

CHAPTER 5

RESULTS

The detection algorithm was executed on the filtered echograms of 96 valid survey lines over the 2-week period of the cruise CE1701, providing continuous depth solutions for the bottom of the thermocline. The most representative solutions for the inferred track of the thermocline in different periods of the day and under the effect of internal waves are shown below. These solutions are graphically presented overlaid (figures 5.1,5.2,5.3 and 5.4, further below) on the corresponding RGB composite of the filtered echograms and compared to the unfiltered RGB and the individual solutions for each channel. Detection estimates at the MVP locations were compared to the depth for the bottom of the velocline obtained from the MVPs (table 5.1).

Day period	Difference MVP - detection algorithm for thermocline bottom		
	<1 m	<3m	<5m
Daytime	52%	79%	94%
Nighttime	43%	69%	78%
Twilight	31%	47%	66%
Spring tides	39%	71%	68%
Neap tides	45%	68%	90%
Overall	46%	69%	86%

Table 5.1. Result for differences between MVP and the detection algorithm solutions for the bottom of the thermocline at MVP locations in the echogram.

On average, the thermocline could be estimated within ±5 m during 86% of the time. This range assumes errors within 5%. All the solutions presented in this section of the thesis are referred to the bottom of the thermocline. The top of the thermocline could not be effectively tracked under any filter settings nor any period of the day. This can be explained by the surface turbulence getting through the upper water column and diffusing the scattering layer corresponding to the

top of the thermocline. This turbulence did not go deeper to the bottom of the thermocline, which is closer to the bottom boundary layer and is affected mostly by phenomena originated close to the seabed.

5.1. Daytime.
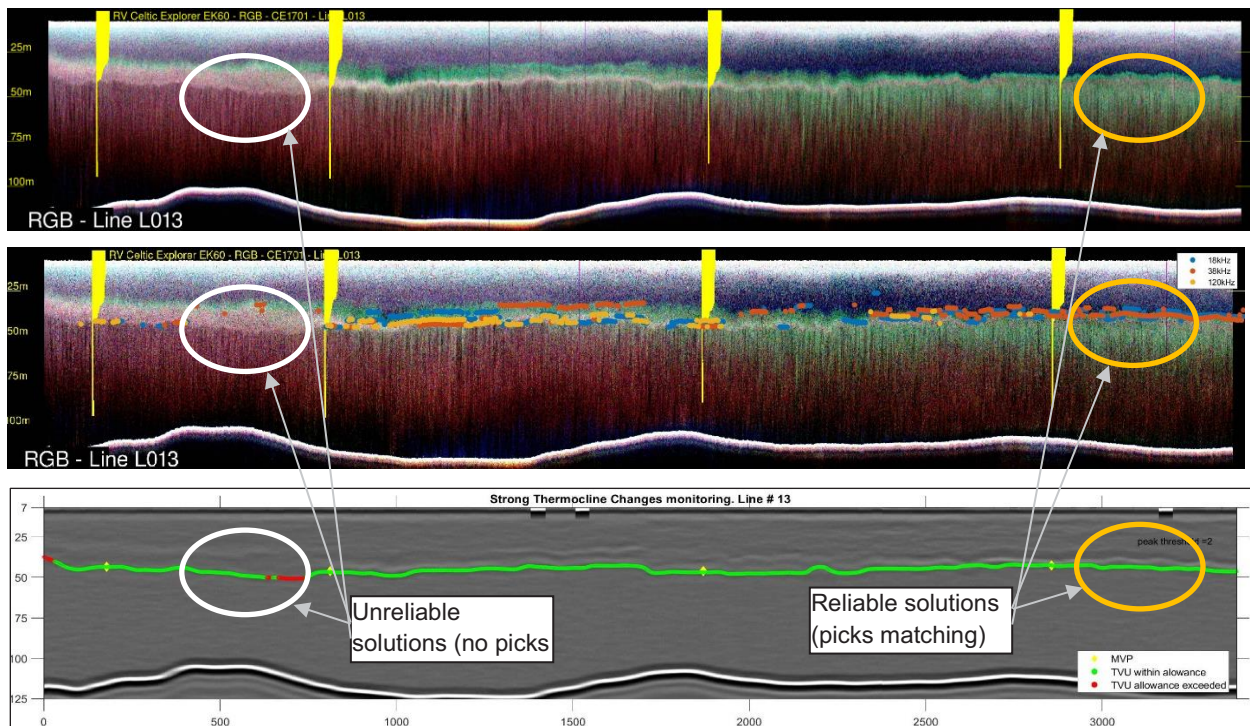
Figure 5.1. Line 013. Daytime example. RGB echogram (top). Individual solution for each frequency (center) and consolidated track of the thermocline (bottom). MVP locations are shown as yellow markers. White circles highlight regions of unreliable solution while yellow circles show reliable solutions.

The daytime tracking was in overall more successful than in any other period of the day. It is due to the fact that the thermocline is better defined on average and the scatterers mimic the bottom of this layer more consistently.

The image filter processing of the echogram is eventually hiding feature of horizontal wavelengths shorter that ~600 m.

It can be noticed in figure 5.1 that the tracking algorithm provides a continuous solution even when there is a gap in detection. This happens whenever the moving window of the Hempel filter is at least the same width of that gap.

5.2 Nighttime.
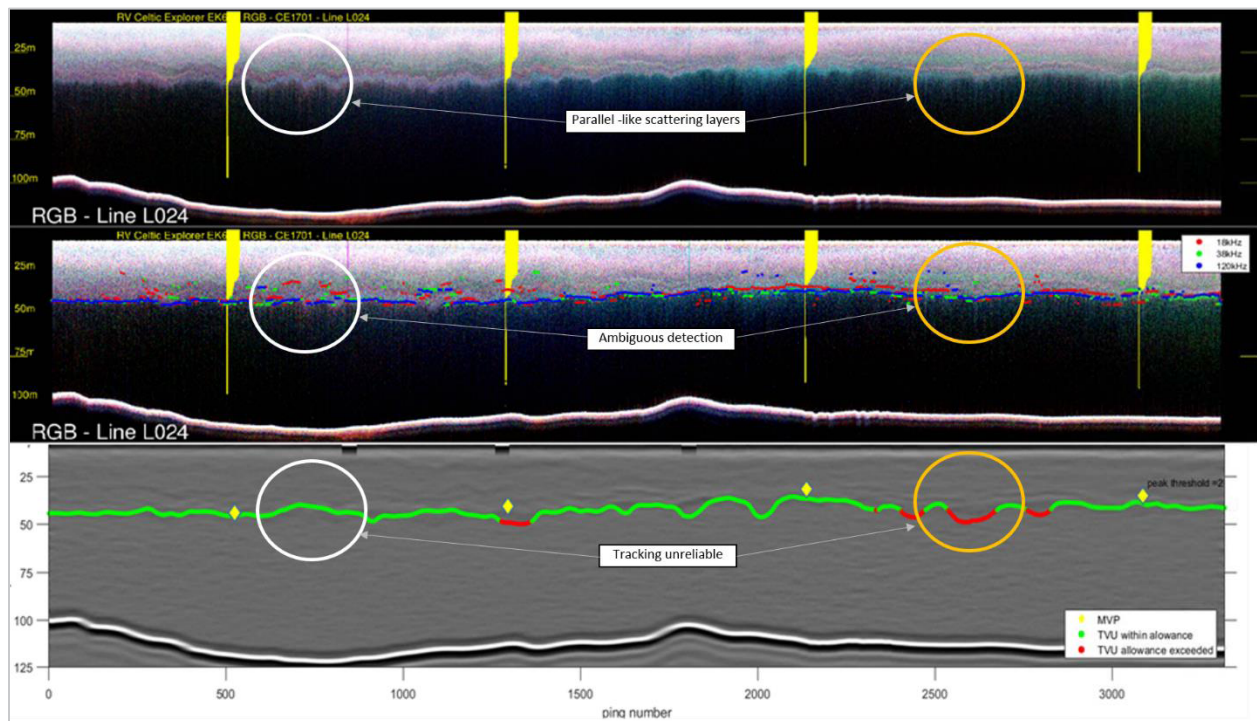
Figure 5.2. Line 024. Nighttime detection example. White and orange circles highlight areas where the algorithm is not effective since shallower scattering layers than the bottom of the thermocline are tracked instead.

During the night, the effectiveness of the algorithm was lower than during daytime. Shallow layers parallel to the bottom of the thermocline are present along the echograms and sometimes they are tracked instead of the thermocline. It can be explained by the diel vertical migration of the biological scatterers and by a stronger echo return. Under these circumstances, the algorithm computed shallower solutions (highlighted as white circles in fig 5.4) than the acoustic image in the RGB overlay.

80
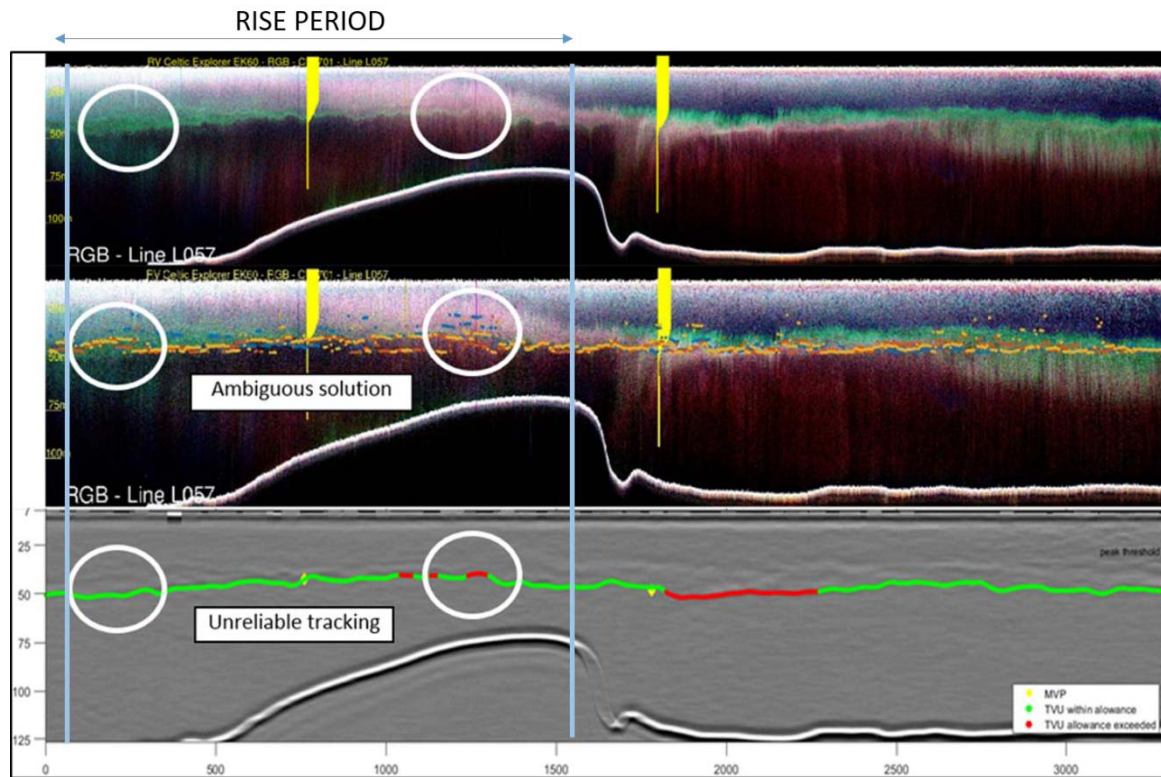
5.3 Twilight.

Figure 5.3. Line 19. Internal wave activity example.

The twilight period presented the least satisfactory results. Scattering from intermediate layers prevented the filter from extracting unambiguous solutions. This effect, already present during the night time, is accentuated 2 hours before dawn and 2 hours after dusk. It can be explained by the initial or ending state of the diel vertical migration.

5.4 Internal waves.
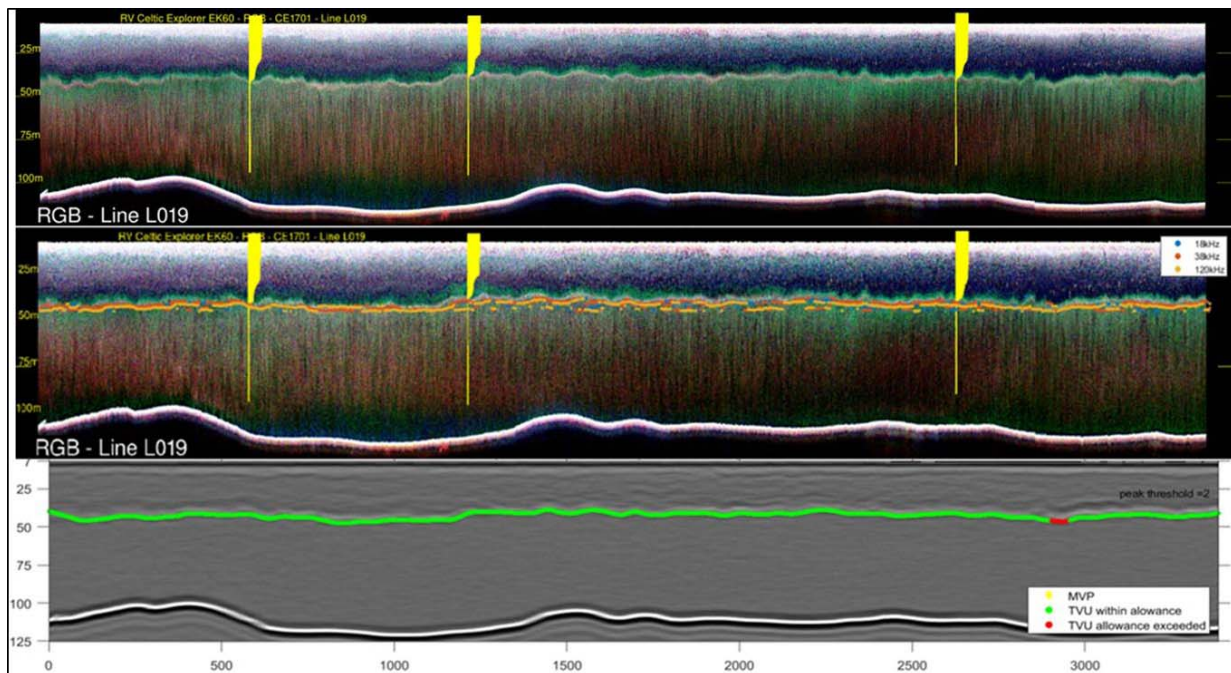
Figure 5.4. Line 057.Internal wave activity example

Adequate tracking of vertical oscillations of the bottom of the thermocline due to internal wave

activity was achieved with some limitations. The low pass filter smoothed horizontal

wavelengths shorter than 620 m (2x31 pixels), meaning that high frequency internal waves and

Kelvin Helmholtz waves were averaged in the final solution.

It has to be highlighted that since that the EK60 system only captures the vertical cross section

of the internal wave and it is projected in a 2D plane, the effect of a tilted velocline is not

included in the vertical uncertainty calculations. Therefore, the real TVU would be higher than

that one presented graphically.

5.5. Spring tide effect.

Enhanced internal wave generation at the slope of Labadie Bank, associated with stronger tidal

flows during spring tide periods, could not be observed since the survey was conducted north of

the bank during that moon phase. No major differences could be observed in the data that were acquired over the bank during the neap tides.

CHAPTER 6

CONCLUSIONS

5.1 Summary

An algorithm was tested to automatically detect and track significant changes in the thermocline from multispectral vertical beam acoustic imagery and to find the correlations with the velocline obtained from underway in situ mechanical profiling measurements. Spatial image filters and decision filters were run to extract high contrast features from EK60 echograms and determine a single solution per each ping for the bottom of the thermocline. These depths were compared to those from the velocline and the induced errors in MBES seafloor modeling for vertical displacements of the sound speed structure were inferred. TVU excesses were computed and visually highlighted as an overlay on the echogram.

5.2. Algorithm success

This method permitted a potential real-time means to trace a solution for the bottom of the thermocline. The results were satisfactory under certain conditions, notably during day time and low turbulence. During nighttime and particularly twilight the algorithm presented higher differences between the measured velocline and the calculated thermocline. It could mean that this comparison between temperature gradient to backscatter is less correlated for those periods of the day. It can be theorized that under those conditions there are scatterers in the water column that are not mimicking the thermocline as they have a biological origin and could follow a diurnal migration pattern.

5.2.1. Minimum Horizontal Wavelength

In addition, the noise removal effect of the low pass filter has a cost. Averaging intensity contrast eventually eliminates short undulation periods and ultimately blanks out the detection of billows. Given the wide beam and lack of across definition of the SIMRAD EK-60 echogram, examination of these shorter wavelength phenomena should best be attempted using water column backscatter from multibeam sonars directly. Most vessels, however, only have a single frequency multibeam system, and the water column data tends to be corrupted with interference and propeller noise. The EK60 systems have the advantage of standard multiple frequencies and a low data volume, which makes the analysis more amenable.

engineering

5.2.2. Top vs Bottom of thermocline tracking.

Regarding the origin of the scatterers, the ephemeral upper scattering layer, which sometimes corresponded to the top of the thermocline, appeared to be diffuse and not consistent along the echogram. As a result, the detection algorithm could not extract robust solutions for the top of the thermocline. This could be explained by an enhanced turbulent response in the upper layer from billows, internal waves or surface waves affecting this region. On the other hand, even though the solutions were more reliable close to the bottom of the velocline, strong scatterers not mimicking the thermocline were sometimes observed. Their presence may be explained by the vertical migration of scattering zooplankton as researched by Stanton et al,(1999).

5.2.3. Spring-Neap Variability.

Although suggested by other studies (Palmer et al., 2013), in this survey, the spring tide periods did not reflect a particular difference in the outcome, as a consequence of an enhanced tidal flow. This could be explained because during this period the survey took place mostly north of Labadie bank and therefore perturbations due to shear over the slopes were not affecting the thermocline

in the same extend as during the neap tide period, mostly conducted over the bank. Only acquiring data simultaneously (off and on bank) could tell if this is true.

5.2.4. MLD correlations.

Finally, accessing the Ocean Mixed Layer predictions from the Copernicus Marine Service, although the correlation with the measure velocline was not conclusive, provided a useful indication of the thermocline range variability in the survey area and could be considered for the sound speed sampling planning. Furthermore, the Mixed Layer depth is just one single sample from the many other parameters available in the Copernicus operational models. These models provide full high-resolution 3D output of temperature and salinity so computing sound speed predictions for the area of interest could be achieved straightforwardly. Also, using a different MLD definition criteria, the top and bottom of the thermocline could be better defined.

Furthermore, the operational models clearly show fine details about the generation and propagation of longer wavelength oscillations (4 km +) all across the Celtic Sea. The shelf break, tidal fronts and oceanic eddies locations are provided by CMES and also standing waves across the continental shelf, some of which appear to be locked to the location of the banks, are accurately displayed.

5.3 Future work.

The image filtering and the detection algorithms present opportunities for improvement by designing filters more capable of accurately extracting the slope distribution of the backscatter features. For a possible new line of research, using deep learning techniques for image classification and pattern recognition like those employed for acoustic seafloor classification (Landmark, 2016) could produce better results. In addition, a further step would be the implementation of a real time solution that could be computed from acoustic imagery produced

from digital scrolling single beam echosounders such as the Kongsberg EA-600 or EA-400 or even navigation echosounder such as Kongsberg EN-250.

Finally, in order to complement the existing Hydroffice package, a comprehensive study is needed to develop tools from the high resolution and free available datasets provided by the Copernicus Marine Service, such as modeling synthetic sound speed profiles or open ocean tides.

LIST OF REFERENCES

Alkan, R. M., Kalkan, Y., & Aykut, N. O. (2006, October). Sound velocity determination with empirical formulas&Bar Check. In *XXIII FIG Congress Munich, Germany* (Vol. 2, p. 12).

Apel, J. R. (2002). Oceanic internal waves and solitons. *An atlas of oceanic internal solitary waves*, 1-40.

Baines, P. G. (1982). On internal tide generation models. *Deep Sea Research Part A. Oceanographic Research Papers*, *29*(3), 307-338.

Beaugrand, G. (2004). The North Sea regime shift: evidence, causes, mechanisms and consequences. *Progress in Oceanography*, *60*(2-4), 245-262.

Carter, D. J. T., & Challenor, P. G. (1989). Estimation of extreme waves. *Metocean Parameters–wave parameters, Dept. of Energy report OTH*, *89*(300), 7-66.

Cooper, L. H. N. (1961). The Oceanography of the Celtic Sea I. Wind Drift. *Journal of the Marine Biological Association of the United Kingdom*, *41*(2), 223-233.

Cushing, D. H. (1952). Echo-surveys of fish. *ICES Journal of Marine Science*, *18*(1), 45-60.

De Jong, J. D., Lachapelle, G., Skone, S., & Elema, I. A. (2002). *Hydrography*. DUP Blue Print.

Dinn, D. F., Loncarevic, B. D., & Costello, G. (1995, October). The effect of sound velocity errors on multi-beam sonar depth accuracy. In OCEANS'95. MTS/IEEE. Challenges of Our Changing Global Environment. Conference Proceedings. (Vol. 2, pp. 1001-1010). IEEE.

Hampel, F. R. (1974). The influence curve and its role in robust estimation. *Journal of the american statistical association*, *69*(346), 383-393.

Haury, L. R., Wiebe, P. H., Orr, M. H., & Briscoe, M. G. (1983). Tidally generated high-frequency internal wave packets and their effects on plankton in Massachusetts Bay. *Journal of Marine Research*, *41*(1), 65-112.

Hill, A. E., Brown, J., & Fernand, L. (1997). The summer gyre in the western Irish Sea: shelf sea paradigms and management implications. *Estuarine, Coastal and Shelf Science*, *44*, 83-95.

Holt, J. T., & Thorpe, S. A. (1997). The propagation of high frequency internal waves in the Celtic Sea. *Deep Sea Research Part I: Oceanographic Research Papers*, *44*(12), 2087-2116.

Holte, J., & Talley, L. (2009). A new algorithm for finding mixed layer depths with applications to Argo data and Subantarctic Mode Water formation. *Journal of Atmospheric and Oceanic Technology*, *26*(9), 1920-1939.

Hughes Clarke, J.E., 2017, Coherent refraction "noise" in multibeam data due to oceanographic turbulence: *Proceedings of the US Hydrographic Conference*, Galveston, TX, 2017 18pp.

Huntley, D. A. (1980). Tides on the north-west European continental shelf. In *Elsevier Oceanography Series* (Vol. 24, pp. 301-351). Elsevier.

Huthnance, J. M., Holt, J. T., & Wakelin, S. L. (2009). Deep ocean exchange with west-European shelf seas. *Ocean Science*, *5*(4), 621-634.

IHO, C. (13). Manual of Hydrography.

Idier, D., Paris, F., Le Cozannet, G., Boulahya, F., & Dumas, F. (2017). Sea-level rise impacts on the tides of the European Shelf. Continental Shelf Research, 137, 56-71.

Inall, M., Aleynik, D., Boyd, T., Palmer, M., & Sharples, J. (2011). Internal tide coherence and decay over a wide shelf sea. *Geophysical Research Letters*, *38*(23).

Kantha, L. H., & Clayson, C. A. (1994). An improved mixed layer model for geophysical applications. Journal of Geophysical Research: Oceans, 99(C12), 25235-25266.

Kimmerer, W. J., Burau, J. R., & Bennett, W. A. (2002). Persistence of tidally-oriented vertical migration by zooplankton in a temperate estuary. Estuaries, 25(3), 359-371.

Lavery, A. and T. Ross, 2007. Acoustic scattering from double-diffusive microstructure. J. Acoust. Soc. Am., 122(3), 1449-1462. doi: 10.1121/1.2764475.

Lavery, A. C. (2014). *Understanding the Effects of Water-Column Variability on Very-High-Frequency Acoustic Propagation in Support of High-Data-Rate Acoustic Communication Applications*. WOODS HOLE OCEANOGRAPHIC INSTITUTION MA DEPT OF APPLIED OCEAN PHYSICS AND ENGINEERING.

Lavery, A. C., Chu, D., & Moum, J. N. (2009). Measurements of acoustic scattering from zooplankton and oceanic microstructure using a broadband echosounder. *ICES Journal of Marine Science*, *67*(2), 379-394.

Lavery, A. C., Wiebe, P. H., Stanton, T. K., Lawson, G. L., Benfield, M. C., & Copley, N. (2007). Determining dominant scatterers of sound in mixed zooplankton populations. *The Journal of the Acoustical Society of America*, *122*(6), 3304-3326.

Lowe, J., Howard, T., Pardaens, A., Tinker, J., Holt, J., Wakelin, S., ... & Reeder, T. (2009). UK Climate Projections science report: Marine and coastal projections.

Lurton, X. (2002). *An introduction to underwater acoustics: principles and applications*. Springer Science & Business Media.

Masetti, G., Kelley, J. G., Johnson, P., & Beaudoin, J. (2018). A Ray-Tracing Uncertainty Estimation Tool for Ocean Mapping. *IEEE Access*, *6*, 2136-2144.

Massel, S. R. (2016). *Internal gravity waves in the shallow seas*. Springer.

Medwin, H. (1975). Speed of sound in water: A simple equation for realistic parameters. *The Journal of the Acoustical Society of America*, *58*(6), 1318-1319.

Munk, W. H., & Garrett, C. J. (1973). Internal wave breaking and microstructure (The chicken and the egg). *Boundary-Layer Meteorology*, *4*(1-4), 37-45.

Nash, J. D., Kelly, S. M., Shroyer, E. L., Moum, J. N., & Duda, T. F. (2012). The unpredictable nature of internal tides on continental shelves. *Journal of Physical Oceanography*, *42*(11), 1981-2000.

O'dea, E. J., Arnold, A. K., Edwards, K. P., Furner, R., Hyder, P., Martin, M. J., ... & Liu, H. (2012). An operational ocean forecast system incorporating NEMO and SST data assimilation for the tidally driven European North-West shelf. *Journal of Operational Oceanography*, *5*(1), 3-17.

Oakey, N. S., & Cochrane, N. A. (1999, July). Turbulent Mixing in Solitons. In *The 1998 WHOI/IOSIONR Internal Solitary Wave Workshop: Contributed Papers* (p. 123).

OSPAR Commission. (2000). *Quality status report 2000* (Vol. 3). The Commission.

Palmer, M. R., Inall, M. E., & Sharples, J. (2013). The physical oceanography of Jones Bank: A mixing hotspot in the Celtic Sea. *Progress in oceanography*, *117*, 9-24.

Petit de la Villéon, C. M. I. S. T. (2017). Copernicus. Product User Manual In Situ TAC products.

Pingree, R. D. (1975). The advance and retreat of the thermocline on the continental shelf. *Journal of the Marine Biological Association of the United Kingdom*, *55*(4), 965-974.

Pingree, R. D. (1980). Physical oceanography of the Celtic sea and English channel. In *Elsevier Oceanography Series*(Vol. 24, pp. 415-465). Elsevier.

Pingree, R. D., & Le Cann, B. (1989). Celtic and Armorican slope and shelf residual currents. *Progress in Oceanography*, *23*(4), 303-338.

Pingree, R. D., Mardell, G. T., Holligan, P. M., Griffiths, D. K., & Smithers, J. (1982). Celtic Sea and Armorican current structure and the vertical distributions of temperature and chlorophyll. Continental Shelf Research, 1(1), 99-116.

Proni, J. R., & Apel, J. R. (1975). On the use of high-frequency acoustics for the study of internal waves and microstructure. *Journal of Geophysical Research*, *80*(9), 1147-1151.

Proni, J.R. and J.R. Apel, 1975. "On the use of high-frequency acoustics for the study of internal waves and microstructure," J. Geophys. Res. 80, 1147-1151.

Robinson, I. S. (1979). The tidal dynamics of the Irish and Celtic Seas. *Geophysical Journal International*, *56*(1), 159-197.

Ross, T., & Lueck, R. (2005). Estimating turbulent dissipation rates from acoustic backscatter. *Deep Sea Research Part I: Oceanographic Research Papers*, *52*(12), 2353-2365.

Ross, Tetjana, Isabelle Gaboury, and Rolf Lueck. "Simultaneous acoustic observations of turbulence and zooplankton in the ocean." *Deep Sea Research Part I: Oceanographic Research Papers,*54.1 (2007): 143-153.

Rothschild, B. J., & Osborn, T. R. (1988). Small-scale turbulence and plankton contact rates. *Journal of Plankton Research*, *10*(3), 465-474.

Rudnick, D. L., & Klinke, J. (2007). The underway conductivity–temperature–depth instrument. *Journal of Atmospheric and Oceanic Technology*, *24*(11), 1910-1923.

Sandstorm, H. J. and A. Elliott. 1984. Internal tide and solitons on the Scotian Shelf: A nutrient pump at work. *J. of Geophysical Research*, *89*, C10.

Sharples, J., Holt, J., & Dye, S. R. (2013). Impacts of climate change on shelf sea stratification. *MCCIP Science Review*, *2013*, 67-70.

Sharples, J., Moore, M. C., Rippeth, T. P., Holligan, P. M., Hydes, D. J., Fisher, N. R., & Simpson, J. H. (2001). Phytoplankton distribution and survival in the thermocline. *Limnology and Oceanography*, *46*(3), 486-496.

Sharples, J., Ellis, J. R., Nolan, G., & Scott, B. E. (2013). Fishing and the oceanography of a stratified shelf sea. Progress in oceanography, 117, 130-139.

Simpson, J. H., & Hunter, J. R. (1974). Fronts in the Irish sea. *Nature*, *250*(5465), 404.

Simpson, J. H., & Sharples, J. (2012). *Introduction to the physical and biological oceanography of shelf seas*. Cambridge University Press.

Smyth, W. D., Burchard, H., & Umlauf, L. (2012). Baroclinic interleaving instability: a second-moment closure approach. *Journal of Physical Oceanography*, *42*(5), 764-784.

Stanton, T. K., Chu, D., & Wiebe, P. H. (1998). Sound scattering by several zooplankton groups. II. Scattering models. *The Journal of the Acoustical Society of America*, *103*(1), 236-253.

Stanton, T. K., Wiebe, P. H., Chu, D., & Goodman, L. (1994). Acoustic characterization and discrimination of marine zooplankton and turbulence. *ICES Journal of Marine Science*, *51*(4), 469-479.

Susanto, R. D., Mitnik, L., & Zheng, Q. (2005, 12). Ocean Internal Waves Observed in the Lombok Strait. *Oceanography, 18*(4), 80-87. doi:10.5670/oceanog.2005.08

Sutherland, B. R. (2010). *Internal gravity waves*. Cambridge University Press.

Thorpe, S. A. (1971). Experiments on the instability of stratified shear flows: miscible fluids. *Journal of Fluid Mechanics*, *46*(2), 299-319.

Thorpe, S. A., & Brubaker, J. M. (1983). Observations of sound reflection by temperature microstructure. *Limnology and Oceanography*, *28*(4), 601-613.

Uncles, R. J., & Stephens, J. A. (1996). Salt intrusion in the Tweed Estuary. *Estuarine, Coastal and Shelf Science*, *43*(3), 271-293.

Uncles, R. J., & Stephens, J. A. (2007). Sea 8 technical report—hydrography. *Strategic Environmental Assessment Programme, UK Dept. of Trade and Industry, London*.

Uncles, R. J., & Stephens, J. A. (2007). Sea 8 technical report—hydrography. *Strategic Environmental Assessment Programme, UK Dept. of Trade and Industry, London*.

Von Schuckmann, K., Le Traon, P. Y., Alvarez-Fanjul, E., Axell, L., Balmaseda, M., Breivik, L. A., ... & Dubois, C. (2016). The Copernicus marine environment monitoring service ocean state report. *Journal of Operational Oceanography*, *9*(sup2), s235-s320.

Wiebe, P. H., Stanton, T. K., Benfield, M. C., Mountain, D. G., & Greene, C. H. (1997). High-frequency acoustic volume backscattering in the Georges Bank coastal region and its interpretation using scattering models. *IEEE Journal of Oceanic Engineering*, *22*(3), 445-464.

APPENDICES

APPENDIX A – MVP_gradient.m script

The following is the Matlab code for deriving the top and bottom of the thermocline from the SVP samples extracted from the MVP casts.

```
%% MVP_gradient. By MS Jose Cordero,2018.
% This script will load and parse the SVP profiles from the MVP samples and will extract the
bottom and the top of
% the thermocline by the gradient method
% the workflow is: importing data > sorting>removing outliers>
% smoothing>plotting> finding gradients> get the bottom and top of the
% thermocline> writting out a file

 %% Step 1. Load the data
clc, clear all

% Selecting files
[FileName,PathName,FilterIndex] = uigetfile('*.*m1','MultiSelect','on'); % m1 is the MVP file
extension

% Reading the files
FileName=cellstr(FileName);
[m,n]=size(FileName);

% Presets
nudge=.0001;
tol=.1;

 %% Step 2.Displaying Data (we will use the downcast sampling better)
n=size(MVP,2);
lgnd=zeros(1,n);
figure(1)
for ii=1:n
    plot(sv{ii},depth2{ii})
    title('Sound Speed Profile - Organized Raw Data')
    axis ij
    xlabel('Sound Speed [m/s]')
    ylabel('depth [m]')
    lgnd(ii)=str2double(FileName{ii}(5:20));
    legend(num2str((lgnd(1:ii))'),'location','west')
    hold on
    end
xlim([1480 1520])
```

```
ylim([0 100])

for ii=1:n
    clear max , clear idx
    MVP{ii} = dlmread([PathName,'\',FileName{ii}],',',75,0); % 75 is the first row with valid data
    ind1=MVP{ii}(:,3)<mean(MVP{ii}(:,3)-50);
    depth_temp=MVP{ii}(:,2);      % We need these temporal variables
    MVP{ii}(:,2)=depth_temp(~ind1); % depth
    sv_temp=MVP{ii}(:,3);
    MVP{ii}(:,3)=sv_temp(~ind1); % sv

        ind2=MVP{ii}(:,3)>mean(MVP{ii}(:,3)+50); % removing everything outside mean +-50
    sv_temp=MVP{ii}(:,3);
    depth_temp=MVP{ii}(:,2);
    MVP{ii}(:,2)=depth_temp(~ind2);
    MVP{ii}(:,3)=sv_temp(~ind2);
     sv_temp=MVP{ii}(:,3);
    depth_temp=MVP{ii}(:,2);

% this is the index for the max
[max1, idx]=max(depth_temp);

% now get only from 1 to max
   sv_temp2=sv_temp(1:idx);
   depth_temp=depth_temp(1:idx);

 % Now we have the descending array without outliers
 % Next thing to do is to average repeated depth values
   [depth_temp,~,idx2] = unique(depth_temp,'stable');
    %depth3={};
    depth3{ii}=depth_temp;
    % smoothing
    %sv2={};
    sv2{ii}= smooth(accumarray(idx2,sv_temp2,[],@mean));
    sx=(smooth(accumarray(idx2,sv_temp2,[],@mean)));
    depth_temp2=depth_temp(depth_temp>16&depth_temp<54);% min and max depths
    sx2=sx(depth_temp>16&depth_temp<54);% min and max depths
    g=diff(sx2)./diff(depth_temp2);
    g2=[0 ;g];
    g3{ii}=g2;
    depth_plot{ii}=depth_temp2;
    %clear depth_temp, clear sv_temp2

end
```

```matlab
    fclose('all')

% SS Gradient vs depth
figure
for ii=1:n
    plot(g3{111}(:),depth_plot{111}(:))
    axis ij
    grid on
    title('Gradient vs depth')
    axis ij
    xlabel('Sound Speed gradient [m/s/d]')
    ylabel('depth [m]')
    hold on
end

%% Step 2. Finding the bottom and the top of the termocline in the SVP

% Now I will find the depths where the gradient is over a certain thresold

for ii=1:n
gg=g3{ii};
[max_grad,ind_grad]=(max(abs(gg))); % Finding the maximum value of the gradient array
gradient_above=find(abs(gg)>(max_grad/7)); % Values of gradient above max/4
ind_top(ii)=min(gradient_above); % this is the index of the top of the thermocline
ind_bot(ii)=max(gradient_above); % this is the index of the top of the thermocline
thermo_bot(ii)=depth_plot{ii}(ind_bot(ii));
thermo_top(ii)=depth_plot{ii}(ind_top(ii));
end

thickness=(thermo_bot-thermo_top)';
mean_thick=mean(thickness);
std(thickness)

% Plotting the downcast
% Sound speed vs depth

for ii=1:n
    FileNameMod{ii}=FileName{ii}(5:end-5);
    h=figure;
    plot(sv2{ii}(:),depth3{ii}(:),'r')
    hold on
    index1 = find(depth3{ii}==thermo_top(ii));
    index2 = find(depth3{ii}==thermo_bot(ii));
    velo_top(ii)=sv2{ii}(index1)
```

```matlab
    velo_bot(ii)=sv2{ii}(index2)

end
for ii=1:n
    fileID{ii} = fopen(FileName{ii},'r');
    linenum = 9;
    LAT(ii) = textscan(fileID{ii},'%22*c%10f',1, 'headerlines',linenum-1);
    LON(ii) = textscan(fileID{ii},'%22*c%10f',1, 'headerlines',1);
    TIME{ii} = textscan(fileID{ii},'%20*c%{HH:mm:ss.s}D',1,'headerlines',2);
    DATE{ii} = textscan(fileID{ii},'%19*c%{dd/MM/yyyy}D',1, 'headerlines',1);
     fclose(fileID{ii});
end
```

APPENDIX B – Parsing_final_results.m script

The following Matlab code displays the extracted thermocline depths from the EK60 echograms , compares them to the ground truth (MVP samples) and displays the locations where a new cast cast should be conducted.

```
%% Parsing final results JMC MAY 2018
% Added Hempel Filter
% This script reads and parses the binary files resulting after the Image
% Processing filtering of the EK60 echograms
% The pixel coordinates are converted into depths. Remind that the
% measurements starts at the transducer depths

% This is has to be run for each line
 clear all;

load('table_line_POS.mat') ; % Importing line numbers , Start and End times (folder
"echograms"
peak_threshold=4;  % Only integers
% Hampel filter parameters
windowSize = 6; %each pixel equals 10 m
numSD =1;

% Use a image viewer to get his values from JHC RGB image
RGB01_start=96;    % try 135
RGB01_end=3500;    % try 3480
RGB01_length=RGB01_end-RGB01_start; % now sure , maybe  add 10

% The maxima delta depth  to initiate the alarm
Thermo_offset=6.5;

% Load the data for the 3 freqs but same filter settings
[fname, pname]= uigetfile('*x51',[], 'multiselect', 'on');
fname=sort(fname); % this way 18 kHz will be the first channel ,
% Reminder: You need to have the line folder open in the file browser

for ii=1:numel(fname)
    s{ii}=dir(fname{ii});
    Nbytesping=3500; %% 3500 is the number of pixels in x dims , obtained from the GIF
images
    Npings=s{ii}.bytes/Nbytesping;
    fid=fopen(fname{ii});
    LF{ii}=fread(fid,[Nbytesping,Npings],'*ubit8');
```

```matlab
        LF{ii}=LF{ii}';
        inx=strfind(fname{1},'0');  % get the spot locations
        line_number=fname{1}(inx(1)+1:inx(1)+2);     % return the substring up to 2nd underscore
        offset=find(LF{ii}(300,:)==0, 1, 'first') ; % this 300 is an assumption. The offset is smaller
        LFS{ii}=LF{ii}(:,1:offset);  % The data is shifted in the x dim.
        LF{ii}(:,1:offset)=[];
        LFH{ii}=double([LF{ii} LFS{ii}]); % Horizontal shifted matrix
        Shift_V{ii}=LFH{ii}(601:625,:); % shifting 20 pixels downward. (10 m)
        LFH{ii}(601:625,:)=[];
        LFF{ii}=double([Shift_V{ii};LFH{ii}]); % Final Matrix with borders aligned
        % imshow(A4)
%       figure
%       imagesc(LFF{ii}); % Now it is OK
%       colormap(gray)
end

% removing the borders
offset2=find(LFF{1}(300,:)~=0, 1, 'first'); % Horizontal offset to find z
offset3=find(LFF{1}(:,300)~=0, 1, 'first'); % vertical offset to find
LFF{1}(:,1:offset2-1)=[]; % Deleting zeros in x(left black frame) for 18khz
LFF{2}(:,1:offset2-1)=[]; % Deleting zeros in x(left black frame) for 38khz
LFF{3}(:,1:offset2-1)=[]; % Deleting zeros in x(left black frame) for 120khz
LFF{1}(1:offset3-1,:)=[]; % Deleting zeros in y(top black frame) for 18khz (from surface to 125m)
LFF{2}(1:offset3-1,:)=[]; % Deleting zeros in y(top black frame) for 38khz
LFF{3}(1:offset3-1,:)=[]; % Deleting zeros in y(top black frame) for 120khz

 % Creating the RGB image
%  RGBImage = uint8(cat(3, LFF{1}, LFF{2}, LFF{3}));
% figure
% imshow(RGBImage)
% title('RGB multispectral combination')

[ydim, xdim]=size(LFF{1}); % dimensions of the non-zero data
interval=2; % This is the samppling interval. Choose 1 to get the results for each ping
x=(1:interval:xdim);
for ii=1:numel(fname)
   for jj=1:length(x)
   sect{jj}=LFF{ii}(:,x(jj));
   end
   sections{ii}=sect;
end

out=cell2mat(cellfun(@(x) cell2mat(x),sections,'un',0)); % composite 3 channel matrix after
interval sampling
```

```matlab
grad_out=abs(out-128);

%% Finding the peaks
[m, n] =size(grad_out);
% Maybe the threshold for thermo top should be change to peak_threshold-1
for ii=1:n
    [pks{ii},locs{ii}]=findpeaks(grad_out(:,ii),'minpeakheight',peak_threshold); % These are the
peaks and the indexes

indexinrange{ii} = locs{ii} > 80 & locs{ii} < 235 ;% Finding indexes depth 18-60 m
pks_subset{ii}=pks{ii}((indexinrange{ii}));
locs_subset{ii}=locs{ii}(indexinrange{ii}) ;
end

% finding the bottom and the top of the thermocline

for ii=1:n
    thermo_bot{ii}=max(locs_subset{ii});
    thermo_top{ii}=min(locs_subset{ii});
    if isempty(thermo_bot{ii})
        thermo_bot{ii}=0;
    end
    if isempty(thermo_top{ii})
        thermo_top{ii}=0;
    end
end

% converting from cell to double
thermo_bot=cell2mat(thermo_bot);
thermo_top=cell2mat(thermo_top);
thermo_bot(thermo_bot==0)=NaN ;
thermo_top(thermo_top==0)=NaN ;
th_bot_18=thermo_bot(1:(n/3));
th_bot_38=thermo_bot((n/3+1):(2*n/3));
th_bot_120=thermo_bot((2*n/3)+1:end);
th_top_18=thermo_top(1:(n/3)); %
th_top_38=thermo_top((n/3+1):(2*n/3));
th_top_120=thermo_top((2*n/3)+1:end);

%% Preparing the data and rejecting outliers

%% Computing averages...
temp1=hampel(th_bot_18,windowSize,numSD);
temp2=hampel(th_bot_38,windowSize,numSD);
```

```
temp3=hampel(th_bot_120,windowSize,numSD);
temp4=hampel(th_top_18,windowSize,numSD);
temp5=hampel(th_top_38,windowSize,numSD);
temp6=hampel(th_top_120,windowSize,numSD);
th_bot_all=[temp1;temp2;temp3];
th_top_all=[temp4;temp5;temp6];
clear temp1 temp2 temp3 temp 4 temp5 temp6

% 117/ydim is the scale factor to convert number of pixels to meters

%% Saturday 19 May mod. HAMPEL FILTER
th_deepest=max(th_bot_all); % deeper values are preferred for the bottom
% Hampel function. Specify the number of neighbors on either side of each sample of the data
in the measurement window.
% Specify the number of standard deviations to be 10. If a data point differs from the local
median by more than this number it is replaced with the median value.
% windowSize = 20; %each pixel equals 10 m
% numSD =1;
th_smooth = hampel(th_deepest,windowSize,numSD);

%%%%BEFORE MOD%%
% th_smooth=smooth(th_median,0.03,'rloess','omitnan');  % This is the other
% approach instead of the hampel filter
% Converting pixel y dim to depth in meters
th_smooth_meters_bot=(th_smooth*117/ydim+8); % 8 is the transducer depth

% the same for the top
th_shallowest=min(th_top_all) ;%(top is Z=0)
% th_median_top=median(th_top_all,'omitnan'); % median values from all channels input
% th_smooth_top=smooth(th_median_top,0.04,'rloess');
th_smooth_top=hampel(th_shallowest,windowSize*1.5,numSD); % The filter window is wider for
the top
th_smooth_meters_top=(th_smooth_top*117/ydim+8) ;

%% Adding the time stamps
load('LineDateTime.mat') ; % file located in ...MATLAB\Drive\Published\Thesis\Echograms
load('MVP_data_grad.mat') ; % MVP datetime and MVP thermo bottom depth of the MVP
shown in the images (MVPdata.MVP_time,MVPdata.MVP_depth);Previous line location

% Contains line number, Start and end date time
TimeEnd=datenum(TimeEnd) ; % converting into datenum
TimeStart=datenum(TimeStart);
MVP_time=datenum(MVP_time);
% How many time slices? --- length(x) (depends on the sampling interval).
```

```
% This will get the indexes for each IP depth in this line
thermo_time=linspace(TimeStart(str2double(line_number)),TimeEnd(str2double(line_number)),l
ength(x))'; % Times of the present line

% Findind the MVP for this line
for jj=1:length(MVP_time)
indx{jj}=find(thermo_time<MVP_time(jj));
end

for jj=1:length(indx)
    temp(jj)=length(indx{jj});
end

% another approach, same result
temp(temp == 0 ) = NaN;
[~,MPV_ind_min] = min(temp); % this is the first MVP for this line from the MVP list
temp(temp == length(x)) = NaN;
[~,MPV_ind_max] = max(temp); % this is the last MVP for this line from the MVP list

MPV_times_this_line=MVP_time(MPV_ind_min:MPV_ind_max);

for ii=1:length(MPV_times_this_line)
[va(ii), wi(ii)]=findClosest(thermo_time,MPV_times_this_line(ii));
end

% First approach
indx=indx(~cellfun('isempty',indx));% Removing empty cells

for ii=1:length(indx)
indxx(ii)=max(indx{ii});
end
indxx2=indxx(indxx~=length(x)); % these are the indexes of the MVP. They are good

%%NOTE 14 MAY 2018. The MVPs shown in the JHC label image DO NOT MATCH

%% Adding position and range to the slope of each point
% Number of elements of this array= num samples =n
% interpolate positions
load('labadie.mat')
[labadie_x_UTM, labadie_y_UTM]=ll2utm(Labadie(:,2),Labadie(:,1));
line_num=str2double(line_number);
[UTM_x_start,UTM_y_start,UTM_zone]=deg2utm(table_line_POS.lat_start(line_num), -
table_line_POS.lon_start(line_num));  % remember negative long
```

```
[UTM_x_end,UTM_y_end]=deg2utm(table_line_POS.lat_end(line_num), -
table_line_POS.lon_end(line_num));
% calculating the evenly spaced locations (assigning  POS to each sampling
% point)
UTM_x=linspace(UTM_x_start,UTM_x_end,length(x));
UTM_y=linspace(UTM_y_start,UTM_y_end,length(x));

% Now the distances to Labadie
for ii=1:length(x)
[pings_to_Labadie(ii),pings_to_Labadie_x(ii), pings_to_Labadie_y(ii)] = p_poly_dist(UTM_x(ii),
UTM_y(ii), labadie_x_UTM, labadie_y_UTM) ;
end

%% Plotting results
% Finding if the current line is 'westward' (E to W), (echogram should be
% flipped
% We can know it since we alreaday got the UTM coordinates.
westward=UTM_x(1)>UTM_x(end);
eastward=UTM_x(1)<UTM_x(end);
%% Scaling: this is necessary to overplot the results on the pre-existing images of different size
(x 3500, y 625)
%%Important reminder
% the pre=existing images shows depths ranging from 0 to 125 m
% The data starts at the transducer (~8 m) and goes to 125m. in total 117 m
% It needs to be adjusted in the vertical scaling

scaling_horiz=RGB01_length/xdim; % it already excludes zero value in the ImPro
horiz=scaling_horiz*(x)-(RGB01_start);
horiz=(RGB01_start)+(x/scaling_horiz);
scaling_vert=625/(ydim-ydim/117*7);

% preparing the title
ix=strfind(fname{1},'.');  % get the dot locations
name=fname{1}(ix(2)+1:end);     % return the substring up to 2nd underscore

% preparing the jpg name
ix2=strfind(fname{1},'L');  % get the dotlocations
name_jpg=fname{1}(ix2(1):ix2(1)+3);     % return the substring up to 2nd underscore
sufix1={'_3channels bot'};
sufix2={'_3 channels top'};
sufix3={'_18 kHz_bottom'};
sufix4={'_18 kHz_top'};
sufix5={'_38 kHz_bottom'};
sufix6={'_38 kHz_top'};
```

```matlab
sufix7={'_120 kHz_bottom'};
sufix8={'_120 kHz_top'};
sufix9={'_newcast'};
sufix10={'_RGB'};

name_fig1=[name_jpg sufix1];
name_fig2=[name_jpg sufix2];
name_fig3=[name_jpg sufix3];
name_fig4=[name_jpg sufix4];
name_fig5=[name_jpg sufix5];
name_fig6=[name_jpg sufix6];
name_fig7=[name_jpg sufix7];
name_fig8=[name_jpg sufix8];
name_fig9=[name_jpg sufix9];
name_fig10=[name_jpg sufix10];
filenamex = [name_fig1 '.jpg'];
filenamex = strjoin(filenamex);
filenamex2 = [name_fig2 '.jpg'];
filenamex2 = strjoin(filenamex2);
filenamex3 = [name_fig3 '.jpg'];
filenamex3 = strjoin(filenamex3);
filenamex4 = [name_fig4 '.jpg'];
filenamex4 = strjoin(filenamex4);
filenamex5 = [name_fig5 '.jpg'];
filenamex5 = strjoin(filenamex5);
filenamex6 = [name_fig6 '.jpg'];
filenamex6 = strjoin(filenamex6);
filenamex7 = [name_fig7 '.jpg'];
filenamex7 = strjoin(filenamex7);
filenamex8 = [name_fig8 '.jpg'];
filenamex8 = strjoin(filenamex8);
filenamex9 = [name_fig9 '.jpg'];
filenamex9 = strjoin(filenamex9);
filenamex10 = [name_fig10 '.jpg'];
filenamex10 = strjoin(filenamex10);
warning('off', 'Images:initSize:adjustingMag');


%% Step 14. Calculating the difference WRT MPV. (Truth-measurement)
% Another way to find the MVPs for this line
for ii=1:length(x)
[~, ind_MVP_temp(ii)]=findClosest(MVP_time,thermo_time(ii));
end
```

```matlab
% Remind that MPV(1) could correspond to the previous line
ind_MVP=unique(ind_MVP_temp);
if numel(ind_MVP)>numel(indxx2)
ind_MVP(1)=[];
end

% MPV_times_this_line= MVP_time(ind_MVP)% Other way to do it
for ii=1:length(MPV_times_this_line)
[~, ind_MVP_xdim(ii)]=findClosest(thermo_time,MPV_times_this_line(ii));
end

% MVP bottom deptht at each location-Hampel filtered depths for the thermo-bot
MVP_IP_bot_diff=MVP_bot(ind_MVP)-th_smooth_meters_bot(indxx2)';

% smoothed solutions
% th_smooth_meters_bot(indxx2);
% thermo_bot_mean(indxx2)*117/568+8;

if mean(abs(MVP_IP_bot_diff))>1.5;   % max error tolerance
    warning_message = sprintf('Initial detection threshold value NOT valid.Detected depths are
too far from MVP values');
    msgbox(warning_message);
    MVP_IP_bot_diff
% return
end

%% Step 15. Plotting

pic_nam='Reg_Sect_L0XX.MVP.RGB.label.gif';
pic_name = strrep(pic_nam,'L0XX',name_jpg);

% Thermo bottom on the RGB LABELED
figure
% imshow(pic_name)
hold on
scatter(horiz,scaling_vert*th_bot_18,10,'r','filled')
scatter(horiz,scaling_vert*th_bot_38,10,'g','filled')
scatter(horiz,scaling_vert*th_bot_120,10,'b','filled')
% plot(horiz,scaling_vert*th_smooth,'cyan','LineWidth',1.5)
legend('18kHz','38kHz' ,'120kHz','thermo bot','Location','southeast')
title(name,'Interpreter', 'none')
xlabel('Bottom of the thermocline multispectral detection')
% saveas(gcf,filenamex)  % here you save the figure
```

```
% Thermo top on the RGB LABELED
% figure
% imshow(pic_name)
% hold on
% scatter(horiz,scaling_vert*th_top_18,12,'r','filled')
% scatter(horiz,scaling_vert*th_top_38,12,'g','filled')
% scatter(horiz,scaling_vert*th_top_120,12,'b','filled')
% plot(horiz,scaling_vert*th_smooth_top,'cyan','LineWidth',2)
% legend('18kHz','38kHz' ,'120kHz','thermo top','Location','southeast')
% title(name,'Interpreter', 'none')
% txt=['peak threshold =', num2str(peak_threshold)];
% text(3100,100,txt)
% xlabel('Top of the thermocline multispectral detection')
% saveas(gcf,filenamex2)  % here you save the figure


% %% Ploting on the IP images   red - 18 kHz, green 38 kHz, blue 120 kHz.
% %18 kHz bottom
% figure
% imshow('Rot_L002.018kHz.low_41x05.vert_grad_01x15.high_01x51.jpg')
% hold on
% offset_xtra=0;
% scatter(x+offset2/2+offset_xtra,scaling_vert*th_bot_18,10,'r','filled') %Added xtra offset
% title(['Line number  ',num2str(line_number),', channel 18 kHz'])
% txt=['peak threshold =', num2str(peak_threshold)];
% text(3000,100,txt)
% legend('Image Processing thermocline bottom detections for 18 kHz','Location','south')
% xlabel('datetime')
% ylabel('depth')
% % saveas(gcf,filenamex3)  % here you save the figure
%
% %18 kHz top
% figure
% imshow('Rot_L002.018kHz.low_41x05.vert_grad_01x15.high_01x51.jpg')
% hold on
% scatter(x+offset2/2+offset_xtra,scaling_vert*th_top_18,10,'r','filled')
% title(['Line number  ',num2str(line_number),', channel 18 kHz'])
% txt=['peak threshold =', num2str(peak_threshold)];
% text(3000,100,txt)
% legend('Image Processing thermocline top detections for 18 kHz','Location','south')
% xlabel('datetime')
% ylabel('depth')
% % saveas(gcf,filenamex4)
%
```

```matlab
% %38 kHz bottom
% figure
% imshow('Rot_L002.038kHz.low_41x05.vert_grad_01x15.high_01x51.jpg')
% hold on
% scatter(x+offset2/2+offset_xtra,scaling_vert*th_bot_38,10,'r','filled')
% title(['Line number  ',num2str(line_number),', channel 38 kHz'])
% txt=['peak threshold =', num2str(peak_threshold)];
% text(3000,100,txt)
% legend('Image Processing thermocline bottom detections for 38 kHz','Location','south')
% xlabel('datetime')
% ylabel('depth')
% % saveas(gcf,filenamex5)
%
% %38 kHz top
% figure
% imshow('Rot_L002.038kHz.low_41x05.vert_grad_01x15.high_01x51.jpg')
% hold on
% scatter(x+offset2/2+offset_xtra,scaling_vert*th_top_38,10,'r','filled')
% title(['Line number  ',num2str(line_number),', channel 38 kHz'])
% txt=['peak threshold =', num2str(peak_threshold)];
% text(3000,100,txt)
% legend('Image Processing thermocline top detections for 38 kHz','Location','south')
% xlabel('datetime')
% ylabel('depth')
% % saveas(gcf,filenamex6)
%
% %120 kHz bottom
% figure
% imshow('Rot_L002.120kHz.low_41x05.vert_grad_01x15.high_01x51.jpg')
% hold on
% scatter(x+offset2/2+offset_xtra,scaling_vert*th_bot_120,10,'y','filled')
% title(['Line number  ',num2str(line_number),', channel 120 kHz'])
% txt=['peak threshold =', num2str(peak_threshold)];
% text(3000,100,txt)
% legend('Image Processing thermocline bottom detections for 120 kHz','Location','south')
% xlabel('datetime')
% ylabel('depth')
% % saveas(gcf,filenamex7)


%% Step LAST. PLOTTING FINAL RGB
% indxx2=indxx(indxx~=length(x)); % these are the indexes of the MVP
% indxx2=sort(length(x)-indxx2) ; % Finally, this are the indexes of the MVP
```

```
% MPV_bot_final=flip(MVP_bot(MPV_ind_min:MPV_ind_max));  % Depth MVP
MPV_bot_final=MVP_bot(MPV_ind_min:MPV_ind_max);  % Depth MVP

% Checking MVP bottom vs IP solution
th_smooth_meters_bot(indxx2); %IP Depth at MVP
% th_smooth_meters_bot(indxx2)=MPV_bot_final;


%% Last plot using our RGB.
% is this line inverted? If so then FLIP the RGB_plot
% The vertical scaling factor to convert from pixel to meter is 117/ydim
% top pixel is at transducer depth (8m) and the bottom pixel is at 125 m .
% vertical range is therefore 125-7=117m. In pixel dimemsions, it the the
% height if the image ydim , 569 pixels
% meters=4.8*pixel-offset
% ( remember we are plotting pixels)

RGBImage = uint8(cat(3, LFF{1}, LFF{2}, LFF{3})); % This is our RGB image (smaller that
JHC's)
temp=rgb2gray(RGBImage);
RGB_plot = imadjust(temp);
RGB_plot_flip=flip(RGB_plot,2);
% Now remind thee offset between the RGB IP (starts at 8 m depth ) and the MVP
% depths (start at 0) 8m=39 pixels
 offset_IP=39;% This offset is used for plotting ,not for calculating diff
RGB_westward=RGB_plot_flip(westward);


figure;
hold on
imshow(RGB_plot)
% imshow(RGB_westward)
title('Strong Thermocline Changes monitoring')
hold on
hscat=scatter(indxx2*interval,[ydim/117*MVP_bot(MPV_ind_min:MPV_ind_max)-
offset_IP],80,'y','filled','d'); % MVP_x_loc vs MVP_bot
ylabel('depth in meters')
xlabel('ping number')
set(gca, 'visible', 'on')
ax = gca; % current axes
ax.FontSize = 12;
ax.TickDir = 'out';
ax.TickLength = [0.02 0.02];
ax.YLim = [0 size(RGB_plot,1)];
```

```matlab
ax.XLim = [0 size(RGB_plot,2)];
yticks([0 87 207 328 448 567])
yticklabels({'7','25','50','75','100','125'})
h = zeros(3, 1);
h(1) = plot(NaN,NaN,'dy','MarkerFaceColor','y');
h(2) = plot(NaN,NaN,'og','MarkerFaceColor','g');
h(3) = plot(NaN,NaN,'or','MarkerFaceColor','r');
legend(h, 'MPV','Love boat ','Cast again','Location','southeast')
for jj=1:length(x) % number of samples per channel throughout the line
    [~,MPV_closest(jj)]=findClosest(MVP_time,thermo_time(jj));
    depth_diff(jj)=abs((th_smooth_meters_bot(jj)-MVP_bot(MPV_closest(jj))));
%     if isnan(wa(jj)), plotme(jj)=100;
%     end
    scatter(x(jj),th_smooth(jj),16,'green')
     pause(0.004)
       if depth_diff(jj)>Thermo_offset
       colorMap='red';
       scatter(x(jj),th_smooth(jj),16,colorMap)
       pause(0.004)
    end
end
% saveas(gcf,filenamex10)  % here you save the figure

%%Step 19  .Creating the table
% It will include:time,POS,,Labadie_range,thermo_top,thermo_bo
table_num=line_num*ones(length(x),1);
% table_num=table_num';
UTM_x=UTM_x';
UTM_y=UTM_y';
% thermo_time=thermo_time'
pings_to_Labadie=pings_to_Labadie';
table_name=strcat('table_L',line_number);
th_smooth_meters_top=th_smooth_meters_top';
th_smooth_meters_bot=th_smooth_meters_bot';
table_this_line=table(table_num,thermo_time,UTM_x,UTM_y,pings_to_Labadie,th_smooth_met
ers_bot,th_smooth_meters_top);
save(table_name,'table_this_line');
% another table for the diff
table_name2=strcat('table_MVPdiff_L',line_number);
MVP_IP_bot_diff
table_MVPdiff=table(MVP_IP_bot_diff);
save(table_name2,'MVP_IP_bot_diff');
%
```